Unterschrift des Betreuers

TECHNISCHE UNIVERSITÄT WIEN
Vienna University of Technology

DIPLOMARBEIT

Magnetic properties of deformed Electrical Steel

Ausgeführt am Institut für

Festkörperphysik

der Technischen Universität Wien

unter der Anleitung von

Ao.Univ.Prof.Dipl.-Ing. Roland Grössinger

durch

Stefan Hartl

Gartengasse 25, 2352 Gumpoldskirchen

_____   _____
Datum   Unterschrift

Aknowledgments...

Abstract

Soft magnetic materials are very important for magnetic and electric applications. The quality of a material is not only defined by the elements used in the alloy, but also by the internal or external influences like applied stress, which was investigated in this thesis. The material used was M400-50A electrical steel, which corresponds to Fe3%Si. In this thesis the influence on the hysteresis loops and the magnetostriction on homogeneous deformed ring shaped samples were investigated. For a homogeneous deformation, tensile and rolling procedures were chosen. On the samples, magnetic hysteresis and the magnetostriction was measured. From this measurements the overall core losses, the permeability, the coercive field strength and the magnetostriction were calculated. The observed changes, regarding the deformation, were used to establish a model to predict the losses and magnetostriction at certain deformation.

 The second part of this thesis investigates inhomogeneous deformation, based on punched ring shaped samples, which were produced by the „Austrian Institute of Technology". Different punching parameters (punching speed, clearance) were applied to simulate a real manufacturing process for cutting electrical steel. Again the changing losses and coercive field strength was analysed. Due to the complexity of the deformation, it can only be predicted using numerical simulations. A similar approach using the Jiles-Atherton model was done in a previous theoretical work. With the measurement data in this thesis, the model can be verified and improved.

Zusammenfassung

Weichmagnetische Materialien sind ein wichtiger Bestandteil für elektrische Anlagen. Die Qualität eines Materials ist nicht nur von den Elementen in der Legierung abhängig, sondern auch von internen und externen Einflüssen, wie die induzierte Spannung, welche in dieser Arbeit untersucht wurde. Das verwendete Material war M400-50A Elektroblech, was Fe3%Si entspricht. In dieser Arbeit der Einfluss der Hystereseschleifen und der Magnetostriktion auf homogene verformte Ringproben wurde untersucht. Für die homogene Verformung wurde Ziehen und Rollen gewählt. An den Proben wurden Hysterese und Magnetostriktion gemessen. Ausgehend von diesen Messungen die gesamten Hystereseverluste, die Permeabilität, das Koerzitivfeld und die Magnetostriktion konnten berechnet werden. Die beobachteten Änderungen, bezüglich der Verformung, wurden verwendet ein Model aufzustellen um die Verluste bei bestimmten Deformationen vorherzusagen.

 Der zweite Teil der Arbeit untersucht inhomogene Deformation, an gestanzten Ringproben. Diese wurden vom „Austrian Institute of Technology" hergestellt. Verschiedene Stanzparameter (Stanzgeschwindigkeit, Schnittspalt) wurden verwendet um einen realen Fertigungsprozess an Elektroblech zu simulieren. Auch hier wurden die Änderung der Verluste und des Koerzitivfeldes analysiert. Aufgrund des komplexen Verformungszustandes, eine Vorhersage ist nur durch numerische Simulation möglich. Ein solcher Ansatz basiert auf dem Jiles-Atherton Modell, welches in einer vorangegangenen theoretischen Arbeit behandelt wurde. Mit den Ergebnissen der Messungen in dieser Arbeit kann dieses erweiterte Modell überprüft und verbessert werden.

Nomenclature

General

σ	conductivity	$[S/m]$
σ_i	standard deviation from a variable i	$[\%]$
$\vec{E}$	electric field	$[V/m]$
$I(t)$	current	$[A]$
m_{Fe_i}	mass of one ring	$[g]$
m_{ges}	mass of one sample	$[g]$
R_{shunt}	shunt resistor	$[\Omega]$
$U(t)$	voltage	$[V]$

Magnetic

α_i	direction of the magnetization	$[T]$
β_i	magnetostriction direction	
χ_m	magnetic susceptibility	
η_{Fe}	iron fill factor	
γ	anisotropy saturation constant	
λ	(generally) magnetostriction	
$\lambda_{\parallel}$	magnetostriction along magnetic field $\vec{H}$	
$\lambda_{\perp_0}$	magnetostriction perpendicular undeformed	
$\lambda_{\perp}$	magnetostriction perpendicular to magnetic field $\vec{H}$	
λ_{ijk}	magnetostriction in specified direction [ijk]	
μ_0	vacuum permeability	$[V \cdot s/A \cdot m]$
μ_r	relative permeability	
ω	volume magnetostriction	
$\overline{M}_{ijkl}$	magnetoelastic stress tensor	
Φ	magnetic flux	$[Wb]$
Φ_w	magnetic flux per winding	$[Wb]$

Ψ	magnetic flux for coils	$[Wb]$
θ	angle between magnetization $\vec{M}$ and applied field $\vec{H}$	$[rad]$
θ, ϕ, ψ	angle of the $\vec{\alpha}$ and $\vec{\beta}$	
$\varepsilon_{ij}, \varepsilon_{ms}$	magnetostriction strain	
$\vec{B}$	magnetic flux density	$[T]$
$\vec{H}$	magnetic field strength	$[A/m]$
$\vec{M}$	magnetization	$[A/m]$
A	magnetic surface	$[m^2]$
A_{Fe}	iron surface	$[m^2]$
c_{ijkl}	elastic tensor	
E_K	magnetocrystalline anisotropy energy	$[J]$
E_{el}	elastic energy	$[J]$
E_{mel}	magnetoelastic energy	$[J]$
E_m	magnetic free energy	$[J]$
H_{heis}	Heisenberg Hamiltonian	$[J]$
h_i	Becker and Döring expansion constants	
J_s	saturation polarization	$[T]$
K_1	magnetocrystalline anisotropy constant (first order)	$[J/m^3]$
K_2	magnetocrystalline anisotropy constant (second order)	$[J/m^3]$
K_{eff}	effective magnetocrystalline anisotropy constant	$[J/m^3]$
K_{ij}	anisotropy tensor	
l_m	magnetic mean length	$[m]$
M_s	saturation magnetization	$[A/m]$
N_1	primary winding	
N_2	secondary winding	

Mechanical

α	heat coefficient	$[1/K]$
Δx	length change	$[m]$

σ_{res}	residual stress	$[MPa]$
ε_x	strain	$[\%]$
φ_x	rolling deformation	$[\%]$
E_{pd}	Young's module perpendicular to rolling direction	$[GPa]$
E_{rd}	Young's module in rolling direction	$[GPa]$
R_m	ultimate tensile strength	$[N/mm^2]$
R_p	yield strength	$[N/mm^2]$
x_0	original length	$[m]$

Acronyms

AIT	Austrian Institute of Technology
BCC	body centered cubic
EDT	Electric Drive Technology
FEM	Finite Element Method
MCA	magnetocrystalline anisotropy
MEL	magnetoelastic
MELA	magnetoelastic anisotropy
MS	magnetostriction
VUT	Vienna University of Technology

List of Figures

List of Tables

Table of Contents

1 Introduction

The electrical industry is always searching for better magnetic materials and improved manufacturing methods. In today's production an alloy of FeSi has proven itself as an compromise between low production cost and small magnetic losses, so that the energy loss is reduced during induction. The aim of this work is to investigate the influence of deformation on the hysteresis, and therefore on the losses, on Electro Steel and their appliances.

Within the masterthesis of Simon Ertl the deformation effect of magnetic materials using a theoretical approach was studied. There exists still no unified theory to describe stress effects on the hysteresis. The usual models describe an isotropic hysteresis loop including the crystal structures of a ferromagnetic material, but considering anisotropy or magnetostriction causes discrepancies. Simon Ertl used the Jiles-Atherton model which sums the hysteresis loops of small cells to the total hysteresis of the sample. This is a numerical process, which uses an algorithm to derive an approximate solution. The cells can be connected by several physical properties (hysteresis loops, residual stresses), but then the solution may be hard to calculate. The simulation algorithm from Simon Ertl uses the standard Jiles-Atherton model however including cell deformation as a physical parameter. Therefore it is possible to calculate the hysteresis of a deformed material with respect to a reference (undeformed) material. The results were very promising and provide realistic hysteresis shapes [9]. In this thesis the adapted model of Jiles-Atherton should be verified and if possible improved.

In order to verify the theoretically simulated loops, experimental data are needed. With the knowledge and the material from the Electric Drive Technology (EDT) department of the Austrian Institute of Technology (AIT) ring samples for hysteresis measurements can be produced from M400-50A. This is a standard electro steel (Fe3%Si) for applications. The material will be deformed under controlled conditions. Applying a controlled deformation a correlation to the crystal structure can be made and can be compared with a reference (undeformed) sample. Also samples will be produced with a punching machine. Punching is the most common cutting process in the industry, because it is fast, accurate and cheap. These samples are produced with certain punching parameters and will give information on the cutting tool during the manufacturing process. With an additional FEM simulation of the punching process it is possible to verify the adapted model

for more complex problems and also improve it.

On the identical ring shaped and mechanically deformed samples also the magnetostriction is measured. Because the windings are homogeneous distributed over the whole ring, the transversal and longitudinal magnetostriction can be measured. From these data the saturation magnetostriction is calculated. The magnetostriction is directly connected to the crystal structure and the magneto elastic energy.

There exist several publications discussing the influence of a mechanical deformation processes on the hysteresis loop. The work of Takahashi specifically measured the losses of the components of electric motors under stress [36]. In another paper magnetic properties of certain materials were measured under strain using the Barkhausen noise [32]. Most publications on this matter state a change in the shape of the hysteresis due to deformation but there is no general idea to forecast the stress induced change of hysteresis or losses. In summary reference samples, homogeneous deformed samples and samples with irregular deformation will be used for this study. Ring samples will be cut out of the deformed material with a laser cutting method. This method almost does not affect the stress state of the whole sample. Then the hysteresis loop will be measured and the core losses will be analysed. In addition, the magnetostriction is taken to determine the magneto elastic energy. With the experimental data an adapted theoretical model of Jiles-Atherton should be verified and improved and also the influence of deformation on the core losses is to be examined. This can give first informations concerning the deformation of the material during the manufacturing process and by changing certain process parameters the overall losses may be reduced.

2 Theoretical Treatment

The effect of magnetism is characterised in para-, dia-, ferro and ferrimagnetism. In this work only ferromagnetic materials were used and therefore only this part of the magnetism is covered in the sections below. Because the magnetism is a very large part of physics and is mainly not yet fully explored, just the necessary theories needed to explain the scientific work are being used.

Para- and diamagnetic materials have a simple connection between the magnetic field strength and the magnetic flux density

$$\vec{B} = \mu \cdot \vec{H} = \mu_0(\vec{M} + \vec{H}) = \mu_0\mu_r \cdot \vec{H}. \tag{2.1}$$

where μ_r is the relative permeability which is connected with the magnetic susceptibility χ_m via

$$\mu_r = 1 + \chi_m \tag{2.2}$$

which describes the magnetizability of a material. This equations come directly from Maxwell's equations and can easily be derived. The magnetization $\vec{M}$ is the dipole moment per unit volume and the response of the material due to an external field. A more complex way to write the susceptibility is

$$\chi = \frac{\partial \vec{M}}{\partial \vec{H}}. \tag{2.3}$$

This interpretation especially is needed when the response of a external field is not linear anymore. This is the case for ferromagnetic materials and a interpretation for deformed materials will be made in this thesis.

Some textbooks draw the hysteresis loop with the field $\vec{H}$ over the magnetic flux density $\vec{B}$. This is not quite the truth. The real response field is

$$\vec{J} = \vec{B} - \mu_0\vec{H} \tag{2.4}$$

where $\vec{J}$ is the magnetic polarization. It is the (averaged) contribution from the material to the magnetic flux density [1].

2.1 Induction

Electromagnetic induction is a basic law in electrodynamics. To calculate the field in a wire or coil

$$H(t) = \frac{N_1}{l_m} \cdot I(t) = \frac{N_1}{l_m} \frac{U(t)}{R_{shunt}} \tag{2.5}$$

Furthermore the magnetic mean path l_m has to be calculated, which is in first order for a toroidal sample

$$l_m = \frac{(d_a + d_i)}{2} \cdot \pi \tag{2.6}$$
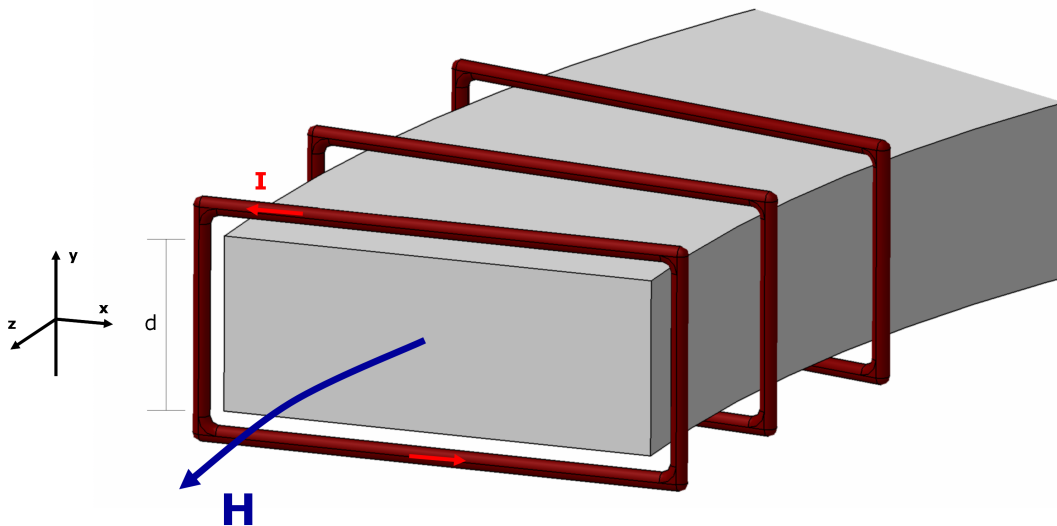
Figure 2.1: Induction of the magnetic field strength H into the ring shaped sample via the winding

It was discovered by Faraday and can be transformed in one Maxwell equation. It describes that, the change of the magnetic flux density results in an electric vortex field

$$\vec{\nabla} \times \vec{E} = -\frac{\partial \vec{B}}{\partial t} \tag{2.7}$$

which is transformed to an integral equation using Stokes law to [19, p.6]

$$\oint_{\partial A} \vec{E} \cdot d\vec{s} = - \int_A \frac{\partial \vec{B}(t)}{\partial t} \cdot d\vec{A} \tag{2.8a}$$

$$U(t) = \frac{d}{dt} \int_A \vec{B} \cdot d\vec{A} = \frac{d\Phi}{dt}. \tag{2.8b}$$

In equation 2.8b the magnetic flux and the magnetic voltage is introduced. The magnetic flux describes the overall field induced in the material, where the magnetic flux density is the local field dependent on the surface. As one can see in equation 2.8 the measured voltage is the magnetic flux per time. In order to determine the flux density a simple transformation must be performed.

The above equations is only valid for one closed surface (e.g. one coil in a magnetic field). For a coil with N loops a first order approximation has to be made to determine the voltage for a whole coil

$$U(t) = \frac{d\Psi}{dt} \simeq N \cdot \frac{d\Phi_w}{dt} \tag{2.9}$$

Finally for the measurement the magnetic flux density is calculated with

$$\vec{B}(t) = \frac{1}{N_2 \cdot A \cdot \eta_{Fe}} \cdot \int U(t) \cdot dt = \frac{1}{N_2 \cdot A_{Fe}} \cdot \int U(t) \cdot dt \tag{2.10}$$

with the generally used variables

N_2 . . . . . secondary coil

A_{Fe} . . . . . iron surface

η_{Fe} . . . . . iron fill factor

The iron fill factor is a compensation factor if the material does not consist only of magnetic material (e.g. air between layers of electro frames). It is the verhältnis of the magnetic surface per whole surface

$$\eta_{Fe} = \frac{A_{Fe}}{A} \approx \frac{\sum_i m_{Fe_i}}{m_{ges}} \tag{2.11}$$

In this thesis this factor is needed, because for one sample three rings are glued together. The glue can not be magnetized but enlarges the magnetic surface of the sample in which eddy currents may occur. Therefore the iron fill factor η_{Fe}

has to be $\geq 85\%$ to get acceptable signals from the material only.

2.2 Ferromagnetism

A simple approach in ferromagnetism is that, a magnetic material consists of an assembly of permanent magnetic moments $\vec{m}_i$ of quantum-mechanical origin. Especially from the spins of electron. It is also postulated that even at low fields the material exhibits a large spontaneous magnetization. Other than in paramagnetism, the magnetic moments interact with each other (exchange interaction) and therefore add an energy term in the form of

$$H_{heis} = -2 \sum_{ij} J_{ij} \vec{s}_i \vec{s}_j \tag{2.12}$$

A problem with the spontaneous magnetization theory is, that a ferromagnet would magnetize itself until it is saturated. This has not been observed. To overcome this inconsistency, Weiss proposed that a ferromagnetic material is divided by magnetic domains. In every domain some magnetic moments are aligned dictated by a molecular field. The orientation of the spontaneous magnetization can change from domain to domain. This may result in a zero magnetic field, when no external field is applied, which reflects the real situation [35].

2.2.1 Magnetic Hysteresis

The hysteresis of a ferromagnetic material, below the Curie temperature, characterizes this material. In 2.2 is a classical hysteresis with all the parameters.

The magnetization $\vec{M}$ is coupled to an external alternating magnetic field $\vec{H}$, which aligns the domains in the structure. This alternation of the field $\vec{H}$ changes the energy balance of the ferromagnet and rearranges the domain structure, through the motion of interference layers (domain walls), which separates those domains. An overview of the work of Huber and Schäfer and will not be explained in detail [14].

2.2.2 Characterisation

Ferromagnets are divided in soft- and hard magnetic. The coercive field strength is used as a boundary to distinguish it. Materials with $H_c < 1000 A/m$ (measured
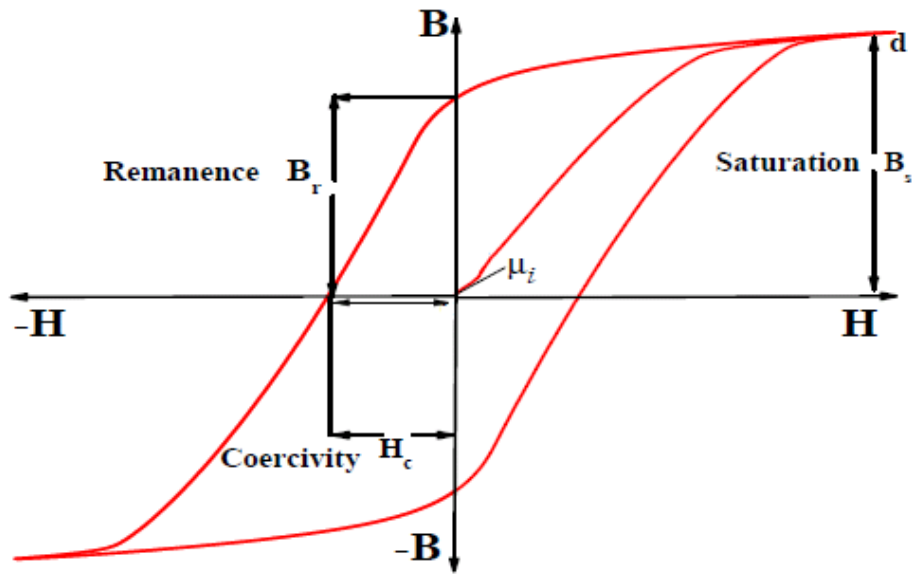
Figure 2.2: Hysteresis of a soft magnetic material with the important parameters, which describe such a curve [25, p.7]

at a static field) are usually described as soft magnetic. The difference include the obvious coercive field strength and therefore the losses and the theoretical approach.
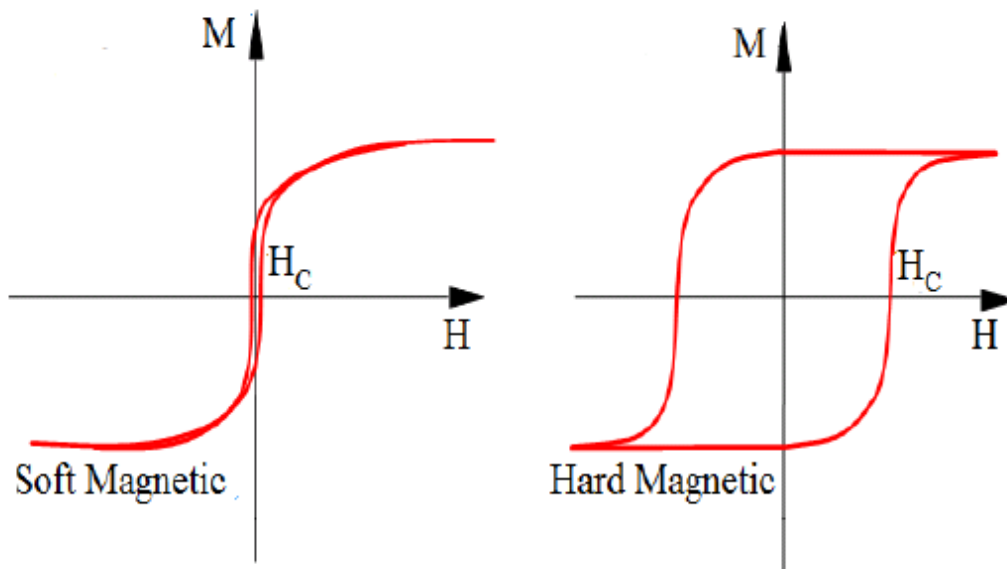
Figure 2.3: Hysteresis of a soft- and hard magnetic material [25, p.3]

2.2.3 Law of Approach to Saturation

To achieve real saturation magnetization it is necessary to apply very high fields. This is rarely possible, because there would be a high powered field coil or super conducting permanent magnet. Furthermore it is often not necessary to measure soft magnetic materials at high fields. As described in 2.2.2 the hysteresis is very narrow and has a high gradient (high permeability).

Saturation means that all the Magnetization vectors $\vec{\alpha}$ are almost aligned to the applied field $\vec{H}$. That means the angle θ between the magnetization $\vec{M}$ and the field $\vec{H}$ approaches zero. The magnetization now reads

$$\vec{M} = M_{sat}\cos(\theta) \approx M_{sat}\left(1 - \frac{\theta^2}{2} + \frac{\theta^4}{24} - \ldots\right) \tag{2.13}$$

An approach to the behaviour on the angle is that the magnetic field introduces a torque which will be encountered by the anisotropy E_K [24].

$$M_{sat}\mu_0 H\sin(\theta) = -\frac{\partial E_K}{\partial \theta} \tag{2.14}$$

Since the θ is very small, the assumption $\sin(\theta) \approx \theta$ is valid and now θ gets a dependency on the applied field $\vec{H}$

$$\theta = \frac{-\partial E_K/\partial \theta}{M_{sat}\mu_0} \cdot \frac{1}{H} \tag{2.15}$$

Compared with experiments $\theta(H)$ is not the only term influencing the saturation. Equation 2.15 includes only even terms in $\vec{M}$. It turned out that additional anisotropy terms as well as a term which suppresses spin waves induced by the field must be added. Now the law of approach to saturation reads [11]

$$M(T, H) = M(0, H) \cdot (1 - \frac{a}{H} - \frac{b}{H^2} - \ldots) + \gamma\sqrt{H} \tag{2.16}$$

with
$M(0, H)$ .. magnetization at 0K
a,b,γ .... parameters for the fit function

2.2.4 Crystal Structure

FeSi alloys have a body centered cubic (BCC) structure. Furthermore the grains can be oriented and non-oriented, which is set in the manufacturing process. M400-50A is a non-oriented silicon steel and the structure is shown in fig. 2.4.
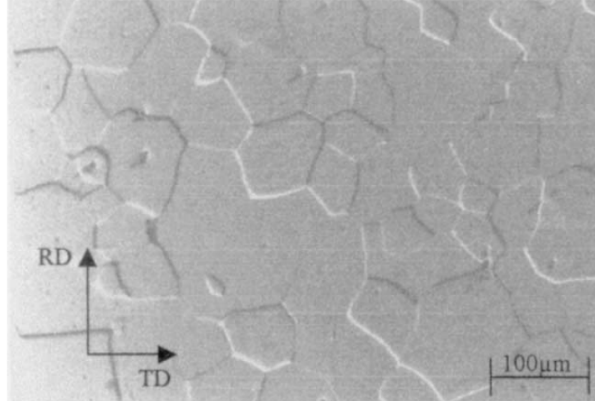
Figure 2.4: Typical grain distribution of non-oriented silicon steel [15]

The difference of the grain orientation sets the preferred magnetization direction. In a non-oriented silicon steel the magnetic properties have the same value in every direction (isotropic) [31].

2.3 Magnetostriction

The effect when a material changes it dimensions under a magnetic field, and therefore magnetizing the material, is called magnetostriction (MS). It is represented dimensionless as the relative length change

$$\lambda = \frac{\Delta\ell}{\ell_0} = \frac{\ell(\vec{M}, T) - \ell_0(\vec{M}_0, T_0)}{\ell_0(\vec{M}_0, T_0)} \tag{2.17}$$

In this context ℓ_0 at a starting magnetization $\vec{M}_0$ (preferable the material is demagnetized with $\vec{M}_0 = 0$) and starting temperature T_0, is the length before a field is induced. The temperature change must also be considered because of the heating due to the induction.

The magnetoelastic (MEL) energy is connected with the magnetoelastic stress σ_{mel} through a elastic constant c_{el} with $E_{mel} = \int_0^{\varepsilon_{ms}} \sigma_{mel} d\varepsilon_{me} = \frac{1}{2}c_{el} \cdot \varepsilon_{ms}^2$ and therefore linked to the magnetostriction. One can see that it has similarity with the mechanical elastic energy [6, p.3]. In mechanics the relative length change

is usually described as strain ε and therefore the ansatz for the polycrystalline magnetostriction

$$\lambda(\vec{M}, \vec{\beta}) = \sum_{i,j} \varepsilon_{ij} \beta_i \beta_j \tag{2.18}$$

can be made. This relation puts all dependencies of magnetization $\vec{M}$, Temperature T, ... in the magnetostrictive strain $\varepsilon_{ms} = \varepsilon_{ij}$ [6, pp.1].

2.3.1 Magnetic Free Energy

Becker and Döring developed an expansion to describe magnetostriction in a cubic symmetry lattice considering magnetization $\vec{M}$ and connecting all other influences with the expansion parameters h_i with increasing order [2]

$$\begin{aligned}
\lambda = \frac{\Delta\ell}{\ell}[T, H, \alpha_i, \beta_i] = & h_0 + h_1(\alpha_1^2\beta_1^2 + \alpha_2^2\beta_2^2 + \alpha_3^2\beta_3^2 - 1/3) + \\
& + 2h_2(\alpha_1\alpha_2\beta_1\beta_2 + \alpha_2\alpha_3\beta_2\beta_3 + \alpha_1\alpha_3\beta_1\beta_3) + \\
& + h_3(\alpha_1^2\alpha_2^2 + \alpha_2^2\alpha_3^2 + \alpha_1^2\alpha_3^2) + \dots
\end{aligned} \tag{2.19}$$

with
h_i ...... Becker and Döring magnetostriction constants
α_i ...... mangetization vector $\vec{M}$
β_i ...... direction of the strain

The magnetic free energy E_m includes all the magnetic and mechanical properties of the crystal. Specifically of three terms, the magnetocrystalline anisotropy (MCA) anisotropy energy F_k, the magnetoelastic energy E_{mel} and the elastic energy F_{el}.

$$F_k(\vec{\alpha}) = K_i\alpha_i + K_{ij}\alpha_i\alpha_j \qquad + \dots + K_{ijkl}\alpha_i\alpha_j\alpha_k\alpha_l \tag{2.20a}$$

$$E_{mel}(\vec{\alpha}, \varepsilon_{ij}) = \qquad\qquad \overline{M}_{ijk}\alpha_i\varepsilon_{jk} + \overline{M}_{ijkl}\alpha_i\alpha_j\varepsilon_{kl} \tag{2.20b}$$

$$F_{el}(\varepsilon_{ij}) = \qquad\qquad\qquad c_{ijkl}\varepsilon_{ij}\varepsilon_{kl} \tag{2.20c}$$

The indices of ε_{ij}, K_{ij} and α_i refer to sum over the three dimensions and the variables with four indices refer to the sum using Voigt's notation, which will be

described below. Each energy term must be invariant against the crystal symmetry operation group G (inversion, rotation, reflection planes) of a cubic crystal system [20]. To get an invariant expression some operators must be defined to cover the three main symmetry operations for a cubical crystal. With such tensors the MEL energy reduces (up to fourth order in $\vec{\alpha}$) to

$$F_K = K_1(\alpha_1^2\alpha_2^2 + \alpha_2^2\alpha_3^2 + \alpha_1^2\alpha_3^2) \tag{2.21}$$

under consideration that the anisotropy constant K_i has in all three axis the same value [6, pp.7]. Similar simplifications can be made for the elastic energy. In the work of Nye can be reduced to

$$F_{el} = \frac{1}{2}c_{11}(\varepsilon_{11}^2 + \varepsilon_{22}^2 + \varepsilon_{33}^2) + c_{12}(\varepsilon_{11}\varepsilon_{22} + \varepsilon_{22}\varepsilon_{33} + \varepsilon_{11}\varepsilon_{33}) + 2c_{44}(\varepsilon_{12}^2 + \varepsilon_{13}^2 + \varepsilon_{23}^2)$$
$$\tag{2.22}$$

introducing the Voigt's notation for the elastic constants $c_{ujkl} \rightarrow c_{nm}$ [28] In section 7.1 it will be determined that the elastic energy F_{el} is reduced when the crystal is strained. Same considerations were made for the MEL energy E_{mel}. Here also the symmetry of the magnetostrictive strain ε_{ij} and the magnetoelastic constants is used, which leads to

$$E_{mel} = \overline{M}_1(\alpha_1^2\varepsilon_{11} + \alpha_2^2\varepsilon_{22} + \alpha_3^2\varepsilon_{33}) + 2\overline{M}_2(\alpha_1\alpha_2\varepsilon_{12} + \alpha_2\alpha_3\varepsilon_{23} + \alpha_1\alpha_3\varepsilon_{13}). \tag{2.23}$$

The tensors ε_{ij}, K_{ij} and $\overline{M}_{ijkl}$ describe the direction of the strain depending on the location in the axis system. It is the same reason that there are four indices although only three dimensions are described. This so called Voigt notation compensates for the symmetry of the tensors of ε_{ij} and K_{ij} and simplifies the notation of the sum over $(i = 1, 2, 3)$. A detailed derivation of how to handle this notation is in A.1 for the elastic energy F_{el} but the principle is the same for the other energies.

With the free energy it is now possible to calculate the equilibrium of the strain at a constant stress $\tilde{\sigma}$ to determine anisotropic magnetostriction depending on the magnetoelastic $\overline{M}_i$ and elastic constant c_{ij}

$$\frac{\partial}{\partial \epsilon_{ij}} \left[F_K + E_{mel} + F_{el} \right]_{\tilde{\sigma}=const} = 0 \qquad (2.24)$$

After the derivation there is a linear system of six equations with the solution

$$\overline{\varepsilon_{ii}} = \overline{M}_1 \frac{(c_{12} - (c_{11} + 2c_{12})\alpha_i^2)}{(c_{11} - c_{12})(c_{11} + 2c_{12})}, \quad \overline{\varepsilon_{ij}} = -\frac{\overline{M}_2 \alpha_i \alpha_j}{2 c_{44}} \qquad (2.25)$$

This expressions can now be inserted into equation 2.18 and the anisotropic magnetostriction $\lambda(\vec{\alpha}, \vec{\beta})$ in any direction β can be calculated. After shifting terms in the equation the resulting terms correspond to terms of 2.19. For measurements the first three terms (h_0, h_1, h_2) are sufficient to compare with the theory. Higher order terms are small and can be neglected, also the function may start to oscillate and more boundary conditions may be needed (quantum effects). The necessary constants now show

$$h_0 = 0, \quad h_1 = \lambda_{100} = -\frac{2}{3}\frac{\overline{M}_1}{c_{11} - c_{12}}, \quad h_2 = \lambda_{111} = -\frac{1}{3}\frac{\overline{M}_2}{c_{44}} \qquad (2.26)$$

The expansion parameters can be related to the magnetization, specifically h_1 is a strain along [100] for $M\|[100]$ and h_2 for $M\|[111]$. $h_0 = 0$ corresponds to the initial state which will be demagnetized. Now the anisotropic magnetostriction with the MEL constants is [6, pp.8]

$$\begin{aligned} \lambda(\vec{\alpha}, \vec{\beta}) = \quad &\frac{3}{2}\lambda_{100}(\alpha_1^2\beta_1^2 + \alpha_2^2\beta_2^2 + \alpha_3^2\beta_3^2 - 1/3) + \\ &+ 3\lambda_{111}(\alpha_1\alpha_2\beta_1\beta_2 + \alpha_2\alpha_3\beta_2\beta_3 + \alpha_1\alpha_3\beta_1\beta_3) \end{aligned} \qquad (2.27)$$

As it will be shown in section 6 this constants can be calculated and connected to the stress σ_x in the deformation direction and to the magnetization process $\vec{M}$ (in this case α_i).

2.3.2 Magnetostriction in the Magnetization Process

Lee proposed that the magnetization is directly linked to the magnetostriction, especially that the magnetostriction also follows a hysteresis. It also can be seen that the magnetostriction also follows different curves in the main crystallographic directions. The domains in demagnetized state are equally distributed in $\langle 100 \rangle$. If the crystal is magnetized the MS corresponds to $180C°$ domain wall displacement,

which generates no spontaneous magnetization and therefore MS is zero. When the domains in $M_s||H$ are exhausted, magnetization in domains with $M_s \perp H$ starts to rotate effectively and MS starts to increase. When this $90C°$ domain walls disappear magnetization starts to saturate and also MS, because the spins start to align with increasing field $\vec{H}$. This considerations can also be made for the medium $\langle 110 \rangle$ and hard $\langle 111 \rangle$ axis [6, p.11].

Direction [100]

Before magnetization 1/3 of the domains are aligned to $< 100 >$ (evenly distributed). When $\vec{H}$ increases domains with $M_s \perp H$ ($90C°$ domain walls) move until they disappear and this movement results in magnetostriction, which follows in the most simple way

$$\frac{\Delta \ell}{\ell} = \frac{3}{2}\lambda_{100}(M - 1/3M_s), \qquad 1/3M_s < M < Ms \qquad (2.28)$$

This simplifications does not consider the movements of the domain walls in all direction. To calculate this rather complicated process, the domain wall orientation have to be seen as a probability distribution. This distribution is displayed as $n_{\pm x}$, $n_{\pm y}$, $n_{\pm z}$ with $\sum_i n_i = n$. With the initial state, that the domains volume are equally distributed the probability is

$$P(n_{\pm x}, n_{\pm y}, n_{\pm z}) = (1/6)^{n_x}(1/6)^{n_y}(1/6)^{n_z} \cdot \frac{n!}{n_x!n_y!n_z!} \qquad (2.29)$$

with the limitation that the only relevant magnetization is in x-direction (¡100¿) the ansatz boundary for the distribution is

$$M = M_s(n_x - n_{-x})/n \qquad (2.30)$$

With variation and experimental magnetostriction data the distribution arrives at $n_x = n_y e^{\nu}$, $n_{-x} = n_y e^{-\nu}$ and $n = n_y(4 + 2\cosh(\nu))$. ν represents the variation scale depending on the magnetization which now calculates to

$$M = M_s\frac{sinh(\nu)}{2 + \cosh(\nu)} \qquad (2.31)$$

and so gives the final magnetostriction compared with the ansatz from 2.28

$$\frac{\Delta\ell}{\ell} = \lambda_{100}\left(\frac{n_x + n_{-x}}{n} - \frac{1}{3}\right) = \lambda_{100}\left(\frac{\cosh(\nu)}{2 + \cosh(\nu)} - \frac{1}{3}\right) \qquad (2.32)$$

In this equation can be seen that with the magnetostriction one can obtain a good deal of information about the magnetization [6, pp.10].

Direction [111]

In the axis of [111] the magnetostriction is only non zero until domains are equally distributed. With increasing $\vec{H}$ until $M = M_s/\sqrt{3}$ the magnetization rotates towards $\vec{H}$ within the domain (see figure 2.5), following $M = M_s \cos(\theta)$ now with $\beta_i = 1/\sqrt{3}$.
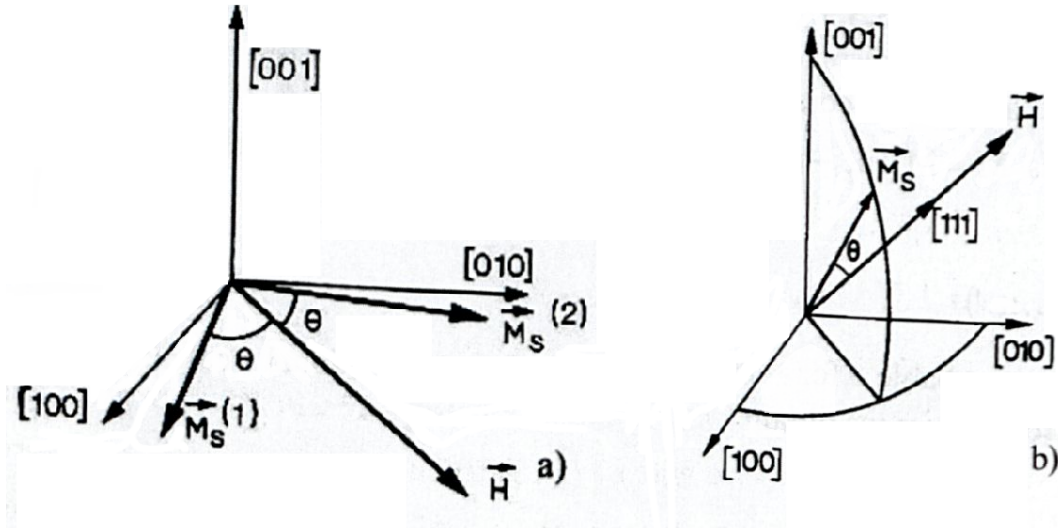
Figure 2.5: Magnetization relative to $\vec{H}$ of two adjacent domains separated by a 90° wall [6][p.12]

With the help of 2.19 and the condition $\cos^2(\theta) = (1/3)(1 + 2(\alpha_1\alpha_2 + c.p.))$the MS for [111] transforms to

$$\lambda = \frac{\Delta\ell}{\ell} = \lambda_{111}(\alpha_1\alpha_2 + \alpha_2\alpha_3 + \alpha_1\alpha_3)$$
$$= (1/2)\lambda_{111}(3\cos^2(\theta) - 1) = (1/2)\lambda_{111}(3(M^2/M_s^2) - 1) \qquad (2.33)$$

This equation agrees with the experiment as seen in 6.5, because rotational magnetization and domain wall do not occur simultaneously [6, p.12].

2.3.3 Polycrystalline magnetic materials

As previous mentioned magnetostriction also follows a hysteresis curve and so there must be connection between $\lambda(\vec{H})$, the MCA constant K_1 and the magnetostriction in λ_{ijk} in easy and hard direction for cubic crystalline ferromagnets.

In this section the spontaneous or technical saturation magnetostriction λ_{sat} at the end of the magnetization process will be calculated. In order to arrive at a general solution all grain orientations have to be equally probable in the polycrystalline structure. This assumption is valid for the electrical steel provided for this work, due to the warm rolling manufacturing of the steel sheets. The necessary magnetostrictions are the anisotropic magnetostriction λ_t and the volume magnetostriction ω, which can be shown as

$$\lambda_t = \lambda_\parallel - \frac{\omega}{3} = \lambda_\parallel - \lambda_\perp, \qquad \text{with} \quad \omega = \lambda_\parallel + 2\lambda_\perp \tag{2.34}$$

where $\lambda_\parallel$ is the MS along the field $\vec{H}$ and $\lambda_\perp$ the magnetostriction normal to $\vec{H}$ [6, p.21].

For a cubic polycrystalline the formula 2.19 of Becker and Döring can be used. Now the spontaneous magnetostriction for the saturated and the demagnetized state will be averaged and then subtracted. In figure 2.6 is the coordinate system used for the calculation, which transforms after some trigonometric considerations to

$$\alpha_1 = \cos\xi \sin\theta \cos\phi + \sin\xi(\cos\theta \cos\phi \cos\psi + \sin\phi \sin\psi) \tag{2.35a}$$

$$\alpha_2 = \cos\xi \sin\theta \sin\phi + \sin\xi(\cos\theta \sin\phi \cos\psi + \cos\phi \sin\psi) \tag{2.35b}$$

$$\alpha_3 = \cos\xi \cos\theta - \sin\xi \sin\theta \cos\psi \tag{2.35c}$$

$$\beta_1 = \sin\theta \cos\phi \qquad \beta_2 = \sin\theta \sin\phi \qquad \beta_3 = \cos\theta \tag{2.35d}$$

This also shows that the angle ξ between the magnetostriction direction $OX(\theta, \phi)$ and the magnetization direction OY is constant. In cubic coordinates and for random grains orientation the spontaneous magnetostriction over the whole crystal reads

$$\overline{\lambda} = \frac{1}{8}\pi^2 \int_0^\pi \int_0^{2\pi} \int_0^{2\pi} \lambda \sin\theta \, d\theta d\phi d\psi \tag{2.36}$$

The solution can be comprehended in A.2 and the solution for the polycrystalline spontaneous magnetostriction gives

$$\lambda = \frac{3}{2}\lambda_s \left(\cos^2(\xi) - \frac{1}{3} \right) \tag{2.37}$$

where the factor from the saturation magnetostriction λ_{sat} now can be related with 2.34 to

$$\lambda_\parallel - \lambda_\perp = \frac{3}{2}\lambda_{sat} = \frac{2}{5}h_1 + 3/5\,h_2 + \dots \tag{2.38}$$

With this equation the saturation magnetization λ_{sat} can be calculated with the measurement of $\lambda_\parallel$ and $\lambda_\perp$. The third term contains all the expansion constants which can be connected magnetoelastic constants and therefore to the magnetic free energy E_m [6, pp.20]. With the magnetic free energy there can be a conclusion made to the magnetocrystalline anisotropy constants K_i, the magnetoelastic stress constants $\overline{M}_i$ and the elastic constants c_{ij}. Especially the elastic energy F_{el} depends on the internal and/or external stress (which also influences $\overline{M}_i$). This will be used in section 7.1 to identify the deformation and the altered form of both the magnetic and magnetostriction hysteresis. It is also possible to connect λ_{100} and λ_{111} with the relation of 2.38.
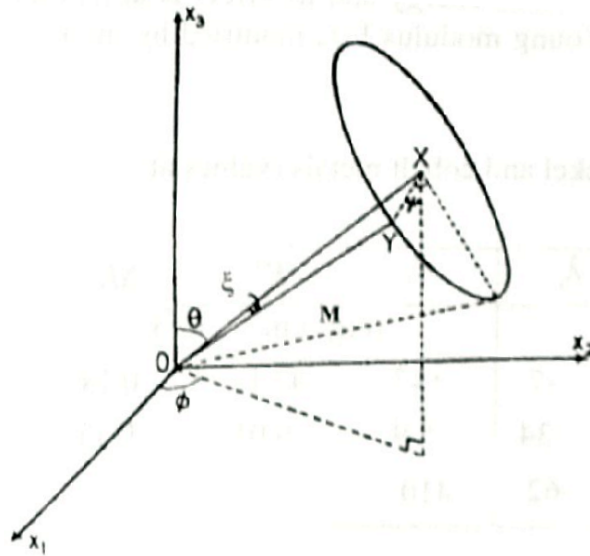
Figure 2.6: Magnetization α_i and magnetostriction direction β_i [1, p.25]

2.3.4 Applied stress and magnetoelastic anisotropy

A magnetized ferromagnet crystal changes the magnetization direction α when deformed. This is the inverse magnetoelastic effect or Villari's effect [38]. Therefore it can be concluded that MS is caused from an internally developed magnetoelastic stress. To include external stress the magnetocrystalline anisotropy energy will be expanded with a magnetoelastic anisotropy (MELA) term. With this information, the magnetic free energy can be expanded in terms of strains [21]

$$F_m = F_K^0 + \frac{\partial F_K}{\partial \varepsilon_{ij}} \varepsilon_{ij} + \frac{1}{2} \frac{\partial^2 F_K}{\partial \varepsilon_{ij} \partial \varepsilon_{kl}} \varepsilon_{ij} \varepsilon_{kl} \tag{2.39}$$

with F_K^0 is the MCA energy for a unstrained crystal. The second term relates to MEL constants, which will be defined as

$$\frac{\partial F_K}{\partial \varepsilon_{ij}} = \overline{M}_{ijkl} \varepsilon_{kl} \tag{2.40}$$

which reduces to $\overline{M}_1$ and $\overline{M}_2$ for a cubic symmetry. The solution of the equilibrium states 2.25 now inserted in the elastic and magnetoelastic energy with the condition above gives the total magnetoelastic anisotropy energy for the deformed crystal

$$F_K = (K^0 + \Delta K)(\alpha_1^2 \alpha_2^2 + \alpha_2^2 \alpha_3^2 + \alpha_1^2 \alpha_3^2) \tag{2.41}$$

where K^0 is linked to the unstrained crystal and

$$\Delta K = \frac{\overline{M}_1^2}{c_{11} - c_{12}} - \frac{\overline{M}_2^2}{2c_{44}} = \frac{9}{4} \left\{ (c_{11} - c_{12})\lambda_{100}^2 - 2c_{44}\lambda_{111}^2 \right\} \tag{2.42}$$

is the MELA energy [6, p.24]. With the knowledge of the anisotropy constant K_1 the MCA constant can be calculated with a reference sample (undeformed) and different strained samples.

To understand the magnetostriction under stress there two separate effects that take place. The *first order inverse magnetoelastic effect* depends on the direction γ of the stress. Here the stress tensor $\sigma_{ij} = \sigma \gamma_i \gamma_j$ and the induced strain ε_{ij} have to be inserted in the magnetic free energy E_m, which now depends on the magnetization $\vec{\alpha}$. Once again $\overline{M}_1$ and $\overline{M}_2 \cdot s_{44}$ can be identified as λ_{100} and λ_{111}

$$E_m = K_1(\alpha_1^2\alpha_2^2 + \alpha_2^2\alpha_3^2 + \alpha_1^2\alpha_3^2) - \frac{3}{2}\lambda_{100}\sigma(\alpha_1^2\gamma_1^2 + \alpha_2^2\gamma_2^2 + \alpha_3^2\gamma_3^2) - $$
$$- 3\lambda_{111}\sigma(\alpha_1\alpha_2\gamma_1\gamma_2 + \alpha_2\alpha_3\gamma_2\gamma_3 + \alpha_1\alpha_3\gamma_1\gamma_3) \tag{2.43}$$

The terms $-\lambda_{ijk}\sigma$ refer to the mechanical work if the mechanical stress by the magnetostriction deformation. To determine the deformed strains ϵ_{ij} the new equilibrium direction α to M_s of the energy must be minimized against α [6, pp.25]. This calculation is rather complicated and for real situation can only be solved numerical. Therefore the magnetostriction λ_{ijk} due to deformation will be determined empirically with the measurement data.

The *second order magnetoelastic effect* takes to account if the stress is constantly applied or removed, which leaves the crystal deformed and therefore with different strains ε_{ij} in the lattice. This deformed state of the lattice changes the form of the magnetostriction curve also [6, pp.25]. This can be calculated for constant applied stress but was never proved for deformed material, like the samples in this work.

2.3.5 Residual Stress and Coercive Field Strength

Using the measurements of the coercive field strength H_C and the magnetostriction the residual stress can be calculated using

$$H_c = \frac{\sigma_{res} \cdot \lambda - \langle K_{eff} \rangle}{\mu_0 M_s} \tag{2.44}$$

with the effective magnetocrystalline constant $\langle K_{eff} \rangle$ and the magnetostriction λ [33].

$\langle K_{eff} \rangle$ will be calculated using the „Reference" sample, where the induced stress is estimated with $\sigma_{res} = 1.95\,MPa$. The magnetostriction λ is not the saturation magnetostriction λ_s, but can be calculated according to eq. 2.38. This relation only is valid for undeformed materials, as it will be shown in 6.5, the *anisotropy saturation constant* γ must be multiplied to arrive at λ_s.

2.3.6 Calculate Measurement Data

As it will described in 4.3.1 strain gauges were used to measure magnetostriction. The measured signals are voltages and with equation 2.45 they can be transformed

to a physical expression which relates to magnetostriction.

$$\lambda_i[ppm] = U(t) \cdot \frac{S_{range}}{U_B \cdot k} \tag{2.45}$$

with

λ_i ...... magnetostriction in longitudinal or transverse

S_{range} ... measuring Range (accuracy)

k ...... calculating factor of the strain gauge

The strain gauges measure longitudinal $\lambda_\perp$ and transverse $\lambda_\parallel$ to the applied field $\vec{H}$. To arrive at the saturation magnetization one has to calculate as shown in 2.38.

2.4 Core Losses

When a conductive material is exposed to a time-varying magnetic field with the frequency, a annular current (*Eddy* currents) perpendicular to the field is induced. This current generates a field, which opposes the external field. This can go so far that the external field is shielded from the inside the material, which is called *Skin-Effect* [18]

$$\delta(f) = \sqrt{\frac{\rho}{\pi f \mu_0 \mu_r}} \tag{2.46}$$

with

δ ...... standard depth of penetration

ρ ...... specific resistivity

μ_r ...... relative permeability

It is important, that the external magnetic field strength $H(t)$ penetrates the material at least $\delta \geq d/2$ to ensure the materials magnetized fully.

Hysteresis Losses

The area of the hysteresis under static conditions ($f \rightarrow 0$) is expressed as hysteresis loss. It is the energy dissipated as heat in each magnetization cycle and will be introduced as

$$W_{hyst} = 4 J_{max} H_{hyst} \qquad (2.47)$$

If the hysteresis loop has a rectangular form (idealization), H_{hyst} coincides with the coercive field H_c and therefore is a good approximation to start the calculating. With the quadratic Rayleigh law for dissipative processes

$$M = \chi_{in} H_a + b H_a^2 \qquad (2.48)$$

the losses get a dependency $\propto H_{max}^3$. Given certain applied fields experiments from Rayleigh showed a relation from $W \sim J_{max}^2$ to $J_{max}^{3/2}$. [3, pp.310]. To generalize the exponent, the assumption $H_{hyst} \propto J_{max}^{\alpha}$ with the material dependent factor α. Usually values of 1.5-2.0 are found for soft magnetic materials and is commonly known as *Steinmetz law* [5].

Now the hysteresis loss can be expressed with two parameters. α is material dependent and k_h is a pre-factor to conclude the cycles of the magnetizations and other contributions such as deformation, temperature, ... [3, pp.426].

$$W_{hyst} = \frac{P_{hyst}}{f} = W_0 = k_h \cdot J_{max}^{\alpha} \qquad (2.49)$$

The saturation polarization J_s for all the samples have the same value the factor k_h also scales with J_s. Therefore instead of k_h the static losses $W_0 \hat{=} W_{hyst}$ will be calculated, which represents the losses at f=0Hz.

Classical Losses

This type of dynamic (eddy-current) losses can directly obtained from Maxwell's equations. The magnetic domains are averaged over the time and therefore have no contribution to the still macroscopic calculation. With the geometry in 2.1 Maxwell's equation from 2.8a can be simplified in only the y-direction, because the gap is much bigger than the height of the sample and the resulting field strength H is directed radial in the z-axis. With the definition of the current

density $\vec{j} = \sigma \cdot \vec{E}$, two differential equations have to be solved [3, pp.399]

$$\frac{\partial H}{\partial y} = j \tag{2.50a}$$

$$\frac{\partial j}{\partial y} = \sigma \frac{dB}{dt} \tag{2.50b}$$

The boundary conditions depend on the material to investigate. For ferromagnetic materials, in this case soft magnetic materials, a steplike function can be assumed (see figure 2.7).
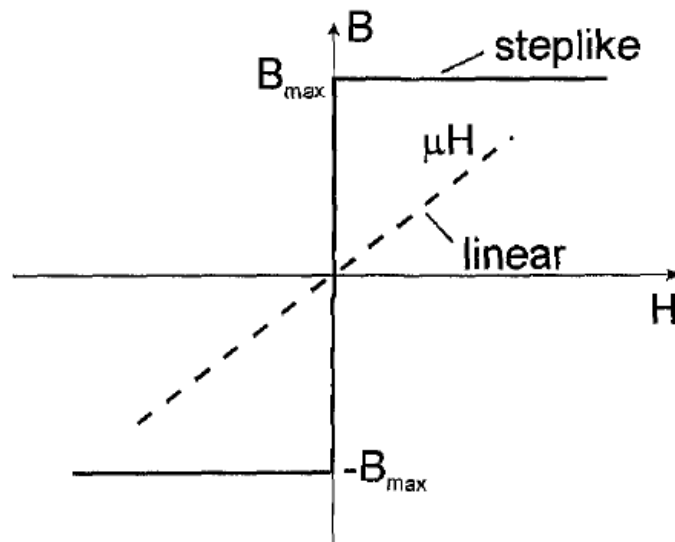
Figure 2.7: Linear and steplike magnetization law [3, p.404]

Also the material has to be assumed as homogeneous and the induced magnetic field penetrates the body from -y/2 to 0 and y/2 to 0 equally. In this case the magnetization corresponds with one-dimensional fronts propagating threw the material in the x-z pane. With this conclusion there are two symmetric fronts for each half period of the magnetization. The position of the fronts are now the

boundary conditions

$$y_{F,B\uparrow} = \pm\frac{d}{4}\left[\frac{B(t)}{B_{max}} - 1\right] \tag{2.51a}$$

$$y_{F,B\downarrow} = \mp\frac{d}{4}\left[\frac{B(t)}{B_{max}} + 1\right] \tag{2.51b}$$

where $y_{F,B\uparrow}$ stands the front under increasing B and $y_{F,B\downarrow}$ for decreasing B. Under considerations that $j = 0$ in the middle of the cross section (x-y pane) the differential equation in 2.50 can be solved, which leads to the solution

$$H_{cl}(t) = \frac{\sigma d^2}{8}\left[\left|\frac{dB}{dt}\right|\frac{B(t)}{B_{max}} + \frac{dB}{dt}\right] \tag{2.52}$$

which is the dynamic magnetization law. This field can now be inserted into 2.53 using the differential equation 2.50 from Maxwell's equation, which leads to the average loss per unit volume of the classical eddy current losses

$$\frac{P_{cl}}{f} = \int_0^{1/f} H_{cl}(t)\frac{dB}{dt} \cdot dt = \frac{\sigma d^2}{8}\int_0^{1/f}\left[\left|\frac{dB}{dt}\right|\frac{B(t)}{B_{max}} + \left(\frac{dB}{dt}\right)^2\right] dt \tag{2.53}$$

This equation transforms under sinusoidal induction $B(t)$ to $P_{cl} = \frac{\pi^2}{4}\sigma d^2 B_{max}^2 f^2$. In this work the commonly used loss equation [3, pp.407]

$$P_{cl} = \pi^2\sigma d^2 \cdot \beta \cdot B_{max}^2 f^2 \tag{2.54}$$

where β is a material constant, which can be determined using a fit-function and will be analysed in detail in the results. It is then possible to compare the variable β with the real solution in eq. 2.53 and a conclusion can be drawn of the deformation of the samples.

Excess Losses

The magnetic domains and the microstructure are the basis of the excess losses W_{exc}. This complex theory is not part of this thesis and is very good explained in the book of Huber [14]. With a linear approximation over the number of regions contributing to the magnetization

$$n(H_{exc}) = n_0 + \frac{H_{exc}}{V_0} + \ldots \tag{2.55}$$

one arrives at the relation

$$P_{ex}(f) = 8\sqrt{\sigma G \cdot S \cdot V_0} B_{max}^{3/2} \sqrt{f} \tag{2.56}$$

where V_0 contains all micro-structural influences, as well as the deformation and the factor G considers the geometry of the sample [3, pp.427].

Overall Losses

Adding all three loss terms, the frequency dependent losses lead to

$$W_{tot}(f) = W_0 + \left[\frac{\sigma d^2}{8} \int_0^{1/f} \left[\left| \frac{dB}{dt} \right| \frac{B(t)}{B_{max}} + \left(\frac{dB}{dt} \right)^2 \right] dt \right] \cdot f + \\ + 8\sqrt{\sigma G \cdot A_{fe} \cdot V_0} B_{max}^{3/2} \cdot \sqrt{f} \tag{2.57}$$

which will be determined using a fitting a function through the calculation of the area of a hysteresis loop at a certain frequency. The function used is now

$$W_{tot} = W_0 + C_1 \cdot f + C_2 \cdot \sqrt{f} \tag{2.58}$$

where the fitting constants W_0, C_1 and C_2 represent the individual part of the losses. The same relation can be applied for the coercive field strength H_c

$$H_c(f) = H_{c0} + H_1 \cdot f + H_2 \cdot \sqrt{f} \tag{2.59}$$

but the coefficients H_1 and H_2 could not yet be related to a physical process. Equation 2.59 is based on observations and the shape of the losses.

2.4.1 Unit Convention

Data sheets of magnetic materials often show the losses in different ways. From the integration of the hysteresis loops the natural units are J/m^3. This characterizes the energy which lost during the remagnetization process per volume unit. If the materials density is known another representation of the losses is in J/kg,
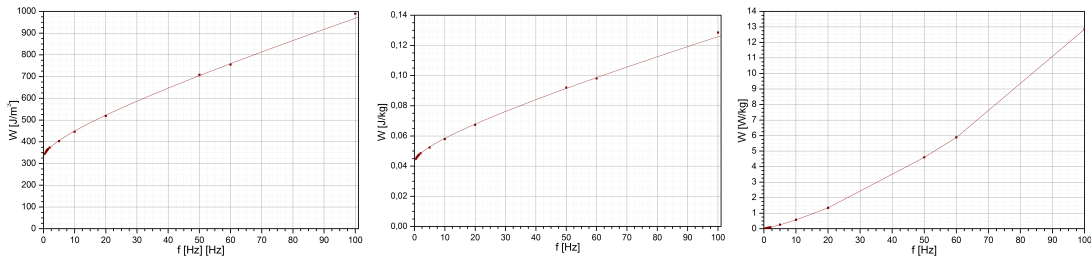
Figure 2.8: Different representation of the overall losses of M400-50A

which in this case classifies the energy per material mass. The last unit depends on the frequency of the measurement and is W/kg and is the power lost in the remagnetization process. In equation 2.60 are the calculation steps to acquire the desired units and in figure 2.8 are the frequency dependent losses for M400-50A electrical steel for the above mentioned units. This work will use the most commonly used J/m^3.

$$\int \vec{B}\,[T]d\vec{H}\,[A/m] \to J/m^3 \xrightarrow{\,:\rho\,[kg/m^3]\,} J/kg \xrightarrow{\cdot f\,[Hz]} \frac{J}{s \cdot kg} = W/kg \qquad (2.60)$$

2.5 Mathematical Approximations

In the complex field of magnetism not all properties can be measured, due lack of measuring equipment or the property is not needed. Therefore it is possible to calculate some properties with verified theories. In following section the functions used in this thesis are described.

Smoothing

In some cases it is necessary to filter the noise of the acquired signal. Especially the magnetostriction signal is very small and therefore also has a high noise. With the data analysis program „ORIGIN" it is possible to smooth signals with special smoothing algorithm. In the case at hand the „Savitzky-Golay" algorithm was used. The speciality with this algorithm is that certain frequencies, overlapping the signal, can be suppressed. Such smoothing is justified if the noise is evenly distributed an no beats or spikes are in the signal.

Integration and Derivation

To analyse the measured voltages advanced mathematics operations have to be made. The magnetic flux density $\vec{B}(t)$ for example, arrives from integration of the magnetic flux $\frac{d\varphi(t)}{dt}$. The measurement software uses a *Simpson* integration algorithm with opened boundary conditions. The derivations also use a numerical procedure. In this case the data is divided by the step width (Δt) for every dataset. Since the step size is around 1.25E-6 even simple trapezoid summation would suffice.

3 Deformation Process

As described in section 1. most of the samples were deformed. To study the effect of deformation some of the samples had to be deformed under controlled conditions. The group of Prof. Zehetbauer has the knowledge and the equipment to apply well defined stresses by a rolling process. With the help of his students Dr. Florian Spieckermann and Gerald Weger MSc., it was possible to strain and deform steel stripes by a rolling machine.

The punching samples were manufactured by „AIT Ranshofen" and the tool designed by Dieter Horwatitsch. He has experience in the punching process and also helped to pick the sample properties for the punching.

3.1 Definitions

To confirm the theoretical approach of hysteresis losses in deformed material it is important to deform the samples. The deformation has to be homogeneous, because this process can be comprehended and the texture of a constant deformation can be measured. Also the comparison between a undeformed and a controlled deformation gives information what happened due to the deformation process.

In figure 3.1 the complete sample preparation is shown. The samples for this thesis were made out of blank M400-50A electro steel sheets. This sheets are used directly in the industry. They were produced by a final cold rolling process and therefore some deformation from the manufacturing process were present. There were three manufacturing routes divided into the different steps taken by the producing facility:

Vienna University of Technology
- Cutting the sheets into stripes
- Stress-Free glowing of the stripes

University of Vienna
- Tensile tests
- controlled tensile and rolling deformation

AIT Ranshofen
- Designing the punching tool
- Punching the samples with different parameters

Blank Sheet
M400-50A

Cutting Strips

50mm and
60mm strips

Untreated

Stress-Free Glow

Undeformed   Rolling   Strain

Lasercutting

Punching

8 Samples:
- Untreated
- Undeformed
- 3 Rolled
- 3 Strained

9 Samples with
different cutting
parameters

Figure 3.1: The workflow of the ring shaped samples, from the blank sheet
over the different deformation processes to the rings

3.2 Stress-Free Glowing

At the Vienna University of Technology (VUT) are special oven to heat samples of different geometry. In figure 3.2 is the laboratory furnace which was used to heat treat the stripes.

Figure 3.2: The Hareaus M1100 laboratory oven to stress-free glow the metal stripes

The heat treatment process ensured that all the stripes had the same initial state regarding their stress state. This was necessary, because the metal sheets were manufactured under industrial conditions. In this case the sheets were cold rolled and cut at a certain length. This, by the production caused deformation, can interfere with the experimentally controlled deformation. Also the initial deformation varies from sheet to sheet and therefore can cause also statistical problems.

  The heating process and especially the stress free glowing is not so well defined, because there is no specific temperature to remove all deformations from the manufacturing. The heat treatment temperature has to be high enough to enable diffusion processes to remove dislocations, on the other side it has to be below any phase transformation temperature. For this purpose one has to consider the phase diagram which is for Fe-Si well known. In figure 3.3 is the phase diagram for Fe-Si, which was used to determine the heat treatment temperature.
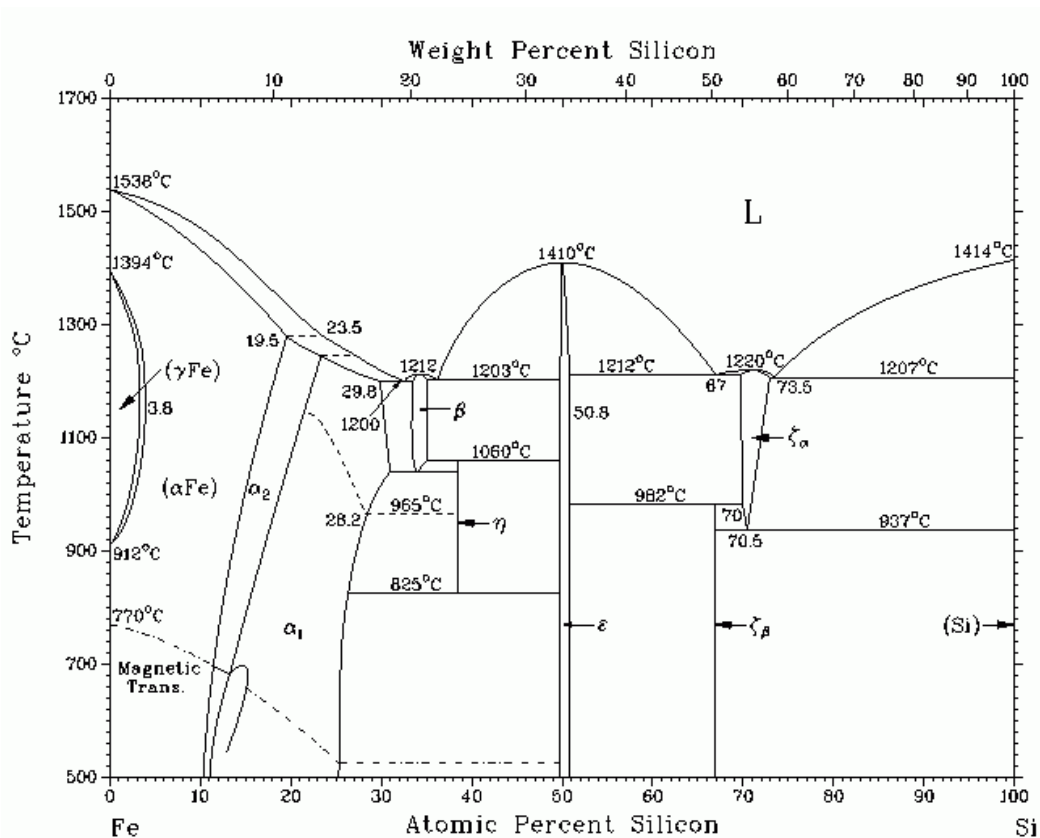
Figure 3.3: Phase diagram for FeSi [30]

On the x-axis the atomic percentage of silicon is drawn whereas on the y-axis the temperature in °C is given. In the present work the Si-content is about 3% and therefore our alloy is located on the far left side of the diagram. Considering the phase diagram it is easy to see, that a too high heat treatment temperature can change the crystal structure from A2 (statistical) to B2 (preferential) which are all BCC but describes different Si positions in the lattice.

As discussed earlier it is necessary to determine the heat treatment by considering boundary conditions:

- the temperature has to be not too high ($< 1000\,C°$)
- preheating and cooling with time is important - see phase diagram
- the temperature of the furnace has to be homogeneous over the sample dimensions

Considering these conditions the temperature for the heat treatment was chosen as $400-500C°$ over 4 hours. In figure 3.4 the heating-up, plateau and the cooling

process is shown as function of the time. The x-axis in mm in the figure represents the sample position in the furnace. In order to stack more stripes, thin chamotte spacers were used.
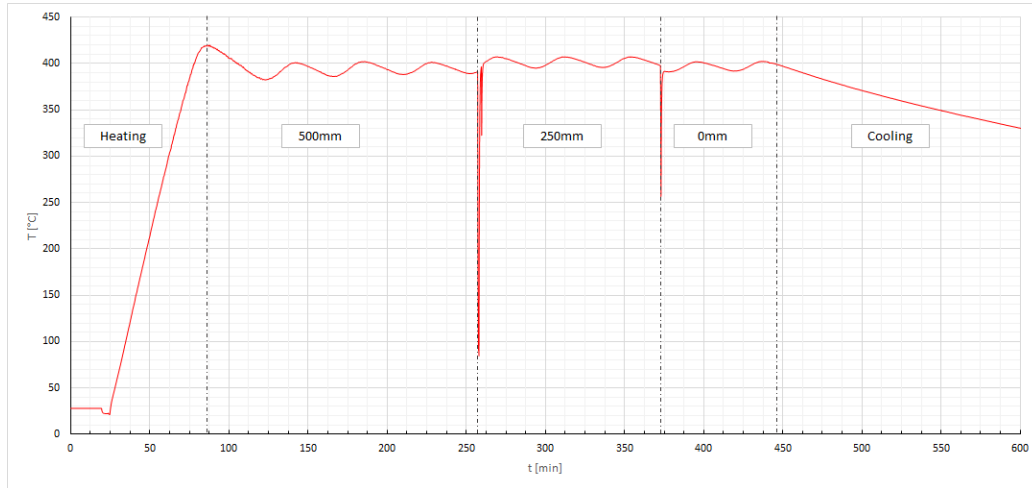
Figure 3.4: Heating diagram of Hareus M1100 oven for the glowing period and positions in the chamber

The sinusoidal behaviour is the result of the control circuit of the oven. In modern oven this behaviour would not appear due to the better control circuits and better heating coils. The temperature difference of $\sim 20C°$ did not make a difference, because of the long duration of the heating. The only important conditions for all the stripes is, that they had to be glowed under the same conditions, which means that all the samples had the same initial state. Table 3.1 lists the heating parameters for M400-50A stripes, although all stripes of different composition were glowed (M330-35A, M330-50A).

The oscillations at the top are caused by the regulator of the furnace. The temperature oscillations of $\sim 20\,C°$ are not problematic, because for removing internal stresses and dislocations an accurate heat treatment is not necessary. Only important for our experiments is, that the heat treatment has to be the same for all stripes, which means that all samples shall achieve the same initial state. Table 3.1 lists the heating parameters for the M400-50A stripes, although all other stripes of different composition (M330-35A, M330-50A) were heated too.

Batch	Temperature [$C°$]	Warm-Up Time [min]	Glowing Time [min]	Cooling Time [min]
4 Tensile 1 Glowed	450	83	270	1553
4 Rolled	440	81	270	1521
5 Cutted	450	83	271	1544
5 Cutted	460	87	275	1550
5 Cutted	450	83	271	1539

Table 3.1: Properties of the stress free glowing of the steel stripes used for the ring samples of the M400-50A stripes

3.3 Tensile Test

A well controlled deformation experiment can be performed by a tensile test. This was made by an ISO60880 tensile test machine provided from the department of „Physics of Nanostructured Materials" from the University of Vienna. For this purpose, heat treated stripes of M400-50A with a width of 60mm were needed. The machine works with a hydraulic stamp and a maximum force of 45 kN can be applied. The strain is measured via two tapes on the clamped stripe (see figure B.1). A camera measures the length change while the machine pulls the stripe with a velocity of 24 mm/min. The resulting force is also measured and by knowing the cross section, the stress in the material can be calculated. All important data of the stress experiments on the samples (dimensions, strain,...) are listed in the appendix B.

The tensile machine can be adjusted to stop at a specific strain. It has to be noted that the measured strain is not the real strain induced in the material. There is always an elastic component which counters the effect of any load. Therefore the strain as achieved in the diagram ε_x has to be differenced from the real strain $\varepsilon_{plsatic}$ in the sample. To test the material until the limit, five breaking tests were performed and the stress-strain diagram is shown in figure 3.5. Only two of the graphs are shown, because the data was corrupted during measurement. Part of the data still could be used to calculate the specific points (e.g. Young's module E, R_m).
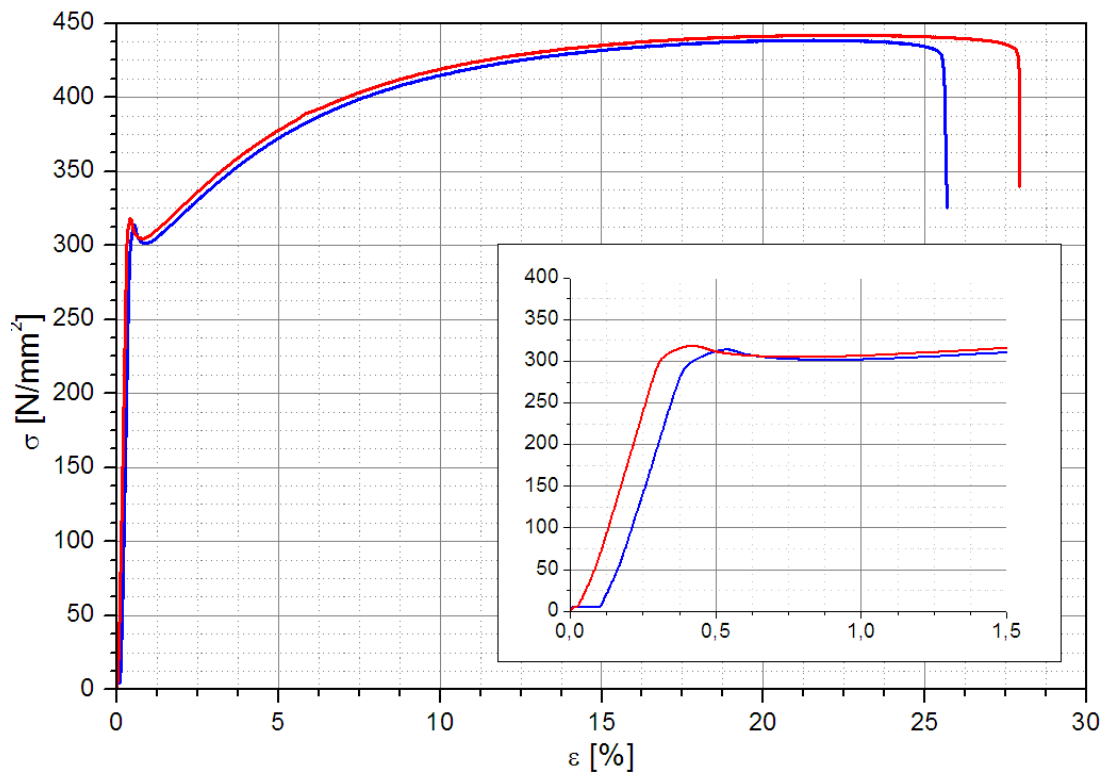
Figure 3.5: $\sigma - \epsilon$ graph from two of the five M400-50A strips. Tensile test until breaking point

With the data of the tensile tests common mechanical properties of the investigated material can be calculated and are summarised in table 3.2. These experimental data are compared with that given in a data sheet.

Property		σ
E_{rd}	199.3 GPa	2.05%
E_{td}	208.7 GPa	4.21%
R_m	445.7 N/mm²	3.53%
$R_{p0.2\%}$	310.6 N/mm²	2.89%
$R_{p0.2\%}$	310.6 N/mm²	2.89%

Table 3.2: Mechanical properties from the tensile tests for M400-50A

In the work of Iordoche it was stated, that the magnetic properties change with

increasing stress of the material. These properties vary until saturation is reached where no alteration is observed [17]. With this information the deformations for the samples were chosen according to the general formula

$$\varepsilon_x = \frac{\Delta x}{x_0} = \frac{x_1 - x_0}{x_0}.$$ (3.1)

In table 3.3 the parameters of the controlled tensile experiments are listed. The samples are named after the strain were the tests were stopped and not the real strain $\varepsilon_{plastic}$. x_0 refers to the initial distance between the tape and x1, the length after the release of the force. Even that the calculated strain ε_x differs from the actual one, the names of the samples stay according to the original strain.

Stripe Name	ε_x [%]	x_0 [mm]	x_1 [mm]
Tensile 0.5% − *G*	0.58	0.507	0.504
Tensile 2% − *G*	2.11	0.507	0.496
Tensile 4% − *G*	4.08	0.507	0.486

Table 3.3: Deformation parameters of the tensile strips

E_{rd} indicates the Young's modulus in rolling direction and E_{pr} perpendicular to the rolling direction. R_m is the yield strength, which is the maximum stress induced until the material breaks and $R_{p0.2\%}$ the strength at a plastic deformation from $\varepsilon = 0.2\,\%$. This value usually define a material for technical applications.

3.4 Rolling

With a rolling machine the second deformation experiment was accomplished, specifically a cold rolling process. In this set-up the stripes were moved through a pair of rolls. If one looks closer the deformation process is not homogeneous. When the material is just between the rolls the deformation is equally distributed in this section of the strip. After the complete rolling process the surface is more deformed than the mid-region. This quasi homogeneous state of the rolled stripes is sufficient, because the most important results are the preferable direction,

which is caused by the strong deformation. Also the inhomogeneous deformation is localized only at the surface.

To calculate the deformation one can use the relation in 3.2

$$\varphi_x = \int_{x_0}^{x_1} \frac{1}{x} dx = \ln(\frac{x_1}{x_0}) \tag{3.2}$$

and with help from equation 3.1 we arrive at

$$\varphi_x = \ln(\frac{x_1 - x_0}{x_0} + \frac{x_0}{x_0}) = \ln(\varepsilon_x + 1) \tag{3.3}$$

x_0 . . . . . . starting thickness

x_1 . . . . . . thickness after deformation

ε_x . . . . . . deformation of the tensile test

φ_x . . . . . deformation of rolling (in respect to tensile test)

This correlates the deformation degree φ_x and the tensile strain ε_x after transformation as described by the equation 3.4

$$x_1 = x_0 \cdot \exp(-\varphi_x) \tag{3.4}$$

and therefore the starting thickness x_1 to the thickness as obtained after the rolling process x_0 [26].

With this rolling machine it is not possible to produce the desired thickness just by one experimental step. After each rolling step the thickness was measured with a micrometer screw and in table 3.4 are the real parameters of the by rolling deformed stripes given.

3.4.1 Crystal Structure

As previously mentioned the material used for this thesis is a non-oriented electrical steel (Fe3%Si, see 1). The grain orientation can improve the soft magnetic properties (coercivity, permeability), but the saturation magnetisation M_{sat} must always have the same value. After deformation the lattice of the cubic crystal were slightly deformed, but the deformation was not strong enough to change the crystal structure, which also was not intended. There are papers about the relation of the coercive field strength and the size of the grains [10]. Unfortuna-

Sample	ϕ_x	x_0 [mm]	x_1 [mm]	$\sim \varepsilon_x$
4% Rolled	4.6%	0.507	0.484	4.71%
10% Rolled	10.3%	0.507	0.457	10.85%
20% Rolled	20.1%	0.507	0.415	22.26%

Table 3.4: Deformation parameters of the rolled strips

tely the stress applied was not high enough induce a change in grain size to get significant results.

3.5 Punching

The second more industrial manufacturing process for the ring samples was punching. The „AIT Ranshofen" has a 100 kN punching machine, with which the samples were produced. Dr. Dieter Horwatitsch from the EDT department designed the punching tool and also produced the samples.

 In this case the deformation induced in the material is very severe and inhomogeneous and also has an effect on the magnetic properties. Most manufactures of electrical steel roll their sheets multiple times to achieve the necessary thickness. Then the long stripe is cut and leaves at least the cutting edge deformed. As can be seen in figure 3.6. The cutting process causes a rather inhomogeneous stress situation. This interference between different punching regions gets bigger when the sheet is getting smaller. For manufacturers it is very important to know when the material losses its good soft magnetic properties. With more punches the tool is getting more worn out and therefore the cutting affects the structure increasingly. For this reason the cutting parameters were changed for each sample to simulate different conditions of the tool. The parameters varied were:

- force
- punching speed
- clearance
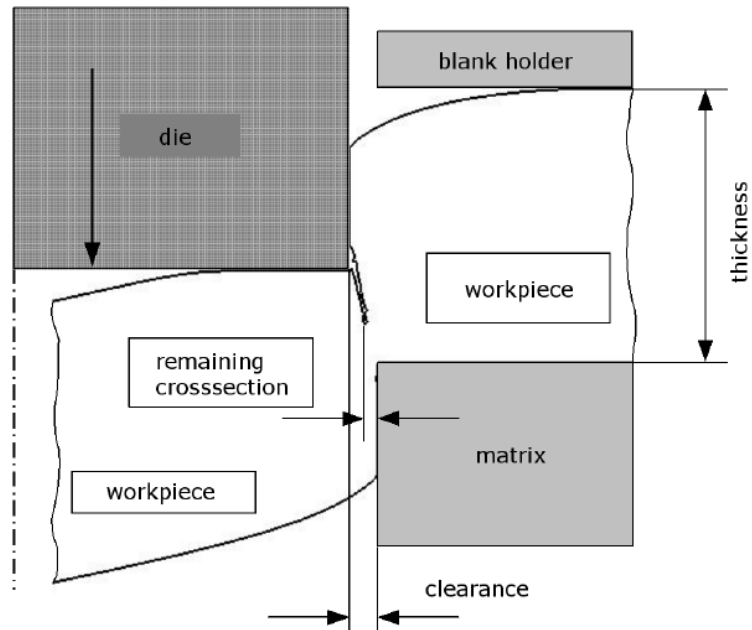
Figure 3.6: Cutting process [37]

With this conditions the following samples with the parameters given in table 3.5 were produced.

		Clearance		
		0.05 mm	**0.035 mm**	**0.1 mm**
Speed	**5 mm/s**	P0.05/5-H	P0.035/5-H	P0.1/5-H
	15 mm/s	P0.05/15-H	P0.035/15-H	P0.1/15-H
	25 mm/s	P0.05/25-H	P0.035/25-H	P0.1/25-H

Table 3.5: Matrix and names of the parameters used for the punched samples

3.5.1 FEM Analysis

Simon Ertl advanced the theory of Jiles-Atherton in his diploma thesis to include localized stress. He simulated the punching process with Finite Element Method (FEM) and wrote a program to solve the Jiles-Atherton Hamiltonian with the

added stress potential numerically. With the experimental data this theory may be confirmed and if necessary improved.

The Jiles-Atherton model and the concept of the stress potential is well explained in Simon Ertl's thesis. In the following is the FEM solution for a punching process shown.
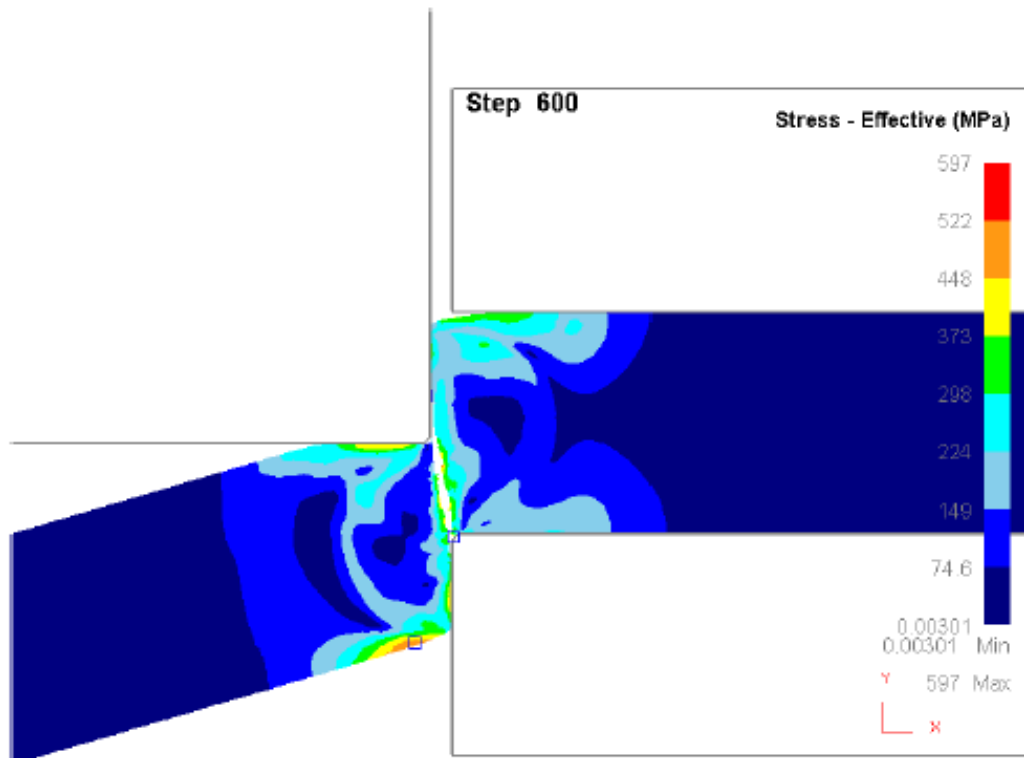
Figure 3.7: Residual stress distribution of the cut workpiece [9, p.33]

As it can be seen the stress is high at the cutting edge and becomes smaller towards the inside. Classical approaches like in section 2 can not be applied and therefore a micromagnetic ansatz must be found, like Jiles and Atherton did.

4 Sample Preparation

In this section the material for the samples and the preparation of the toroidal, especially ring shaped, samples will be described. For electrical and magnetic applications there are a lot of different steel types in use. The composition of such materials is a function between the magnetic losses and the production price.

4.1 Electrical Steel

The material in this thesis is a M400-50A electrical steel, which is in common use for electrical appliances. The shorthand symbol 50A stands for the thickness of the steel. There were two other types of steel available for this thesis, M330-50A and M400-35A, but the M400-50A steel is the most common of them and therefore gave the most representative results for technical use.

The composition and the manufacturing method differs from company to company and is usually kept a secret. Most properties succumb a certain norm which classifies this material as a Fe3%Si. The silicon portion is about 3% ($\pm 0.1\%$). The main reason to contaminate the iron with silicon is to improve the durability. The net induction would be higher for pure iron, but it is to brittle for technical usage. The silicon increases the electrical resistivity and therefore decreases the induced eddy currents as shown in 2.4. In the table below are the properties of the manufacturer which characterizes the material.

Material	Core Loss [W/kg] at		Magnetic Polarization J [T] at			Density [kg/m^3]
	1T	1.5T	2500 A/m	5000 A/m	10000 A/m	
M400-50A	1.7	4.0	1.53	1.63	1.73	7700
M400-35A	1.7	4.0	1.55	1.66	1.76	7750
M330-50A	1.5	3.5	1.50	1.60	1.70	7600

Table 4.1: Magnetic properties of the electrical steel sheets [8]

4.2 Ring Core

The sample geometry defines the field behaviour of the response field. It also defines the parameter used to calculate the magnetic flux density and the magnetic field strength. Especially the mean field length is a complicated value to calculate. For toroidal shaped samples it can be approximated as shown in equation 2.6 which is only valid if the gap between outer and inner diameter is small (<10mm).

In order not to interfere with the degree of deformation of the sample, the rings were cut out of the blank sheet with a laser cutting method. Therefore the deformation caused by the cutting is only localized in a small area around the edges. The influence of the cutting process can so be neglected. The results are 0.5mm thick rings. Every ring had to be cleaned. To guarantee that there is no contamination on the single rings, they were placed in a acetone bath. After 6-8h they could be taken out and swiped with a soft cloth.

All the rings, which are used to made a sample, also had to be weighed and labelled. With this information the iron fill factor can be calculated more accurate, due to the fact that the mass can be determined more accurate than the geometry parameters with a calliper or laser measurement device.

One ring alone doesn't give representative results for a hysteresis loop. To manufacture one sample three rings are glued together to get a high enough magnetic area. The glue was a „Z70" instant glue from „HBM", which is also used for the strain gauges. The only requirement on the glue is that the layer must be very thin to get a reasonable iron fill factor.
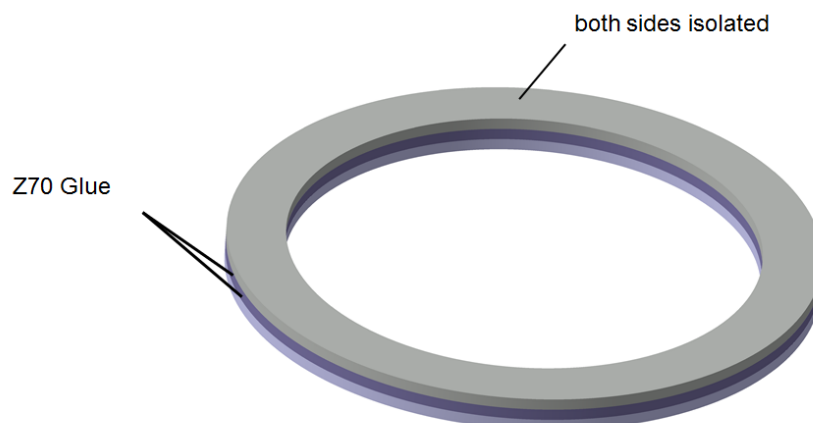
Figure 4.1: A cleaned and glued sample of three M400-50A rings

The layers of a sample must be eccentric, so that the pre factors to calculate the field and the induction describe a real ring sample. To accomplish this two glued sides were weighted with 5kg metal block and aligned horizontally.

A full table with all the dimension, weights and other properties for the individual rings are listed as well as the finished samples are in appendix C listed.

4.3 Winding

In order to generate and detect a field two kinds of coils must be wound around the ring core. This is the most important part of the preparation process. In the field of magnetism, it is convention to denote the field generating coil as primary and the coil which detects the induction field as secondary (pick-up). The following list gives the order in which the two coils are wound most effective:

- Secondary Winding: Has to be near the core (pick-up)
- Primary Winding: Over the secondary winding, can consist of several layers (field coil)
- Both windings have to be wound homogeneously around the circumference

This configuration come from experiments on ring shaped Fe-Si samples. If the secondary winding is over the primary winding the induction field is lower due to stray fields and the air gap between the core material and the winding. The induced voltage is therefore reduced. Similar results were obtained with a inhomogeneous winding[25]. The influence of the air gap between the winding and the core also can not be neglected. An air gap is in first order approximation like an air core and therefore is added to the induction.

This is the cause of the paramagnetic property of air ($\mu \simeq 1$). This effect is almost undetectable if the air area is ¡10% of the magnetic area. Otherwise there is a distinctive linear signal overlapping the induction according to the dependence of magnetic field and flux density for paramagnetic materials [12]

$$B = \mu \cdot H \qquad \text{with } \mu = 1. \tag{4.1}$$

The above mentioned effects must be especially taken account when there are strain gauges on the core, because they add to the height of the sample.
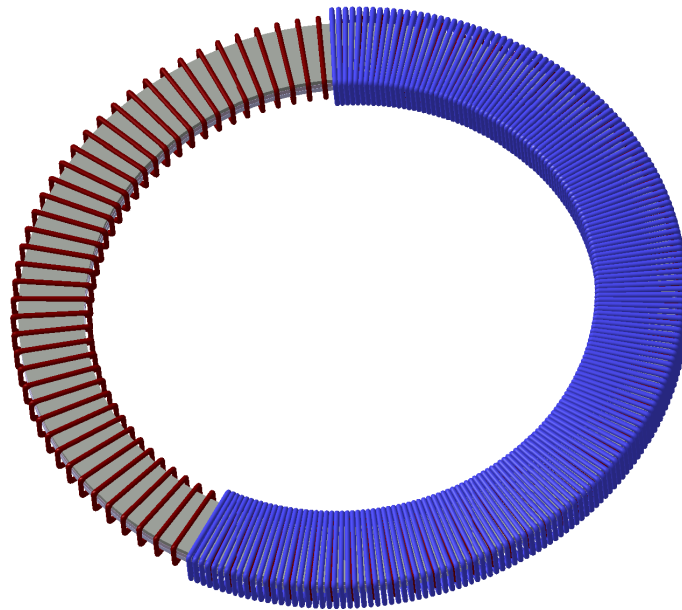
Figure 4.2: Sample for hysteresis measurement with a secondary (red) and primary winding (blue)

4.3.1 Strain Gauge

To detect magnetostriction sensitive sensors must be used. There are three main methods to detect it:

Laser measure the elongation with laser optics (most accurate)

Interferometry with a coherent light source the material is irradiated and when elongation appears interference is detected

Strain Gauge the elongation of the strain gauge results in a change in the electric resistance, this variation can be measured

In this work strain gauges were used, because of the measurement setup described in 5 allows simultaneously measuring of the magnetic fields and the magnetostriction. Also the material is covered with the windings and therefore no optical measurements can be taken on the surface. The strain gauges were glued on the surface of the ringcore. In order to calculate the saturation magnetostriction λ_{sat} two separate measurements were needed: longitudinal and transverse.

In table 4.2 the properties of the strain gauges are listed. Each samples needs three strain gauges: one longitudinal and transversal to the field and a „dummy strain gauge". The „dummy strain gauge" sets the neutral potential for the measurement. With the bridge voltage and the dummy voltage only the voltage
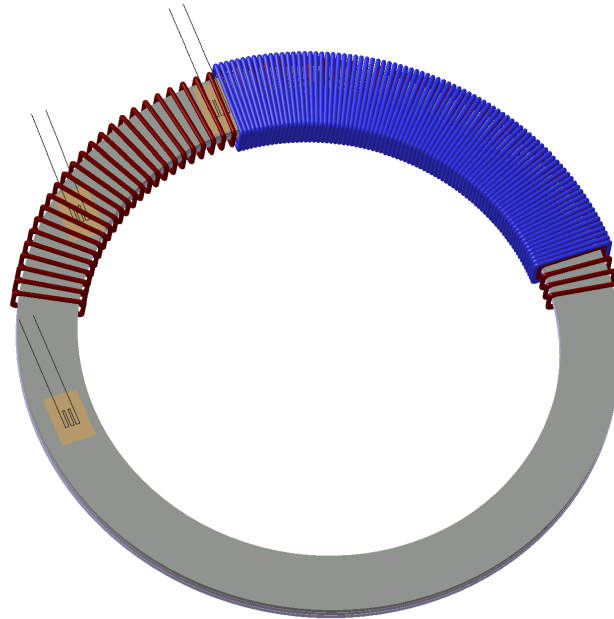
Figure 4.3: Sample for magnetostriction (three strain gauges) and hysteresis measurement (red and blue winding)

difference while the strain gauge changes its resistivity due to elongation is measured. The conversion from the signal to the value of magnetostriction is shown in 2.3.

Property	Value
Type	Ly11-1.5/350
Resistance	$350\,\Omega\ \pm 0.35\%$
k-Faktor	$1.92\ 1.5\%$
α	$10.8\ 10^{-6}/K$

Table 4.2: Properties of the strain gauges used for the magnetostriction measurement [7]

The heating of the samples, even at 0.5 Hz, can be neglected, due to the low heating induction in iron silicon. When the heating still distort the signal it can be corrected with a linear function.

4.3.2 Anisotropy

Due to the different deformation of the steel the ring shaped samples got a texture in a certain direction (see 3). For this reason it was also tried to measure this texture with different settings of winding. The experimental set up is shown in figure 4.4. The position of the anisotropy coil is in longitudinal and transverse to the deformation. It is also important that this coils are small enough to detect the localized flux per time but there must be enough windings to ensure a good signal. To accomplish this, a copper cable with a diameter of 0.1 mm was used. Also the winding is on top of both primary and secondary winding. The measured flux now also has the portion of the much bigger airgap between material and measurement winding. Therefore the measured hysteresis can not be reliable compared with hysteresis from the secondary winding.
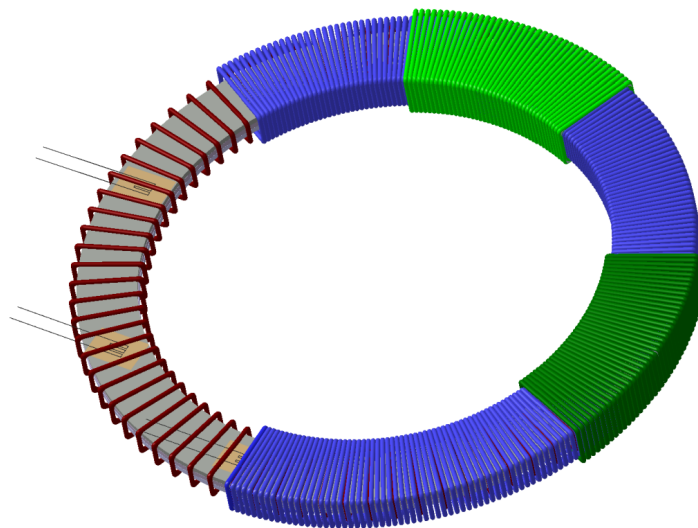
Figure 4.4: Sample with both Strain gauges and windings for anisotropy measurement, as well as a setup for hysteresis

5 Measurement System

To measure hysteresis and magnetostriction a particular system is needed to generate fields and to measure the magnetic response from the material. A simple realization could be a simple function generator (plus a current amplifier) generating an alternating field and a two channel oscilloscope to measure the field- and the induction signals. Peter Oser constructed in his diploma thesis [29] a full automated hysteresisgraph for ring shaped samples and Stefan Hartl improved this setup to enhance the accuracy and decreased the noise which can corrupt the signals [13]. The set-up is displayed in figure 5.1. In this project Hartl also wrote an platform independent Labview program to measure and analyse all kind of signals especially for the application of hysteresis and magnetostriction measurement.
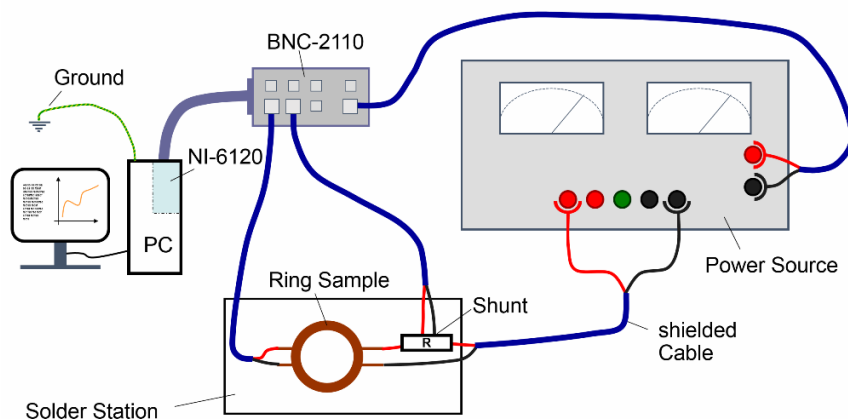
Figure 5.1: The set-up of the hysteresisgraph

5.1 Power Source

The power supply in use is a „Kepco BOP 100-4M“ with 400W. The amplifier is used as a current source and gets the input signal from the digital output of the measurement card over a BNC-box. It also can be used as a voltage source [16]. In figure 5.2b are two serial connected KEPCO amplifiers. This setup can be used to boost the output current (voltage). In this case instead of the single 4A output, a signal up to 8A can be generated. Then the ring shaped sample can

have less winding on the primary side. This reduces the inductance and for this matter the reactive power.
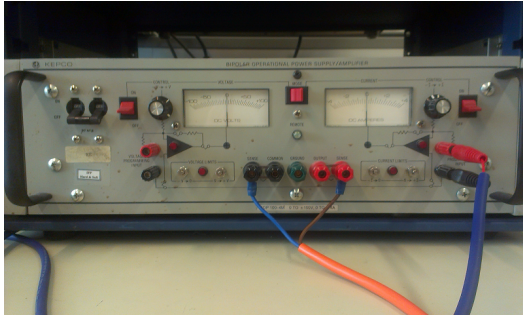
(a) The Kepco BOP 100-4M amplifier connected as current source
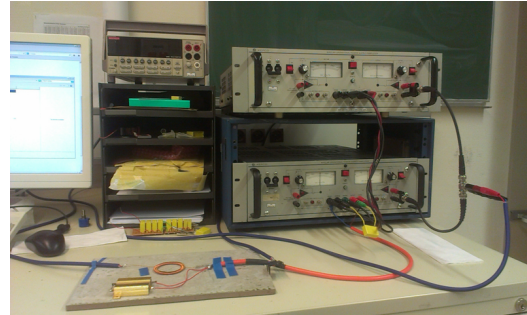
(b) Two seriel connected amplifiers

Figure 5.2: Different connection settings of the amplifier

For the input signal any function generator can be used. The power source only amplifies the incoming signal. Standard signals like sinus, triangle and sawtooth can be generated without any difficulties. In this work the signals were generated via the measurement software and the output of the measurement card. With the software it is also possible to produce a custom signal of any shape and complexity.

Another important aspect is the noise of the power source. For a reliable measurement it is important to differentiate between the signal and the noise, especially when the signal is very small. In figure 5.3 is the noise behaviour of the hysteresis-graph with running power source shown. The signals amplitudes of the induction for $f > 5Hz$ are sufficient, so the noise is not relevant. For lower frequencies or especially for the magnetostriction measurement the signal is generally very small, so it is important to identify the signal from the noise. If the noise level is too high, there is the possibility to put the sample into a μ-metal box with reduces the noise factor additional $\sim 2 - 5\%$.

5.1.1 Measurement

The signal U(t) producing H(t) is generated in the measurement card, sent to the power source and converted into I(t). When the inductance of the primary coil of the ring sample is too high the power amplifier can not generate the desired signal I(t) because then, the necessary voltage becomes due to $U_i = L \cdot dI/dt$ too large. In this case passive elements (resistors, capacitors) can be used to change
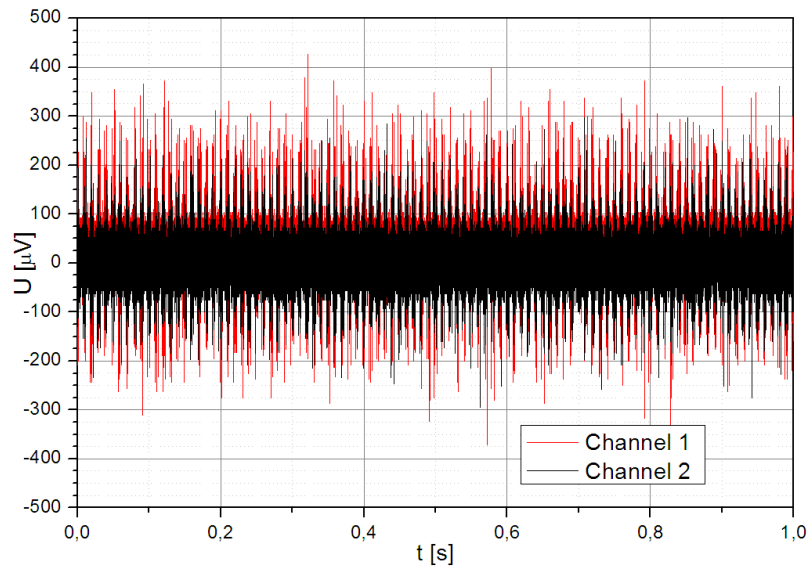
Figure 5.3: Noise behaviour of the hysteresisgraph with running power source

the electrical impedance and to avoid oscillations or compensate the effects of the frequency-dependent reactance. For this purpose a resistor has to be installed in series to the primary coil. This additional resistor consumes electrical power. In order to produce the same current, the applied voltage has to be increased. When the overall impedance becomes too high, the amplifier runs in its voltage limit and the signal will be cutted or distorted.

In order to smooth the output signal or avoid oscillations, capacitors must be installed parallel to the output signal. It's also possible to filter beats and to reduce the reactance. This technique has to be used with care, because with a too high capacitance in the system the generated signal may also be smoothed or changed in shape, e.g. a triangle signal does not have a sharp peak any more.

For all measurements in section 6 the information concerning the passive elements (capacitors, resistors) is included. This is important to describe the exact conditions in order to allow reproducible measurements.

5.2 Measuring Amplifier for Strain Gauges

To measure the magnetostriction a commercial AC bridge (Hottinger KWS 3085A - see figure 5.4) for strain gauges is used, which is necessary in order to measure small signals. It is basically a lock-in amplifier with fixed frequency which can be adjusted to the resistance of the strain gauge. Important for dynamic measure-

ments is the carrier frequency of the lock-in, which is for the KWS 3085A 50kHz. This unusual high carrier frequency was chosen in order to allow dynamic magnetostriction measurements up to high frequencies (up to 1000 Hz). Through the strain gauge (and parallel through its dummy gauge) flows a constant bridge current. When the resistance of the strain gauge changes, due to the elongation of the sample, a differential voltage is measured. All measurements are performed at room temperature, but while measuring at different frequencies (frequency range from 0.25Hz-1000Hz) the sample heats due the current in the primary coil. With one amplifier only one direction (longitudinal or transversal to the applied field) of the magnetostriction can be measured. Therefore two different magnetostriction measurements have to be performed. It would be possible to measure both directions at once, because the measurement card has four input channels, but for this purpose a second strain gauge bridge would be needed.
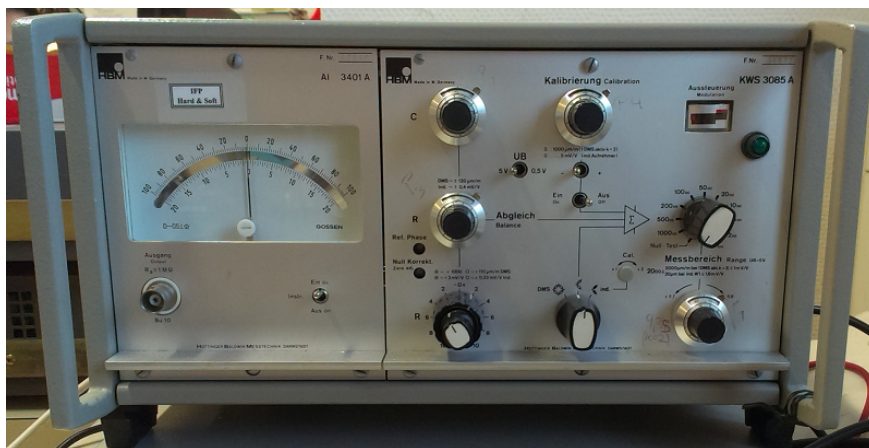
Figure 5.4: The amplifier KWS 3085A from HBM used for the strain gauges

5.3 Other Equipment

In order to process the signal, a measurement card which can detect and digitalize voltages, is needed. This card shall have a high resolution (12 - 16 Bit ADC) as well as a high conversion rate in order to allow also measurements a high frequencies. For this purpose the data acquisition card from National Instruments (DAQ 6120) was used. This data acquisition card can be handled by the „Labview" measuring software and provides a reliable and easy to handle bridge between soft- and hardware. The measuring card has a resolution of 800kS/s and

two A/D-converters. With the converters two signals can be handled almost in real time. In the following is a list of the data acquisition equipment given:

- NI DAQ 6120 [27]
- NI BNC 2110 [4]

5.4 Measurement Software

The measurement and calculating process is controlled by a program written in Labview. The development software Labview can perfectly be used with all equipment from National Instruments. Therefore the data acquisition is programmed with the library functions from Labview. The program is divided in modules in order to use different parts from the program for other applications (e.g. the oscilloscope). The focus on the program is to simplify the measurement process.

 To get physically meaningful values from the acquired signals (voltage) different mathematical steps are necessary. The calculated fields must also be corrected. Within the A/D-converter a small voltage can occur, which causes a drift on the signal. This drift shifts the measured signal for the flux density by a linear factor. With two (ore more) points in one period of the slope and the offset of the drift can be calculated and corrected. The measurement card can also be on a zero different potential, so the signal may get an offset value. Labview does not have the capability to perform complicated algorithms. To overcome this, a special Java program, called „MAGPACK“, has been written. The advantage of this process using Java is that there are good and verified mathematical libraries for the major programming languages available. This correction software (offset, voltage drift, temperature drift) is implemented in Labview and can be easily accessed directly in the hysteresisgraph using a command line. This program has other built in functions which can be useful not only for measuring magnetic properties, but for general calculation also, which are listed below:

 Main usage for magnetic measurements
- Generating signals $U(t) \rightarrow H(t)$
- Measure at least three different channels with maximal resolution (points acquired)
- Correction of the raw signals (drift and offset correction)
- Calculating the necessary magnetic fields (see 2.1)

- Determination of the coercive field H_c
- Calculating the losses (by integration)
- Calculating both directions of the magnetostriction and calculation of the saturation magnetostriction (see 2.3)
- Calculating the permeability $\mu(H(t))$

Other functions
- Integrating (up to third degree)
- Derivative of functions
- Interpolating between curves of different lengths

Both programs (Labview and Java) have been tested in different projects and verified with comparative measurements.

6 Measurement Results

The following chapter shows all the measurements taken in this thesis and the resulting model calculations. At firs all the boundary conditions of the experiment were shown to comprehend the values derived. From the losses and the coercivity the residual stress σ_{res} will be correlated to the induced deformation ϵ using the magnetostriction.

6.1 Samples

As described in 3.2 all samples except the „AsCast" material, were heat treated. This samples are labelled with „H" in table 6.1, because all of them are heat-treated at $400\,C°$ and every stripe is listed in 3.1. The additional shorthand symbol „B" stands for a the second sample of the same quality. This was for quality assurance reasons, to ensure the accuracy of the data. Every Ring was measured individually before and after they were glued together to calculate the iron fill factor (dimensions and calculations are in appendix C).

Sample	N1	N2	l_m [m]	A_{Fe} [m^2]	η_{Fe}	$\rho\,[\Omega m \cdot 10^{-8}]$
AsCast	282	144	0.14115	8.46787 E-6	0.90241	45.2
AsCast - B	305	102	0.14115	8.51125 E-6	0.89776	45.2
Reference	329	108	0.14115	8.30640 E-6	0.91688	38.5
Reference - B	341	92	0.14115	8.37440 E-6	0.90322	38.5
ε 0.5%-H	315	93	0.14128	8.14860 E-6	0.93443	48.1
ε 2%-H	319	115	0.14118	8.17600 E-6	0.92984	49.2
ε 2%-H-B	333	89	0.14117	8.20301 E-6	0.90911	49.2
ε 4%-H	338	133	0.14126	8.35954 E-6	0.91055	51.1
φ 4%-H	311	98	0.13009	7.66300 E-6	0.86358	38.9
φ 10%-H	310	89	0.13013	7.03736 E-6	0.87327	56.1
φ 20%-H	315	73	0.13006	6.41390 E-6	0.88760	58.0
φ 20%-H-B	339	98	0.13006	6.56620 E-6	0.91005	58.0

Table 6.1: Description and measurement properties from the homogeneous deformed ring shaped samples and the reference sample

The primary and secondary winding were wound with a 0.35 mm copper cable and every layer is isolated with insulating tape to prevent short circuits between winding and sample. Some samples were produced two times, to validate the values from the first sample. This is a statistical process to ensure the repeatability of the experiment. The samples were picked randomly except for the *„AsCast"* and the *„Reference"* . All measurements could be reproduced with sufficient accuracy of $> 98\%$.

Sample	N1	N2	l_m [m]	A_{Fe} [m^2]	η_{Fe}
P0.05/5-H	333	106	0.14126	8.34442E-6	0.91306
P0.05/15-H	339	75	0.14303	8.46240E-6	0.89164
P0.05/15-H-B	345	80	0.14303	8.39921E-6	0.90443
P0.05/25-H	344	102	0.14136	8.45224E-6	0.90182
P0.035/5-H	334	90	0.14127	8.23077E-6	0.91642
P0.035/5-H-B	339	101	0.14127	8.38066E-6	0.90156
P0.035/15-H	332	107	0.14127	8.37639E-6	0.90070
P0.035/25-H	336	70	0.141478	8.30681E-6	0.90742
P0.075/5-H	340	84	0.141661	8.34483E-6	0.91220
P0.075/15-H	345	73	0.141300	8.40061E-6	0.89355
P0.075/25-H	339	81	0.141916	8.33185E-6	0.90891

Table 6.2: Description and measurement properties from the punched ring shaped samples

It was also necessary to measure the electrical specific resistivity ρ, because any mechanical deformation shall cause a change of the resistivity. As is described in 2.4 the electrical resistivity is an important property for calculating the fitting parameters of the overall losses and the coercivity. The group of Prof. Bauer from the *„Solid State Physics"* department has an experimental equipment, based on the *four-point method*, to measure the electrical resistivity ρ with high accuracy. These measurements were kindly performed by his group.

Table 6.2 lists the winding properties of the samples produced by the punching manufacturing process. It should be noted, that the punched samples have less eccentricity than the laser cut rings and it was also easier to produce a higher

amount of ring shaped samples. This is because the rings are more planar than that after a tensile stressing process - especially the rolled rings. Also on these samples no magnetostriction measurements were performed, because of the inhomogeneous deformation state the results can not be explained applying a stress model.

To ensure a homogeneous distributed magnetic field, the skin depth $\delta(f)$ indicates the penetration of an external ac-field H(t). In table 6.3 are the values for the boundaries of the measurements as well as for the most interesting frequency of 50Hz. Due to the inhomogeneity of the punched samples the resistivity changes throughout the material and the value of the *"Reference"* is used to represent those samples.

Sample	$\delta \,[mm]$ at		
	1Hz	50Hz	1000Hz
AsCast	10.44	1.48	0.33
Reference	13.02	1.84	0.41
$\varepsilon 0.5\% - H$	15.25	2.16	0.48
$\varepsilon 2\% - H$	16.41	2.32	0.52
$\varepsilon 4\% - H$	20.87	2.95	0.66
$\varphi 4\% - H$	13.88	1.90	0.43
$\varphi 10\% - H$	21.54	3.05	0.68
$\varphi 20\% - H$	22.66	3.20	0.72

Table 6.3: Skin depths δ for the boundary frequencies and for 50 Hz

6.2 Hysteresis Measurement

The following figures show the hysteresis of the „AsCast", the reference sample „Reference" and all the deformed sample measured at room temperature. The field amplitude was chosen to be 15000 A/m, because in most data sheets the induction at different applied fields is given as a factor of the material (usually 2500 A/m, 5000 A/m, 10000 A/m, 15000 A/m). The polarization values at

certain fields can directly be compared.

Figure 6.2a displays the hysteresis for the material as it was produced. It shows the typical behaviour of untreated M400-50A steel sheets. This sample was used to compare the original material with the data from the company, to ensure consistency throughout all the measurements. The first hysteresis loops of figure 6.2 is used as reference loops for all deformed samples. This sample was heat treated at 400 °C as described in 3.2 to remove residual stress from the manufacturing process. All deformed samples were heat-treated under same conditions to ensure an equal state for all samples.

6.2.1 Hysteresis loops of the homogeneous deformed samples

The following figures show the hysteresis of the sample *"Reference"* (fig. 6.1) and the homogeneous deformed sample (see fig. 6.2). All measurements were performed under sinusoidal and triangular external field H(t), but only the triangular results are shown. The losses and the coercivity changes under different fields (deviation $\sim 10\%$), but the triangular field is better to analyse, because of the constant slope of the field and therefore is used to interpret the measurements throughout this thesis.
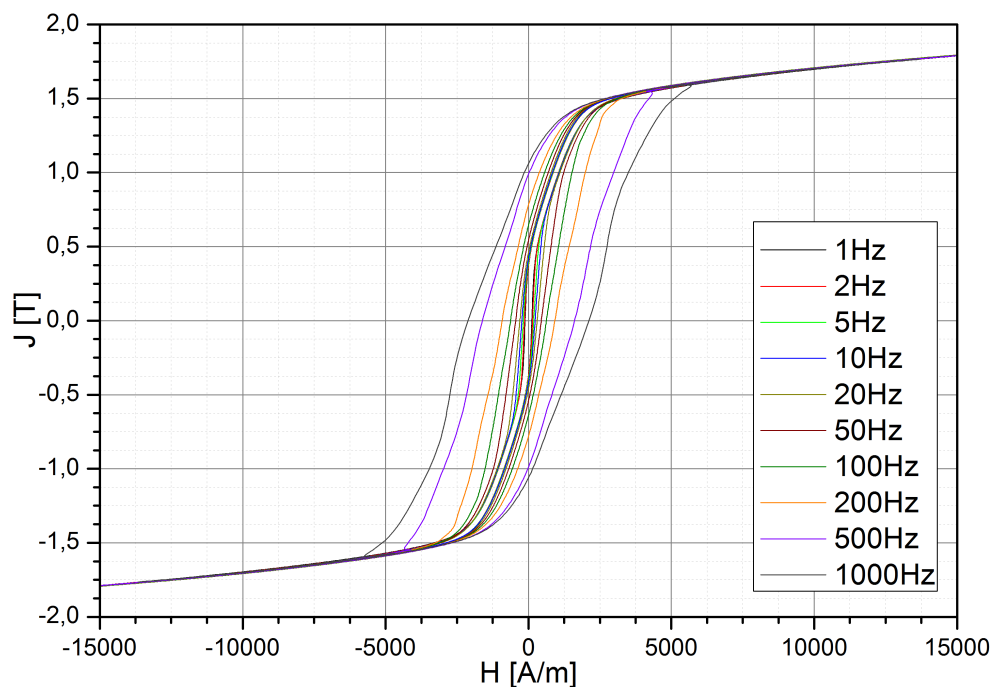
Figure 6.1: "Reference": Hysteresis of the reference over a frequency range of 1-1000Hz

(a) "AsCast"

(b) ε0.5%-H

(c) ε2%-H

(d) ε4%-H

(e) φ4%-H

(f) φ10%-H
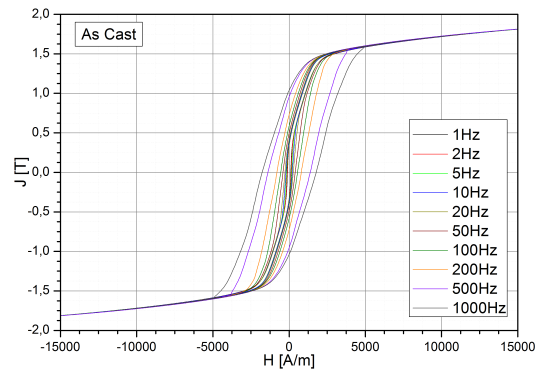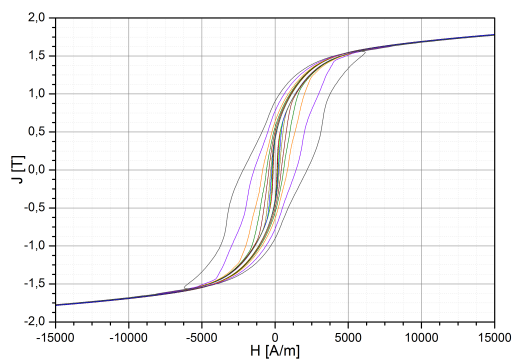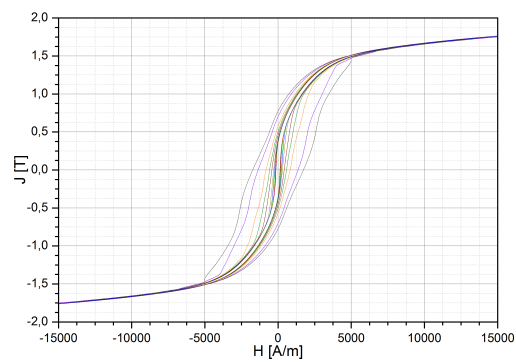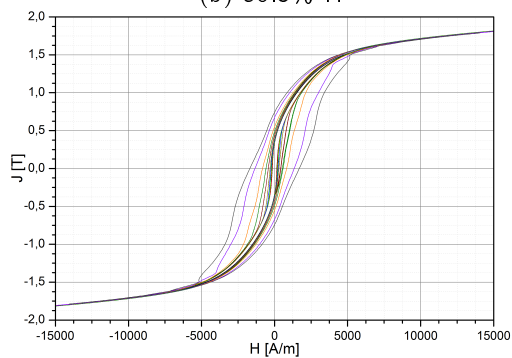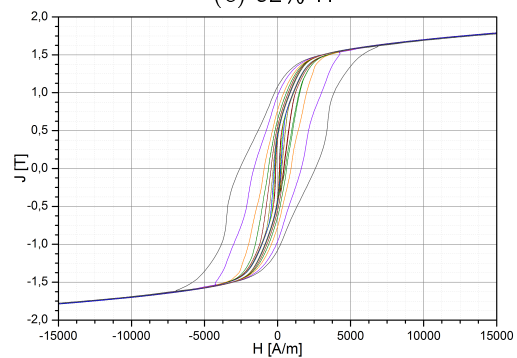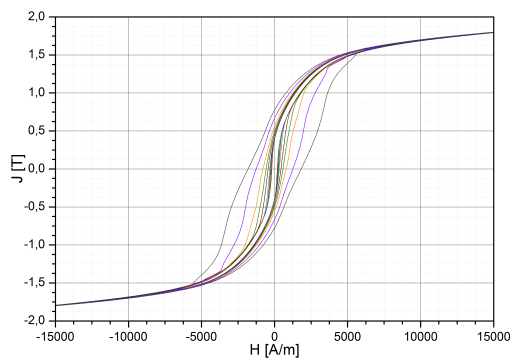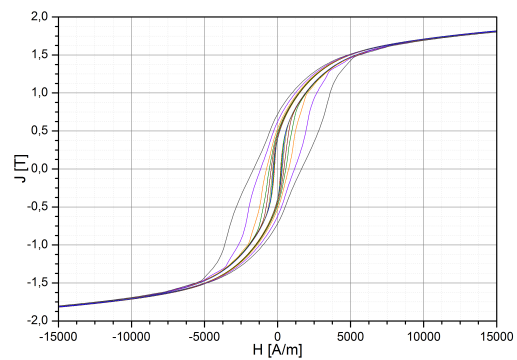
(g) φ20%-H

Figure 6.2: Hysteresis loops of the reference and the homogeneous deformed samples at a frequency range of 1-1000 Hz

6.2.2 Hysteresis measurement of the punched samples

The measurements of the punched samples, which are in an inhomogeneous stress state, were performed under the same conditions as the experiments on the homogeneously stressed ones. The hysteresis loops were measured under triangular and a sinusoidal field, but only the triangular B(H(t)) measurements were used for a further analysis. This is consistent with the argument in 6.2.1. All hysteresis loops were measured at least five times to ensure repeatability of the obtained values.

With the different signal measurements, Dr. Reinhard Wöhrenschimmel further improve the Jiles-Atherton model based on the work of Simon Ertl. The sinusoidal field represents the signal used in the power grid and therefore is from interest for electrical applications.

The general shape of the measured hysteresis loops also show a difference regarding the „Reference". This is consistent with the result obtained for the homogeneous samples. Again a higher field has to be applied to arrive at the reach the same polarization value as the „Reference" sample, which supports the argument. The same argument can be applied, that additionally to the magnetization process, the induced energy from the deformation has to be overcome. It is not easy to distinguish the change of the shapes in fig. 6.3, but in the losses and the coercivity a great difference between the punching parameters can be observed.

      (a) P0.035/5-H   (b) P0.035/15-H
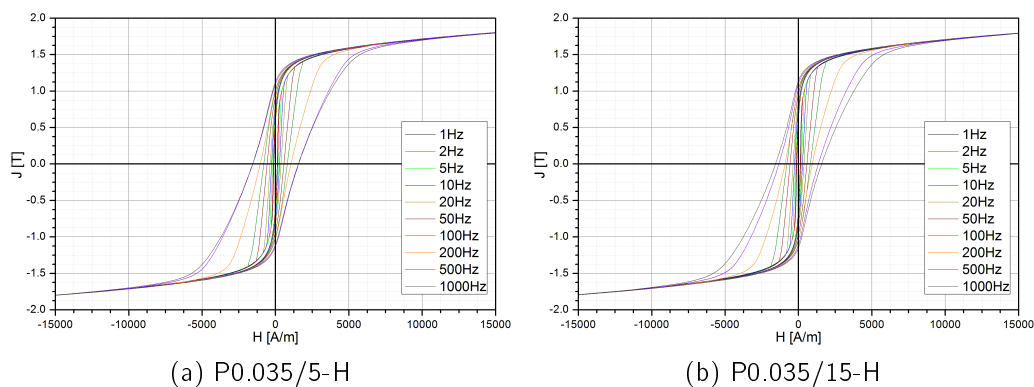
Figure 6.3: Hysteresis loops of the punched samples at a frequency range of 1-1000 Hz

(a) P0.035/25-H

(b) P0.005/5-H

(c) P0.005/15-H

(d) P0.005/25-H

(e) P0.0075/5-H

(f) P0.0075/25-H
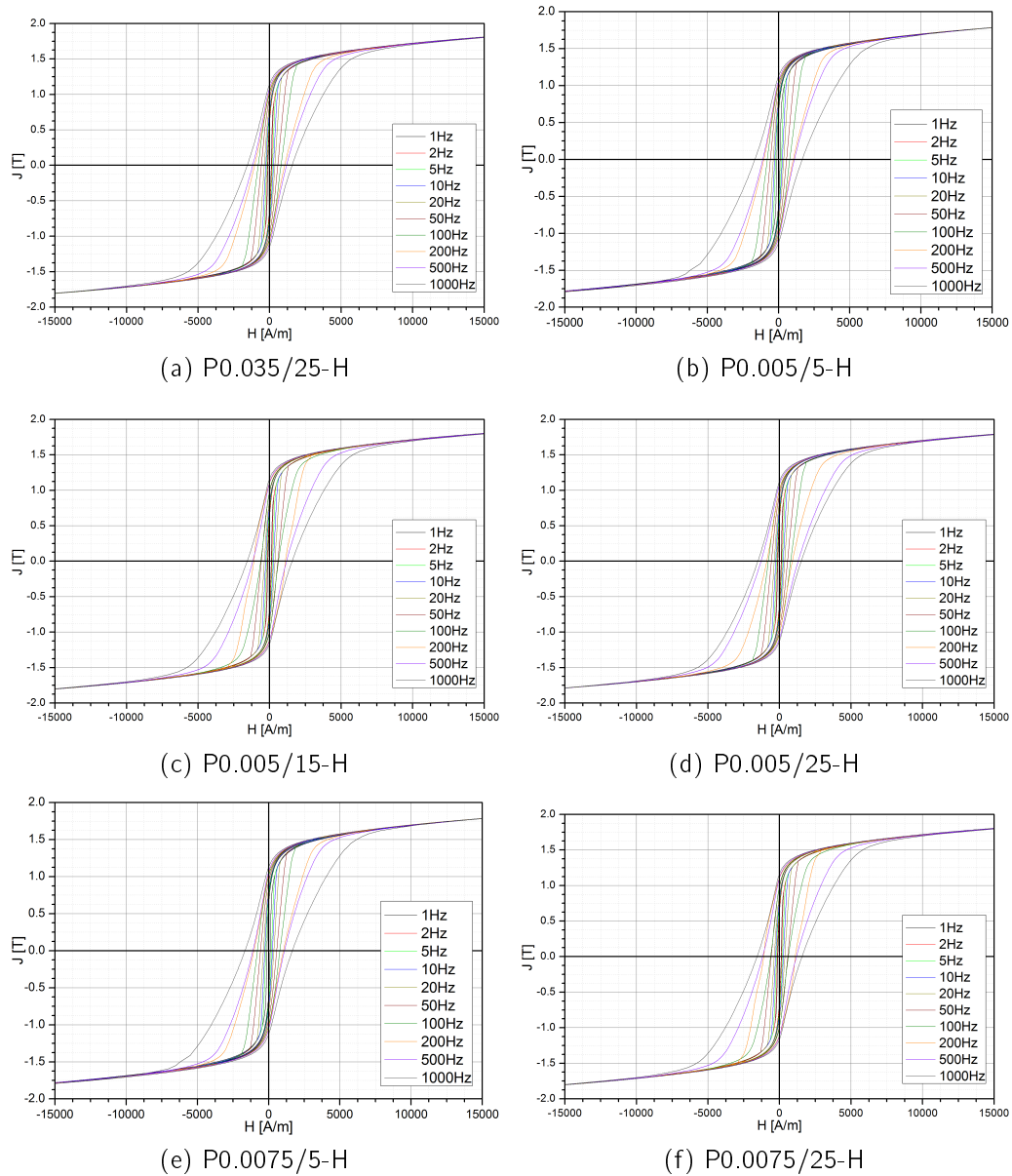
Figure 6.4: Hysteresis loops of the punched samples at a frequency range
of 1-1000 Hz

6.2.3 Approach to Saturation

As it can be see in figure 6.5 all hysteresis loops achieved on the different stressed samples converge to the same value of saturation induction. Every other solution would not be physically understandable and therefore it can be assumed that the measurements were carried out correctly. The maximum field applied was around 25000 A/m and with the law of approach to saturation from 2.2.3 all samples arrive at the saturation polarisation from $J_s = 2.051\,T$ ($\pm 0.0092T$).
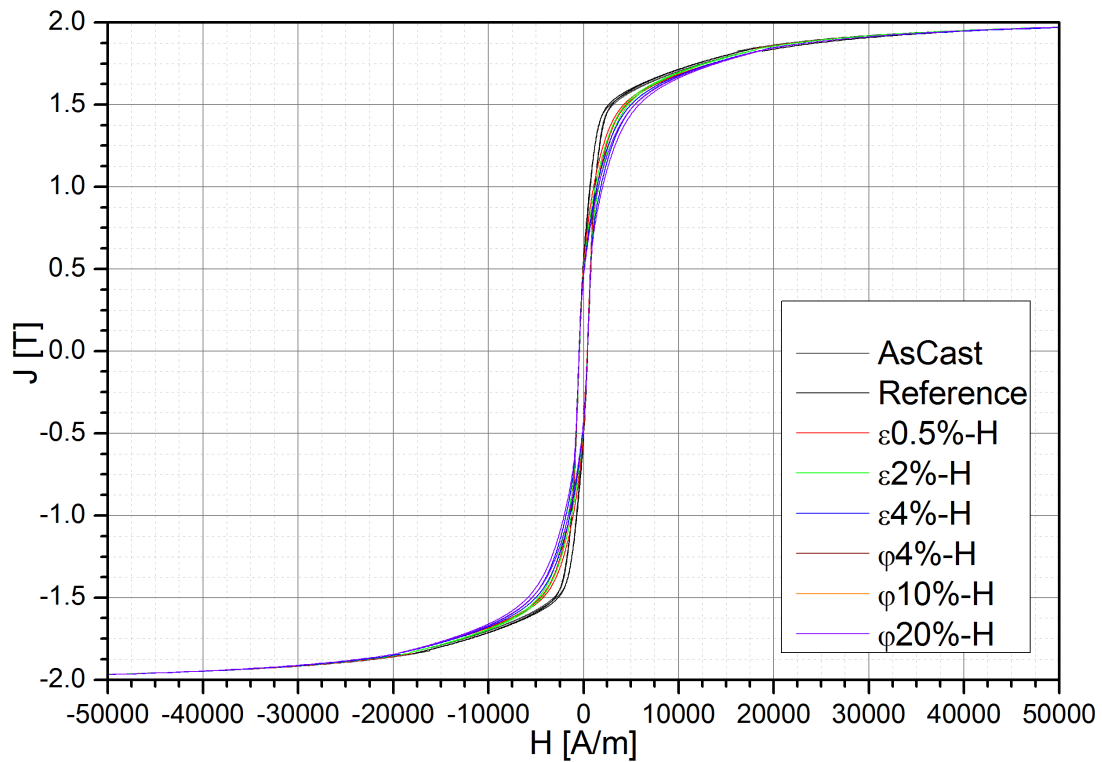
Figure 6.5: Saturation polarization at 50 Hz

In the work of Kronmüller and Seeger it is stated, that the parameters of the law of approach to saturation can also be explained in more detail. Especially the parameter B contains information about the induced stress state and other mechanical properties [22]. The starting field for the fitting function from eq. 2.16 has to be at least $10 \cdot H_c$ ($\approx 2000 - 5000 A/m$) in order to avoid domain effects. To investigate the minimum error of the fitting parameters the starting field was varied with a *minimization algorithm* programmed for this type of function. The results can be viewed in figure 6.6. Due to the very soft magnetic property of the material the hysteresis at low fields H(t) reaches high polarization values J(t). Therefore the hysteresis at high polarizations converges to the same shape of the hysteresis loop. The parameters A and B do not deliver information regarding the deformation, because of their uncorrelated (small) values and high mean errors. Although it is interesting, that the fitted saturation polarization J_s achieves the correct value for all samples. This can be explained, because the terms depending on H(t) vanish at high fields $H(t) \rightarrow \infty$.
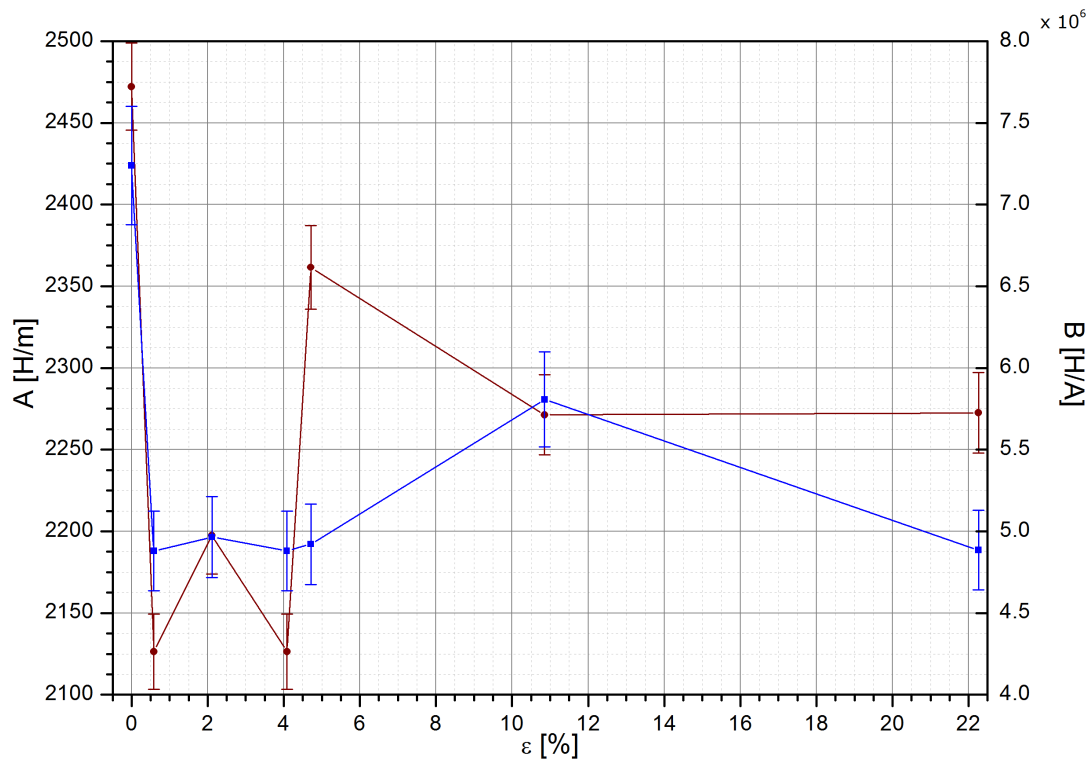
Figure 6.6: Parameters A(red) and B (blue) of the law of approach

6.2.4 Permeability

To calculate the permeability, minor loops, a demagnetized state at the beginning of the measurements is important. There are different ways to demagnetize a sample:

- heating over the curie temperature T_C - thermal demagnetization

- mechanical vibrations

- alternating and decreasing external field $H(t)$

The Curie temperature of electrical steel usually is about $700 - 1100\,K$ and therefore impractical for continuous measuring over a frequency range, the same applies to the shocking technique. For this reason a demagnetizing algorithm was implemented in the measurement software according to Schnabl [34]

The Curie temperature of electrical steel usually is about 1346K and therefore the thermal demagnetization is practically impossible for continuous measurements over a frequency range. For this reason a demagnetizing algorithm was implemented in the measurement software according to Schnabl [34].

$$I(t) = A \cdot AF(t) \cdot \exp^{-\omega t} = I_0 \cdot \sin(\omega t) \cdot \exp^{-\omega t} \tag{6.1}$$

where AF(t) stands for any alternating function and I_0 is the amplitude of the applied current. In this thesis AF(t) is consistently an exponentially decreasing sine function. There were tests with other functions (triangle, rectangular), but there was no difference measurable in the demagnetized state. In figure 6.7 are the virgin curves of the homogeneous deformed samples. Additionally applying the formulas in 2.2 the relative permeabilities μ_r were calculated.
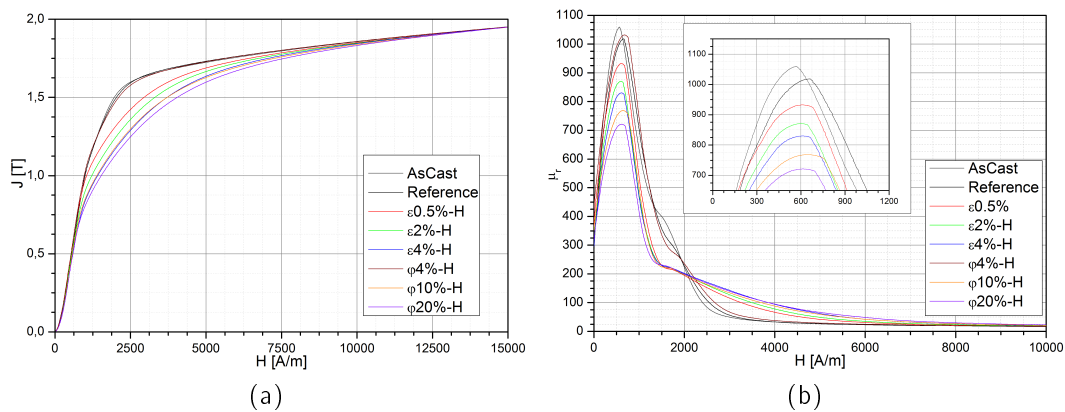
Figure 6.7: (a) Magnetization curve from which the relative permeability μ_r was calculated and relative permeability curve of the homogeneous deformed samples (b)

The permeability plotted over the applied field $H(t)$ has the same characteristics as the magnetostriction, but for the properties, which defines the material, only the region of the virgin curve is required. As seen in figure 6.7b the curve reaches its maximum permeability at the coercive field strength and approaches $\mu_r \rightarrow 1$ at very high fields.

Sample	μ_r	σ_{μ_0}	at H [A/m]
AsCast	1050	1.41	0.3898
Reference	1005	1.35	0.7609
$\varepsilon 0.5\% - H$	942	0.92	0.5345
$\varepsilon 2\% - H$	867	0.88	0.78998
$\varepsilon 4\% - H$	825	0.71	0.8537
$\varphi 4\% - H$	1045	1.25	0.8161
$\varphi 10\% - H$	781	0.80	0.6837
$\varphi 20\% - H$	717	1.33	0.9153

Table 6.4: Relative permeability μ_r values at 50 Hz

6.2.5 Comparison of the deformed samples

This section compares the hysteresis of all samples at a certain frequency. The stress induced change of the hysteresis is directly visible. Figure 6.8 shows the hysteresis at quasi static conditions (f = 1Hz). Evidently the form of the hysteresis changes drastically due to the deformation of the material.
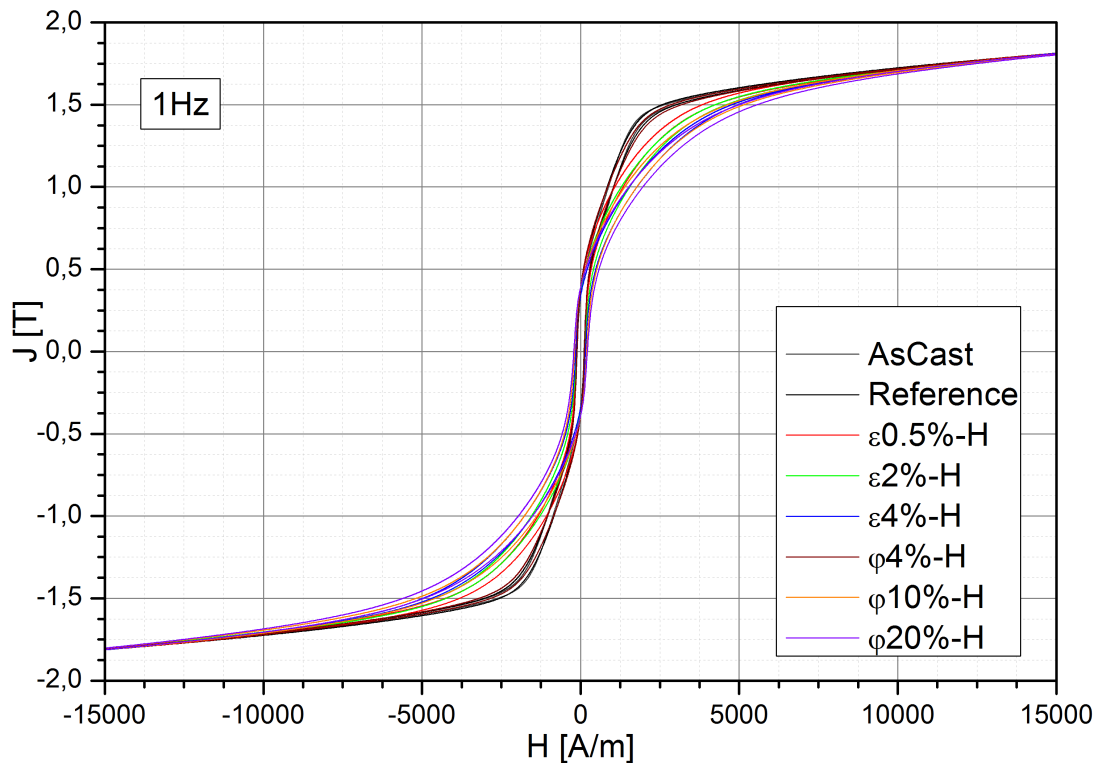
Figure 6.8: Hysteresis of the deformed samples at 1Hz

Specifically the slope flattens and the relative permeability μ_r decreases with increasing stress (see 6.2.4). It can be seen that even at small stresses (*ε0.5%-H*) the J(H) curve differs from that of the *"Reference"*. The change in the hysteresis approaches saturation for the *φ20%-H* sample due to the high deformation.

The measurement at 50 Hz (fig. 6.9) corresponds to the technical common frequency. The change with stress of the observed hysteresis loops show a similar variation as the 1 Hz curves. Due to the frequency dependent losses the hysteresis area is getting greater. This area also scales with the induced stress. This means that the magnetization vector needs more energy to align with the applied field as a direct consequence to the internal stress and the deformation of the crystal lattice. The deformation also changes the magnetic domains and therefore changes the minimum of the total magnetic energy, especially contribution of the exchange and the magnetoelastic energy. The interpretation of the hysteresis is rather difficult, because there are many effects to which influences a loop, however they can not be estimated in a simple manner. The coercivity, the remanence and the saturation values can be achieved from the measurement and are discussed in detail below.
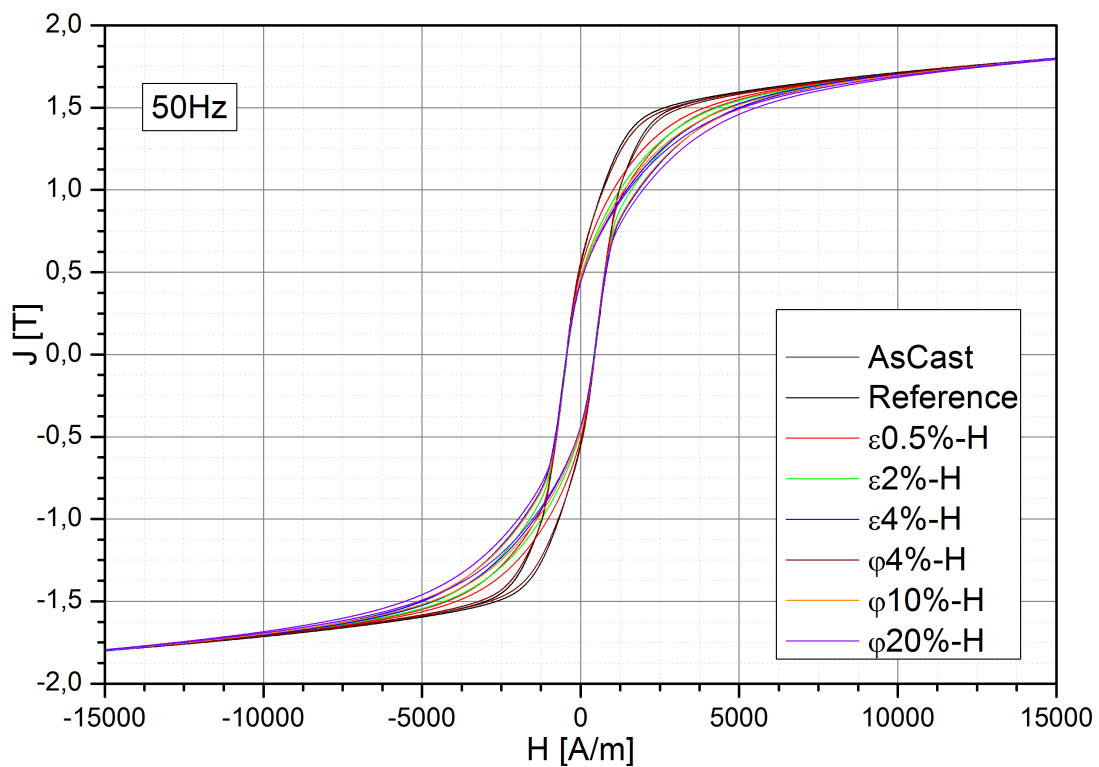
Figure 6.9: Hysteresis of the deformed samples at 50Hz

All other frequency dependent hysteresis loops are shown in figure 6.10. Clearly the hysteresis loops get wider, due to disruptive frequency effects. The shape of these loops can better be understood after investigating the overall losses, as it will be done in 2.4. Another interesting aspect of the low frequency loops is the general shape with an additional inflection point. This originates from the internal stress from the manufacturing process. Even applying a stress relaxation heating process (T =420°*C*, t = 320 min) not all strains can be removed. At higher frequencies the eddy currents dominate the shape of the hysteresis. The sample *φ4%-H* shows almost the same shape of the hysteresis loop as the *"Reference"* material.
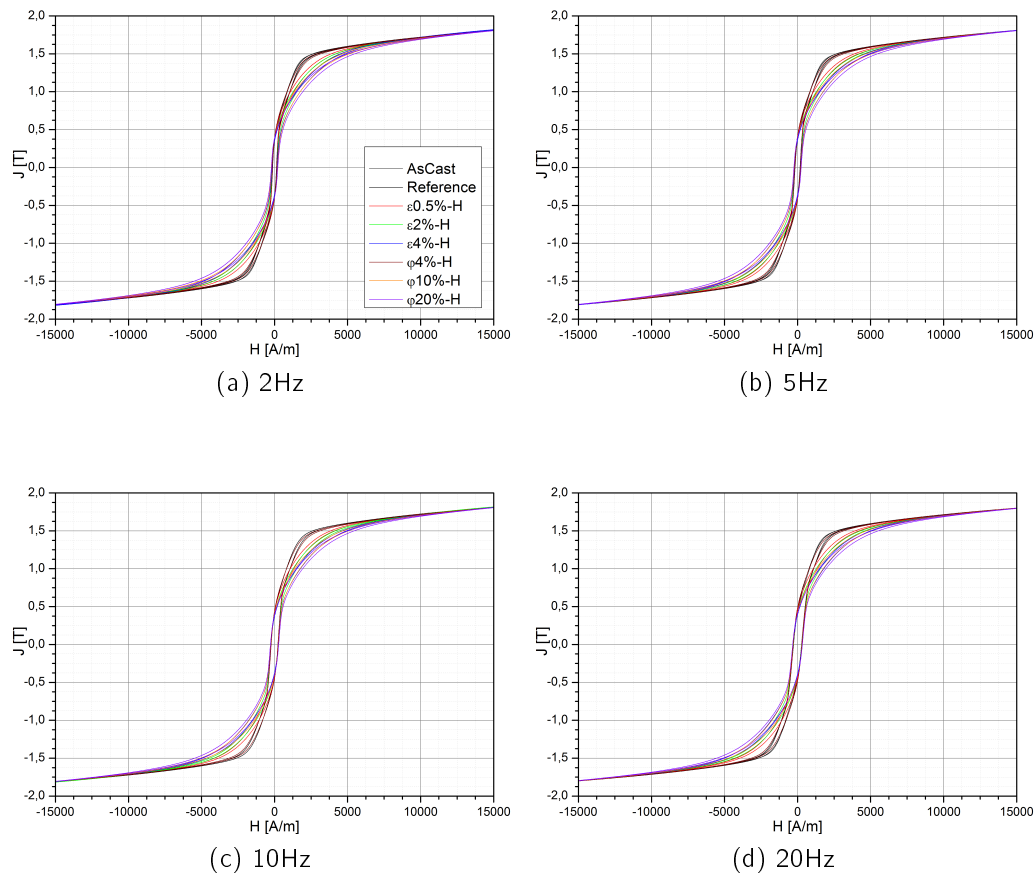
Figure 6.10: Hysteresis loops of the homogeneous deformed samples compared at certain frequencies

(a) 100Hz

(b) 200Hz

(c) 500Hz

(d) 1000Hz
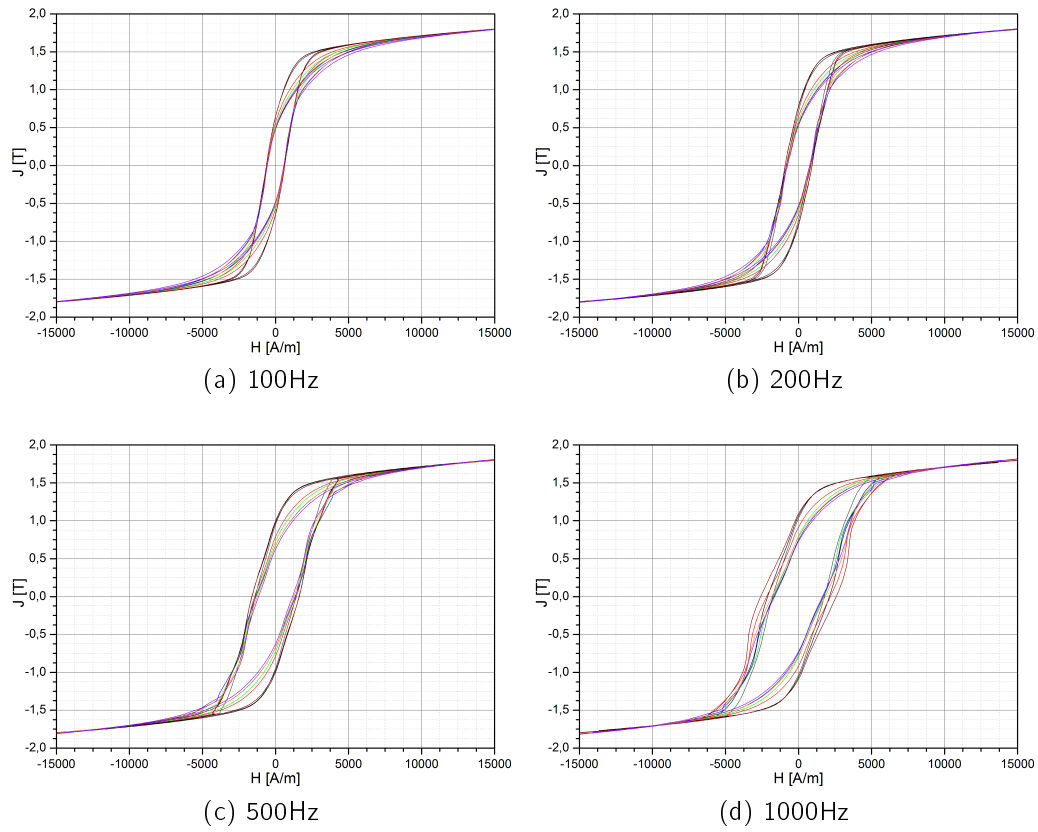
Figure 6.11: Hysteresis loops of the homogeneous deformed samples compared
at certain frequencies

6.2.6 Texture

In order to investigate a local texture by hysteresis measurements a special arrangement of small pick-up coils was chosen (see fig. 6.12).

Sample	N_2	N_L	N_T
AsCast	65.34	41	40
Reference	71.79	45	41
$\varepsilon 2\% - H$	101.60	42	43
$\varepsilon 4\% - H$	118.15	41	40
$\varphi 20\% - H$	181.93	43	41

Table 6.5: Anisotropy properties regarding the secondary
winding. Dimensions in table 6.1

In table 6.5 are the specifications and the samples on which the texture coils were used. For these measurements a triangular field H(t) was applied and in figure 4.4 are the result as obtained on one sample shown.

As seen in the figures above (see fig. 6.2) the shapes of the hysteresis loops are the same but the saturation values are different. These rather big differences can not be explained by the different texture. The main reason of this discrepancy ($> 2\%$) is different magnetic surface used to calculate the magnetic polarization J(t). In the secondary measurement the sample dimensions were taken from five different positions and the average of them were calculated. If the area now differs more than 2% from the averaged surface from table 6.1 the magnetic polarization J(t) also scales with this variation due to equation 2.10.
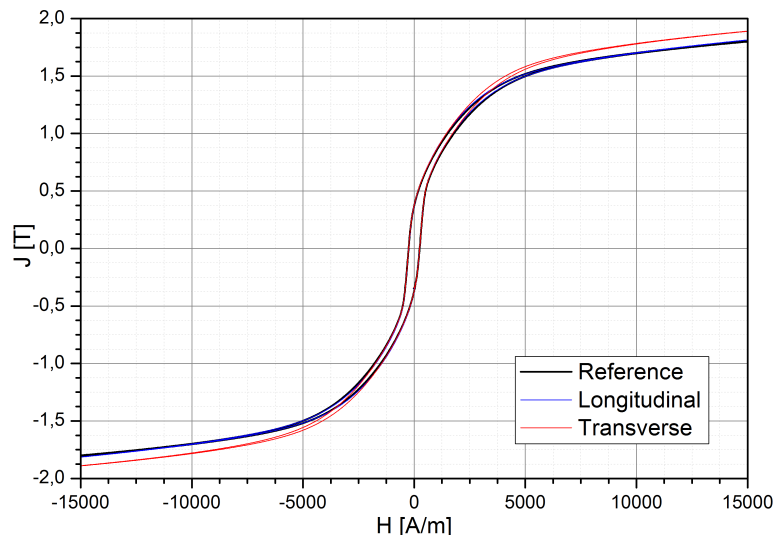
Figure 6.12: Different hysteresis of the *"AsCast"* sample obtained from the anisotropy and the secondary winding at 10 Hz

The other samples where the texture windings were used, showed the same behaviour. Because these measurements came not to any useful new result, the other hysteresis loops are not shown.

6.3 Core Losses

The overall losses are calculated from the area of the hysteresis loops. The integral over one period was calculated numerically and the such achieved values at different frequencies are shown on figure 6.13 and in more detail in 6.14.

For the determination of the losses at low frequency the average over four
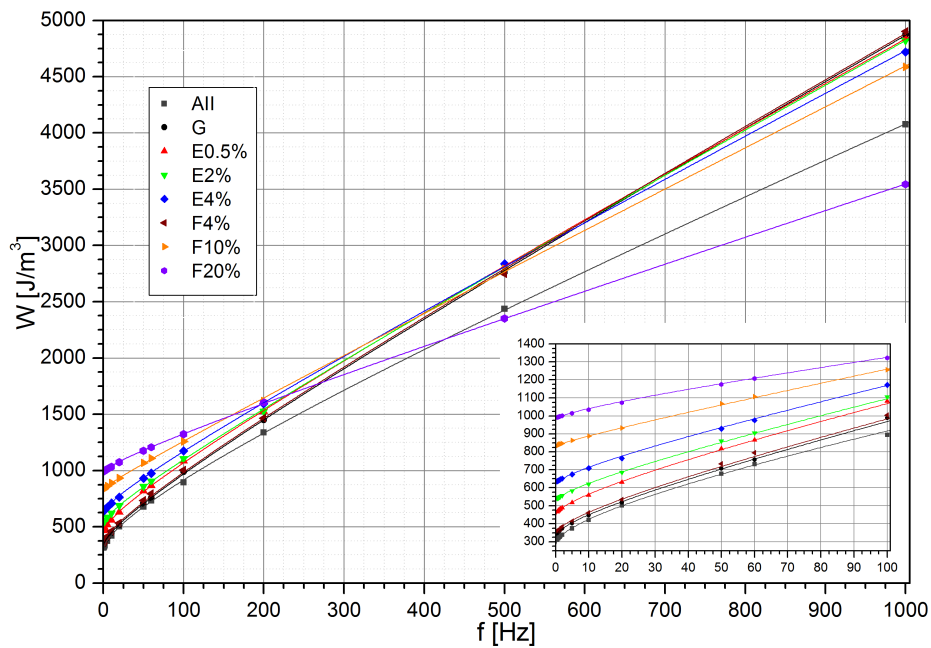
Figure 6.13: Core Loss of all samples over the whole frequency range

hysteresis loops were needed. This ensures enough points to calculate the area under the loop with an acceptable accuracy.
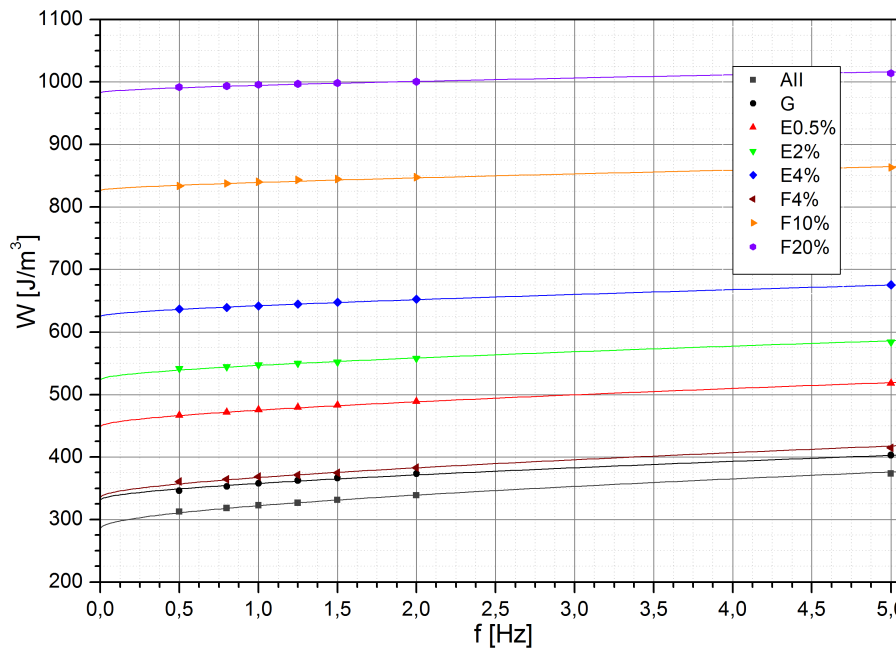
Figure 6.14: Detailed core Loss of all samples

The frequency dependence of the losses was analysed using equation 2.58. The linear eddy currents of the losses are more dominant than the excess losses, unlike

the coercivity in 6.4. In table 6.6 are the calculated parameters for the frequency dependent losses given, which correspond directly to the static, eddy current and excess losses. With the mathematical description in 2.4 these parameters can now be investigated with respect to the deformation.

Sample	W_0	σ_{W_0}	$W_{ex}/\sqrt{f}$	σ_B	W_{cl}/f	σ_C
AsCast	285.41	1.52	33.64	1.13	3.10	0.14
Reference	357.10	2.33	22.38	1.44	4.32	0.14
$\varepsilon 0.5\% - G$	431.32	1.77	22.37	1.10	4.11	0.11
$\varepsilon 2\% - G$	523.63	1.53	19.07	0.94	3.93	0.09
$\varepsilon 4\% - G$	614.80	1.04	13.16	0.64	3.86	0.06
$\varphi 4\% - G$	335.2	2.71	28.09	1.67	3.92	0.16
$\varphi 10\% - G$	826.40	2.20	9.47	1.36	3.39	0.14
$\varphi 20\% - G$	922.78	1.48	9.31	0.92	2.91	0.09

Table 6.6: Calculated loss parameter with averaged error

First the term of the classical losses will be examined. When the integral of eq. 2.53 is calculated, for the specific shape of B(t), the achieved values of the classical losses have almost the same magnitude as the experimental ones. Even though the resistivity changes with increasing deformation. This means that all the deformation information lies in the shape of B(t) and therefore the classical losses W_{cl} can not give any indication of the deformation without the measurement of the magnetic flux density .

$$\Gamma = \frac{\frac{\sigma d^2}{8} \int_0^{1/f} \left[\left| \frac{dB}{dt} \right| \frac{B(t)}{B_{max}} + \left(\frac{dB}{dt} \right)^2 \right] dt}{W_{cl} \cdot f} \tag{6.2}$$

In table 6.7 are the ratios between the by the fitting procedure derived classical losses and that by using formula 2.58 calculated classical losses at different frequencies given. For homogeneous deformation the factor describing the classical losses were calculated with an error of $\pm 10\,\%$. The deviation originates from the ansatz used in 2.4, where the cross section has infinity expansion in y-direction. The relation in eq. 6.2 can calculate the classic losses for a defined texture, but for

punched samples the results are varying. Therefore the inhomogeneity influences the frequency dependence of W_{cl}, in a way which can not be described using this simple ansatz. To verify formula 6.2, the sinusoidal losses also were analysed for this part of the thesis and the resulting ratios are displayed in table D.1.

Sample	Γ							V_0
	1Hz	2Hz	5Hz	10Hz	20Hz	50Hz	100Hz	
AsCast	0.912	1.021	1.021	1.021	1.021	1.021	1.021	0.2797
Reference	0.912	1.021	1.089	0.922	1.061	1.301	0.899	0.2418
ε0.5%-H	0.979	0.920	0.933	1.087	1.038	1.029	1.103	0.2340
ε2%-H	0.973	0.875	0.943	0.885	1.124	0.916	0.947	0.2281
ε4%-H	0.945	0.988	0.981	0.944	0.952	0.990	1.107	0.1105
φ4%-H	1.068	1.037	1.090	1.005	0.959	0.940	0.931	0.2371
φ10%-H	0.991	1.073	1.104	0.935	0.994	0.894	1.028	0.0745
φ20%-H	0.917	0.889	0.981	0.885	1.125	0.929	1.114	0.0643
P0.075/5-H	0.681	0.845	0.771	0.589	0.717	0.720	0.688	2.14
P0.075/15-H	0.753	0.699	0.805	0.671	0.634	0.844	0.809	2.20
P0.075/25-H	0.744	0.809	0.891	0.665	0.910	0.831	0.722	2.45
P0.05/5-H	0.821	0.848	0.802	0.982	0.829	0.909	0.884	2.09
P0.05/15-H	0.730	0.865	0.919	0.878	0.728	0.893	0.677	2.15
P0.05/25-H	0.878	0.978	0.928	0.738	0.860	0.758	0.968	2.37
P0.035/5-H	0.900	0.914	0.699	0.829	0.965	0.844	1.000	1.91
P0.035/15-H	0.879	0.966	0.997	0.826	0.808	0.868	0.780	1.96
P0.035/25-H	0.683	0.866	0.848	0.960	0.952	0.932	0.949	2.15

Table 6.7: Ratio between classical losses from the fitting function and the calculated, as well as the shape factor V_0 from the excess losses

The second term, the excess losses W_{ex}, on the other hand include statistical microstructure factors which are directly connected to the deformation and therefore to the residual stress. This becomes especially important for the phenomenological parameter V_0. Because the measurement was performed under constant triangular field H(t) the form factor is G=0.2 [3, p. 428]. Now V_0 can be calcula-

ted in a reverse way and the solution is given in table 6.6. With the residual stress calculated in 6.5.1 it can be assumed that V_0 follows

$$V_0 \propto \sqrt{\sigma}$$

From this observation, the induced stress rearranges the domains and therefore more energy (higher fields H(t)) is needed to align the magnetic moments and to move the domain walls. This is also supported by the hysteresis loops in 6.2.1, where higher fields are necessary to reach the full polarization as for of the *"Reference"* sample.

All three images in figure 6.15 show a distinctive dependency of all components describing the total losses on the deformation. Particularly it is worth to note that each loss contribution saturates with increasing deformation. This means that at high internal stress no influence on the shape of hysteresis loop and therefore the overall losses occurs. Sample *φ4%-H* does not follow the theory introduced in this section. This is because a deformation with $\varphi = 4\%$ is a very low factor to roll a sample. Rolling machines are designed to deform material applying high pressure and causing a severe plastic deformation of the materials. It is also possible that the low deformation causes only an elastic deformation of the material. This assumption is supported by the fact, that the *φ4%-H* has nearly the same hysteresis properties as the *"Reference"* sample.

For analysing the measurement data in figure 6.15 a special algorithm was applied in order to determine the function dependent of the different loss components on the initial stress performed on the material. This algorithm uses a set of known mathematical functions ($\sin, x^n, \exp \ldots$) to minimize the average error of the data points. Below are the such achieved functions given:

$$W_0(\sigma) = W_{0_{ini}} + D_1 \cdot \left(1 - e^{-\sigma/d_1}\right) + D_2 \cdot \left(1 - e^{-\sigma/d_2}\right) \qquad (6.3a)$$

$$W_{cl}(\sigma) = W_{cl_{sat}} + F_1 \cdot e^{-\sigma/f_1} + F_2 \cdot e^{-\sigma/f_2} \qquad (6.3b)$$

$$W_{ex}(\sigma) = G_{ini} + (G_{end} - G_{ini})\frac{x^n}{g_1^n + x^n} \qquad (6.3c)$$
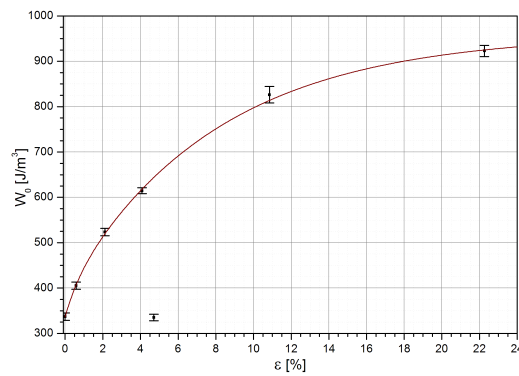
(a) static losses W_0
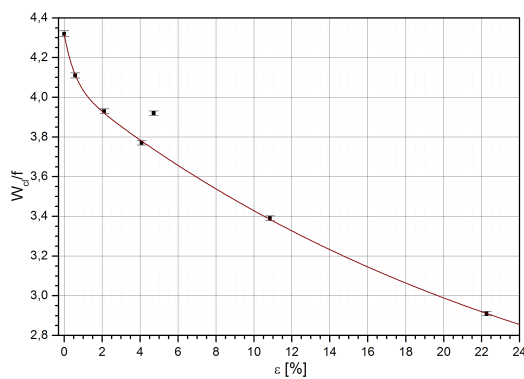
(b) classical losses W_{cl}
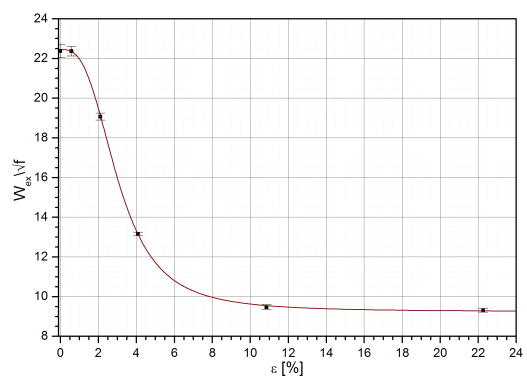
(c) excess losses W_{ex}

Figure 6.15: Fitted curves dependent on the initial deformation regarding the terms of the overall losses

Equation 6.3a and 6.3b show exponential decay behaviour. The fact that there are two exponential functions with different amplitudes and ratios indicate that more than one physical effect characterizes the different loss contributions. The second term in both equation (d_1, f_1) is related to the fast increase of stress at lower strains in the $\sigma - \varepsilon$ diagram of fig. 3.5. The third term is mainly responsible to achieve saturation at some point (until the R_m) and therefore is correlated with maximum energy induced in the lattice. The excess loss function $W_{ex}(\varepsilon)$ is commonly known as *Stirling's* function. With the general shape of the loss function the material parameters can be determined. The capitalized letters refer to an amplitude and the small are the rates of the functions.

 As the frequency dependent losses, the stress dependent loss factors are also dominated by the classical eddy currents. Based on the calculations in table 6.8 the maximum loss due to an induced stress can be calculated. With an induced stress of $\varepsilon = 0.25$, 98 % of the saturation is already reached, which leads to

$W_0 \, [J/m^3]$			W_{cl}			W_{ex}		
$W_{0_{ini}}$	336,65	±8.38	$W_{cl_{sat}}$	2.04	±0.29	G_{ini}	22.45	±0.14
D_1	52.40	±19.4	F_1	2.03	±0.27	G_{end}	9.24	±0.04
d_1	0.687	±0.672	f_1	26.28	±6.08	g_1	3.04	±0.035
D_2	570.44	±17.2	F_2	0.247	±0.034	n	2.946	±0.078
d_2	7.95	±1.48	f_2	0.543	±0.151			

Table 6.8: Material constants for the static, classical and excess losses dependent on the initial deformation

$$W_{sat} = W(\varepsilon = 0.25, f = 50Hz) = 1418.21 \, J/m^3.$$

The parameters are specifically for M400-50A electrical steel (Fe3%Si) and will change for other materials. The theory and the dependencies should stay the same and may be proven for the other steel qualities (M400-35A,M330-50A).

Losses of the punched samples

The analyses of the frequency dependence of the overall losses of the punched samples were examined using the same method as for the homogeneous ones. In fig. 6.16 all punched samples are compared with the „*Reference*" sample. There is a significant change in almost all loss parameters, which emphasizes the strong effect of an inhomogeneous stress distribution.

When the static losses W_0 are investigated further in fig. 6.17, there is a correlation between the clearance and the cutting speed. The samples are grouped by the clearance and divided by their cutting speed. With this approximation a correlation regarding the speed is possible.

Higher cutting speeds lead to smaller losses for a certain clearance. Also when a certain clearances is held constant and the cutting speed is varied, the smallest clearance lead to the minimal losses. This supports the calculated graphs, where the sample with a clearance of d=0.035mm (smallest) and a cutting speed $v_c = 25mm/s$ (fastest) exhibit the smallest overall losses. The graphs may overlap at smaller frequencies, because the cutting parameters can not be investigated
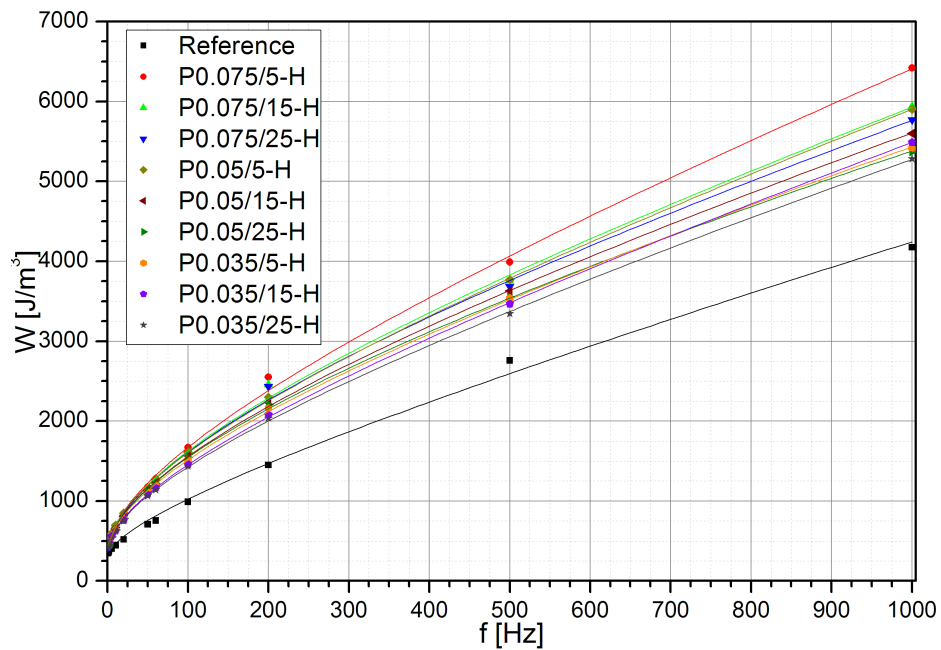
Figure 6.16: Core losses of the reference and the punched samples over a frequency range of 0.25-1000Hz
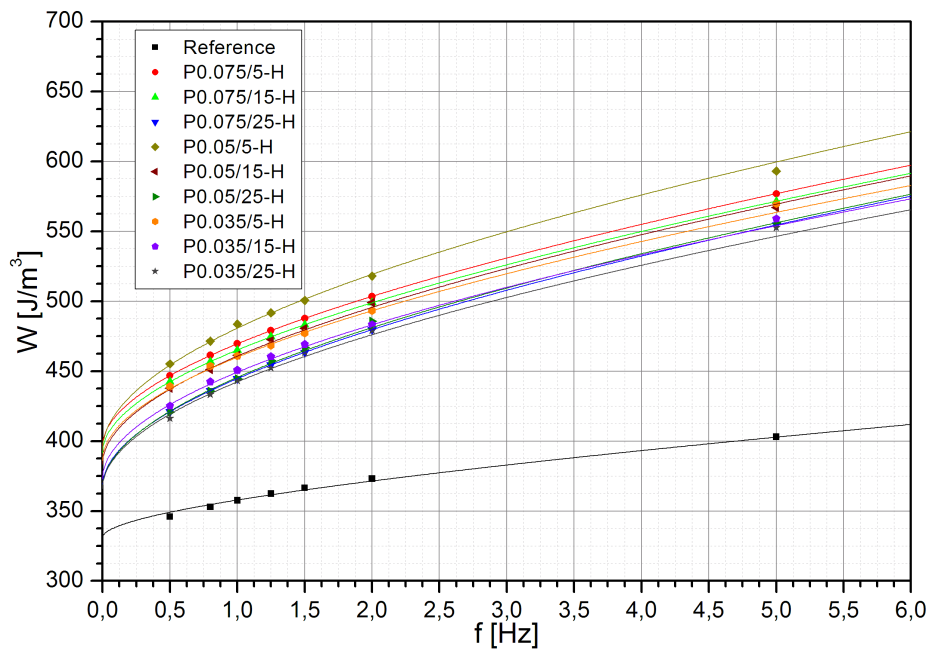
Figure 6.17: Detailed losses of the reference and the punched samples

as one set of parameters. Every clearance has three speeds, where the above argument is valid and the same applies for the three clearances at one speed.

When the loss factors where plotted over their cutting speed and show a distinctive connection between clearance and speed. This behaviour was expected, but

more samples (at least 8) at one speed may produce a more reliable dependency. The interpretation remains still inaccurate, because the losses calculated in this thesis can not consider the inhomogeneity in all directions of the material.
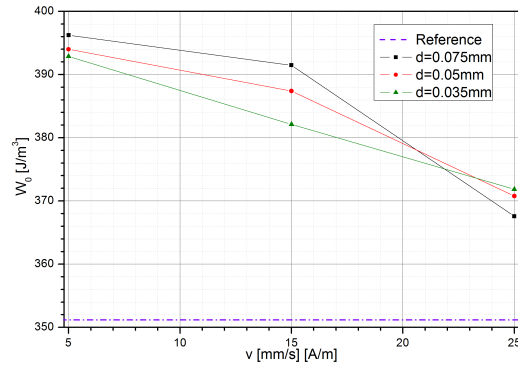
(a) static losses W_0
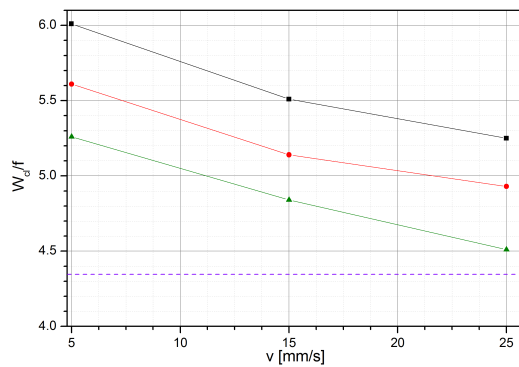
(b) classical losses W_{cl}
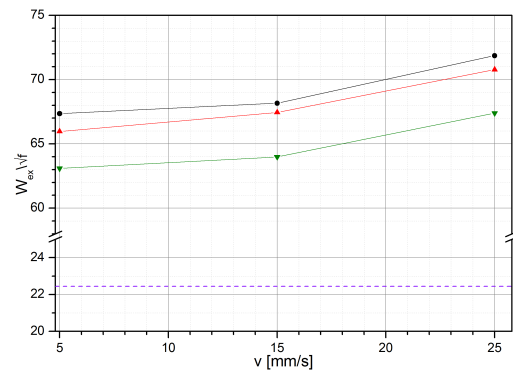
(c) excess losses W_{ex}

Figure 6.18: Separated losses of the punched samples over their cutting speed v. The purple line refers to the *Reference* sample and is independent of the cutting speed

Table 6.9 summarises the individual loss parameters with their averaged errors. These data can be used for further modelling attempts.

6.4 Coercive Field Strength H_C

The coercivity H_c describes the external field where the magnetization changes direction, which means the average magnetization becomes zero at H_c. It is one of the defining parameters of a hysteresis loop and is also needed to calculate the internal stress.

In order to use fitting equation in equation XXX more low frequency values are needed, because of the $\sqrt{f}$ dependency the linear term f would contribute

Sample	W_0	σ_{W_0}	$W_{ex}/\sqrt{f}$	σ_B	W_{cl}/f	σ_C
P0.075/5-H	396.22	2.02	67.35	0.87	6.01	0.16
P0.075/15-H	391.48	1.86	68.16	0.97	5.51	0.17
P0.075/25-H	367.58	1.80	71.86	1.05	5.25	0.20
P0.05/5-H	394.01	1.85	65.97	1.11	5.61	0.13
P0.05/15-H	387.4	1.95	67.45	0.93	5.14	0.25
P0.05/25-H	370.76	1.92	70.78	0.78	4.93	0.19
P0.035/5-H	392.87	1.91	63.09	0.79	5.26	0.18
P0.035/15-H	382.13	1.79	63.99	0.90	4.84	0.21
P0.035/25-H	371.85	1.90	67.39	0.91	4.51	0.13

Table 6.9: Calculated loss parameter for the punched samples with averaged error

mainly. To measure at very low frequencies not the whole hysteresis loop , but only the magnetic polarization around the $J(t) \sim 0$ was measured. There was a normal triangular field applied, but only a partition of the response function $\frac{d\varphi}{dt}$ was measured. Now figure 6.19 shows the coercivity over the a frequency range from 0.25-1000 Hz and 6.20 is a detailed section, where the $\sqrt{f}$ dependency clearly can be seen. At around 20-50 Hz, dependent on the sample, the coercivity of the deformed samples crosses the line of the *"Reference"*.

In order to apply the fitting process given in equation 2.59 more low frequency data are needed, because the linear term f is much larger than the of the $\sqrt{f}$ contribution. To measure at very low frequencies not the whole hysteresis loop was taken, but only the magnetic polarization around $J(t) \sim 0$ was measured. There a triangular field H(t) was applied, but only a partition of the response function $\frac{d\varphi}{dt}$ was measured. Now figure 6.19 shows the coercivity over the measured from 0.25-1000 Hz and figure 6.20 shows in a detailed section the $\sqrt{f}$ dependency. At around 20-50 Hz, the curve $H_c(f)$ of the deformed samples crosses the line of the *"Reference"* sample.

With the applied stress increasing resistivity ρ is responsible for the fact that the slope of the coercive field strength versus f is getting smaller when the eddy current influence gets dominant. This conclusion can be drawn after regarding the losses, because the frequency dependence of the coercivity follows the same
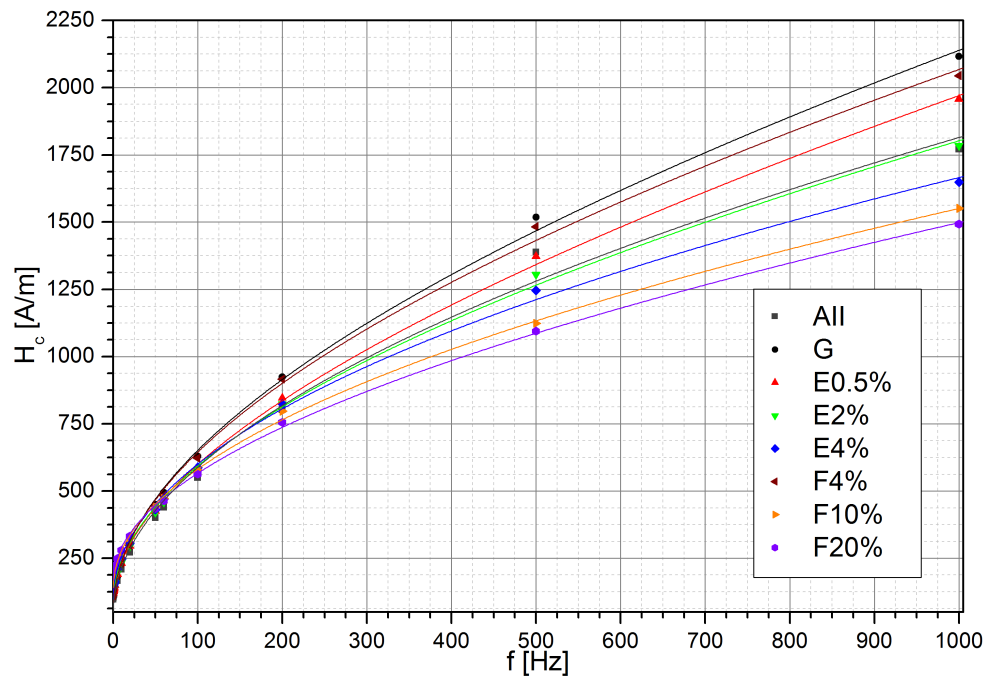
Figure 6.19: The coercitivity field H_c over the whole frequency range for homogeneous deformed samples

behaviour as that of the losses.
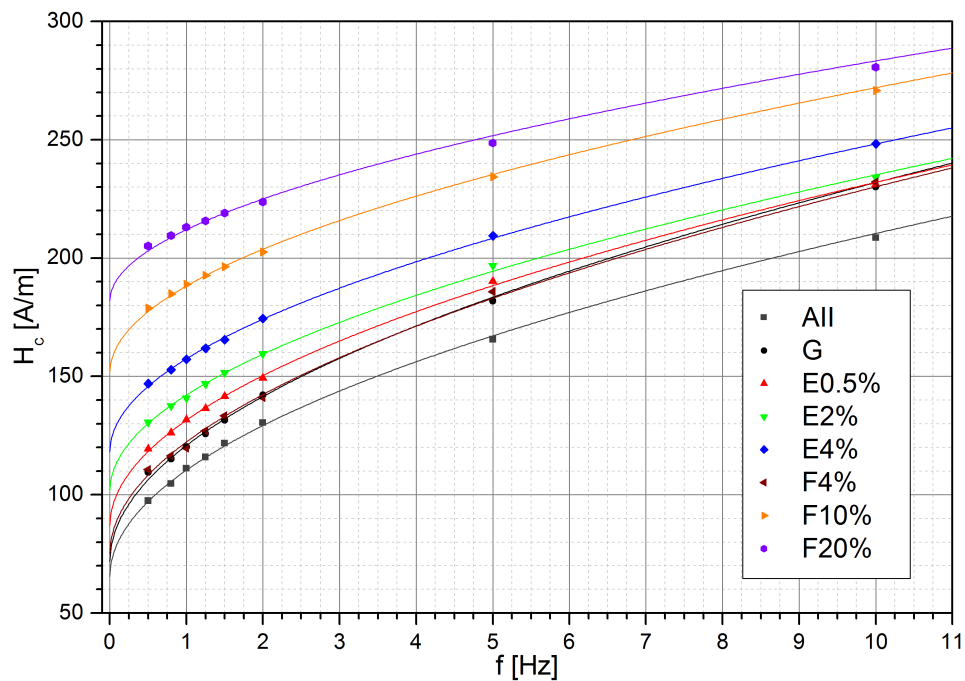
Figure 6.20: Detailed coercivity field H_c of all homogeneous deformed samples

In table 6.10 the calculated fit-parameters applying eq. 2.59 are given. In the quasi static state at 0.25 Hz the frequency independent coercivity H_{C0} has the lowest value for the *"Reference"* sample. With increasing stress, H_{C0} increases as well, which can be explained that the deformed lattice disturbs the energy balance in the crystal and therefore a higher external field $H(t)$ is required magnetize the material. It also can be observed that the linear term decreases with higher stress. This term will be referred as classical term $H_{cl} = C_1 \cdot f$ of the overall coercivity based on the designation in the losses. The same applies to the excess coercivity $H_{ex} = C_2 \cdot \sqrt{f}$. Since the frequency dependent coercivity show similarities to the losses this approximation is justified. The obvious difference is, that the coercive field depends more on the domain structure close to Hc whereas for the overall losses in the case of Fe3%Si and in the frequency range considered the classical eddy currents are dominant.

Sample	H_0 [A/m]	σ_{H_0}	C_1	σ_{C_1}	C_2	σ_{C_2}
AsCast	65.34	1.41	0.3898	0.0863	44.6561	0.8698
Reference	71.79	1.35	0.7609	0.0830	48.2420	0.83682
$\varepsilon 0.5\% - H$	86.69	0.92	0.7684	0.0562	44.2719	0.5672
$\varepsilon 2\% - H$	101.60	0.88	0.7899	0.0539	39.7555	0.5428
$\varepsilon 4\% - H$	118.15	0.71	0.8161	0.0436	38.4420	0.4393
$\varphi 4\% - H$	74.99	1.25	0.8161	0.0766	46.4837	0.7721
$\varphi 10\% - H$	151.61	0.80	0.8599	0.0491	35.1193	0.4951
$\varphi 20\% - H$	181.93	1.33	0.9153	0.0818	32.4551	0.8249

Table 6.10: Calculated parameter for the frequency dependent coercivity with averaged error

The same mathematical algorithm used for the analysis of the loss parameters was now applied on the fit parameters describing the frequency dependence of the coercivity. In figure 6.21 are the for the coercivity parameters calculated graphs given. They show also a saturation behaviour, which leads to the conclusion, that at a certain deformation the coercive field strength does not change anymore with applied stress. As explained in 6.3 the sample φ4-*H* was not deformed enough to truly represent a $\varphi = 4\%$ state and was excluded in the analysis.
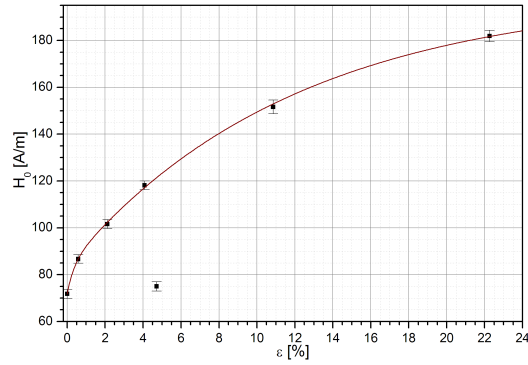
(a) static coercive field strength H_0
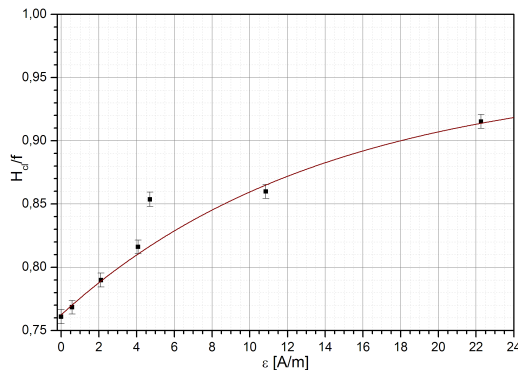
(b) classical term H_{cl}
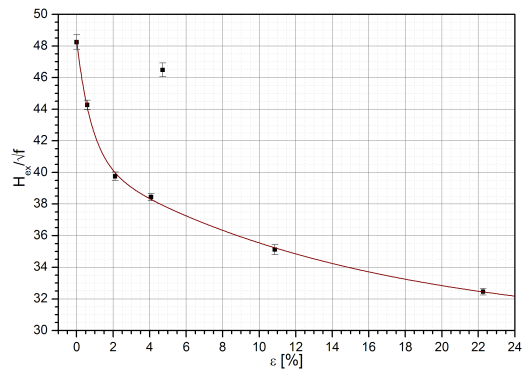
(c) excess term H_{ex}

Figure 6.21: Fitted curves dependent on the initial deformation regarding the terms of the coercive field strength

The functions in eq. 6.4a and 6.4c show also two different exponential terms, which supports the theory, that more than one physical effect effects these functions. From the experimental data, the amplitudes (upper case variables) and the rates (lower case) can be determined for M400-50A electrical steel and are listed in table 6.11.

$$H_0(\varepsilon) = H_{0_{sat}} + H_1 \cdot e^{-\varepsilon/h_1} + H_2 \cdot e^{-\varepsilon/h_2} \qquad (6.4a)$$

$$H_{cl}(\varepsilon) = H_{cl_0} + J_1 \left(\frac{e^{j_1 \varepsilon} - 1}{j_1} \right) \qquad (6.4b)$$

$$H_{ex}(\varepsilon) = H_{ex_{sat}} + K_1 \cdot e^{-\varepsilon/k_1} + K_2 \cdot e^{-\varepsilon/k_2} \qquad (6.4c)$$

Using all the parameters the coercivity, as a function of stress, can be calculated for any frequency and deformation state, which arrives at 99% saturation already at $\varepsilon = 0.22$ and a saturation value $H_{sat} = H(\varepsilon = 0.22, f = 50Hz) = 459.61\,A/m$. This value is the maximum coercive field possible due to a preceding deformation

$H_0\ [A/m]$			H_{cl}			H_{ex}		
$H_{0_{sat}}$	199.60	±7.3	H_{cl_0}	0.762	±0.003	$H_{ex_{sat}}$	30.04	±2.23
H_1	-116.11	±5.25	J_1	0.0136	±0.002	K_1	10.80	±1.46
h_1	11.91	±1.94	j_1	-0.0716	±0.013	k_1	14.82	±7.50
H_2	-11.69	±3.72				K_2	7.51	±1.05
h_2	0.361	±0.25				k_2	0.822	±0.21

Table 6.11: Material constants for the static, classical and excess coercive field dependent on the initial deformation

Coercive field strength of the punched sampled

Similar as for the homogeneously deformed samples the punched samples show a distinctive characteristics regarding their deformation and frequency behaviour. Because the difference between the clearance and speed is ¡20A/m further investigation was proven difficult. The theoretical approach to the coercive field strength is based on simple considerations and do not include a more complex disturbance in the lattice.
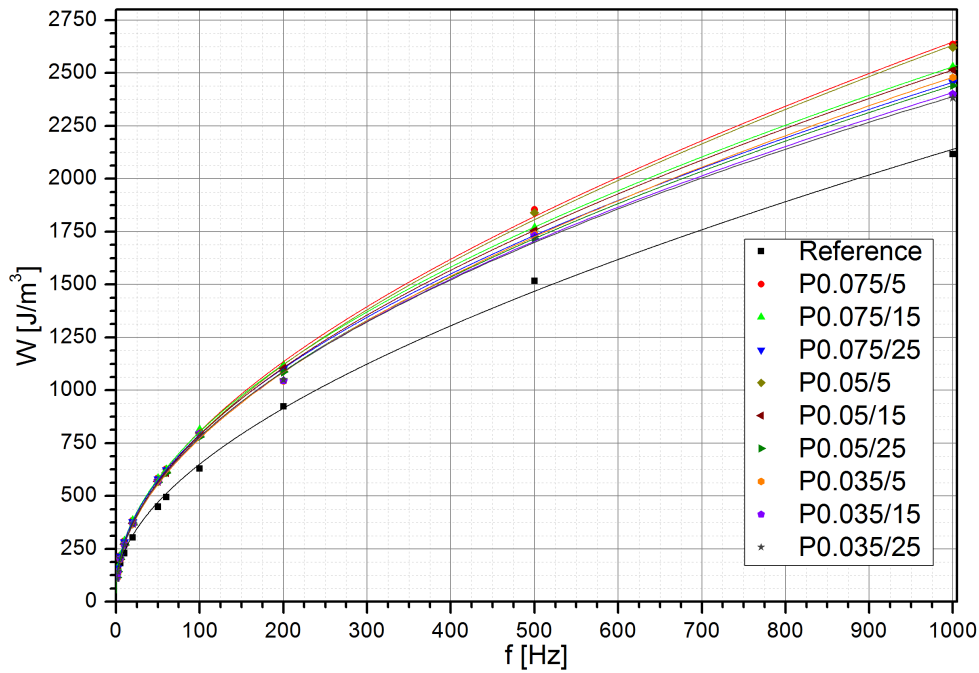
Figure 6.22: coercivity field H_c of the punched samples over the frequency of 0.25-1000Hz

Table 6.12 gives all calculated parameters for the coercive field strength, but no reliable dependency regarding the deformation could be observed. Only the static field H_{c0} shows the expected behaviour as described in 6.3.

Sample	H_0	σ_{H_0}	C_1	σ_{C_1}	C_2	σ_{C_2}
P0.075/5-H	57.00	1.79	0.309	0.14	70.89	0.78
P0.075/15-H	54.57	1.75	0.164	0.15	72.99	0.90
P0.075/25-H	54.67	1.81	0.0997	0.14	72.78	0.71
P0.05/5-H	42.00	2.12	0.317	0.19	71.91	0.82
P0.05/15-H	39.68	1.93	0.164	0.12	72.99	0.91
P0.05/25-H	39.57	1.89	0.0917	0.15	70.86	0.79
P0.035/5-H	45.17	1.91	0.198	0.13	70.75	0.88
P0.035/15-H	39.15	1.95	0.042	0.14	73.54	0.92
P0.035/25-H	38.48	2.01	0.10	0.07	74.07	0.88

Table 6.12: Calculated coercive field strength parameter for the punched samples with averaged error

6.5 Magnetostriction

As described in 2.3 the saturation magnetostriction λ_{sat} of a polycrystalline material can be calculated using the measured magnetostriction longitudinal and transversal to the the applied field. For an isotropic polycrystalline material the factor $\frac{2}{3}$ is achieved as a prefactor considering eq. 2.38. Like the magnetic hysteresis the magnetostriction also has to have a similar saturation characteristic. It is not possible that the saturation magnetostriction of a deformed material has a lower or a higher value than that of an undeformed material, as long as the crystal structure (here BCC) remains the same.

Figure 6.23 shows the quasi static magnetostriction of the homogeneous deformed samples. The the longitudinal magnetostriction λ_L, which is the MS in direction of the applied field H(t), is almost unaffected by the deformation. The transverse magnetostriction λ_T on the other hand are clearly affected from the deformed lattice. The more the material is deformed, the smaller the λ_T gets.
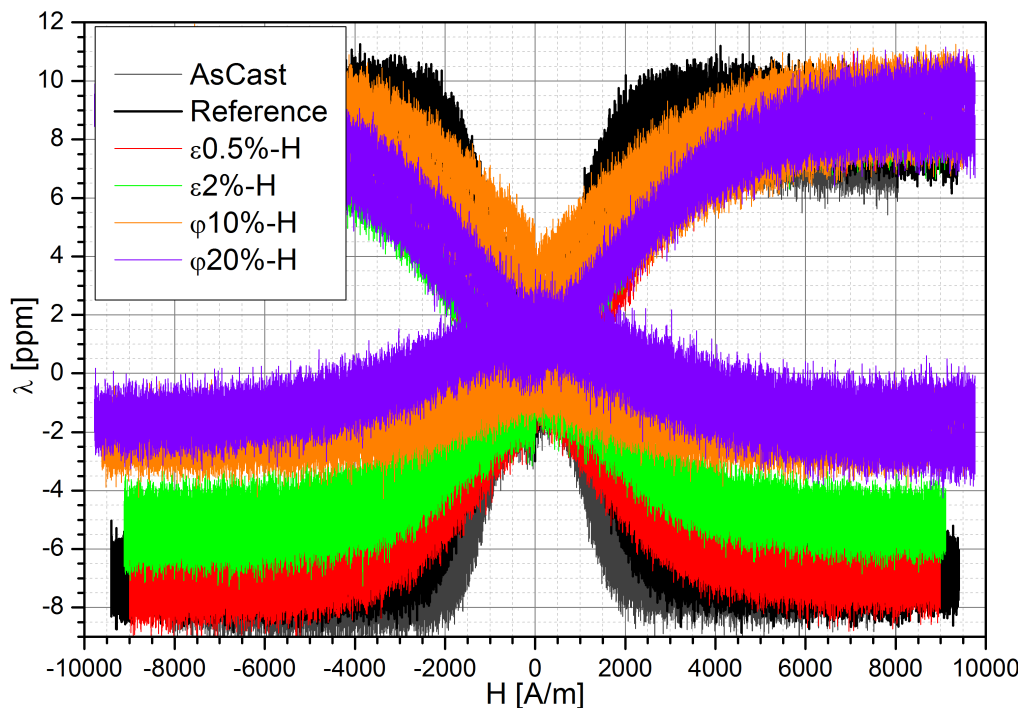
Figure 6.23: Longitudinal (up) and transverse (down) magnetostriction at 1 Hz for the homogeneous deformed sample

With increasing frequency (see fig. 6.24) the saturation values of the longitudinal and transverse MS stay unchanged. Also the distinctive loops can be detected,

which show similarity to a coercive field, because the loops are getting wider with increasing frequency. Due to the soft magnetic nature of M400-50A the loops are very narrow, which also supports a connection between the coercivity and the width of the loops. In figure 6.25 are all the magnetostriction measurements at certain frequencies shown. Above 200 Hz not enough points can be acquired to differentiate the signal from the noise and will not be shown.
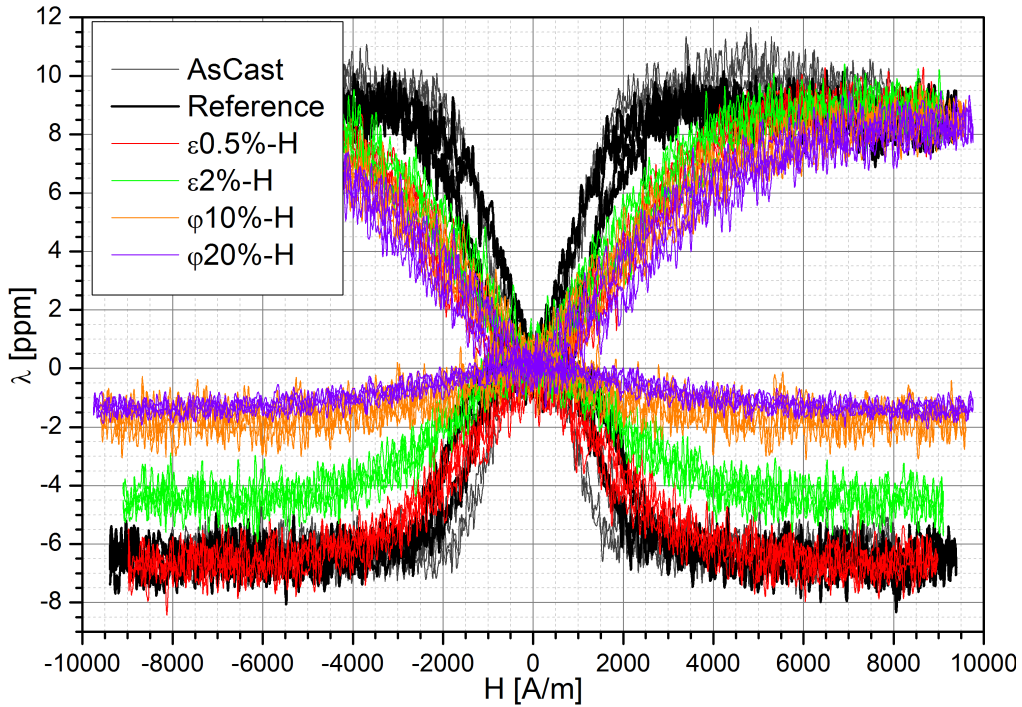
Figure 6.24: Longitudinal (up) and transverse (down) magnetostriction at 50 Hz for the homogeneous deformed sample

The shape of the MS has a similar behaviour as the hysteresis loops, where with increasing deformation the slope dB/dH becomes smaller. At higher external fields more energy is needed to approach the full transverse magnetostriction values as in the case of the *"Reference"* sample. The deformation also suppresses the formation of distinctive (*butterfly*) loop shapes of MS(H).

The saturation magnetostriction λ_s can be calculated for an undeformed crystal structure using eq. 2.38. The factor $\frac{2}{3}$ must be modified to consider an external or internal deformation, which causes the texture.

$$\lambda_s = \frac{2}{3} \cdot \gamma \cdot (\lambda_L - \lambda_T) \tag{6.5}$$
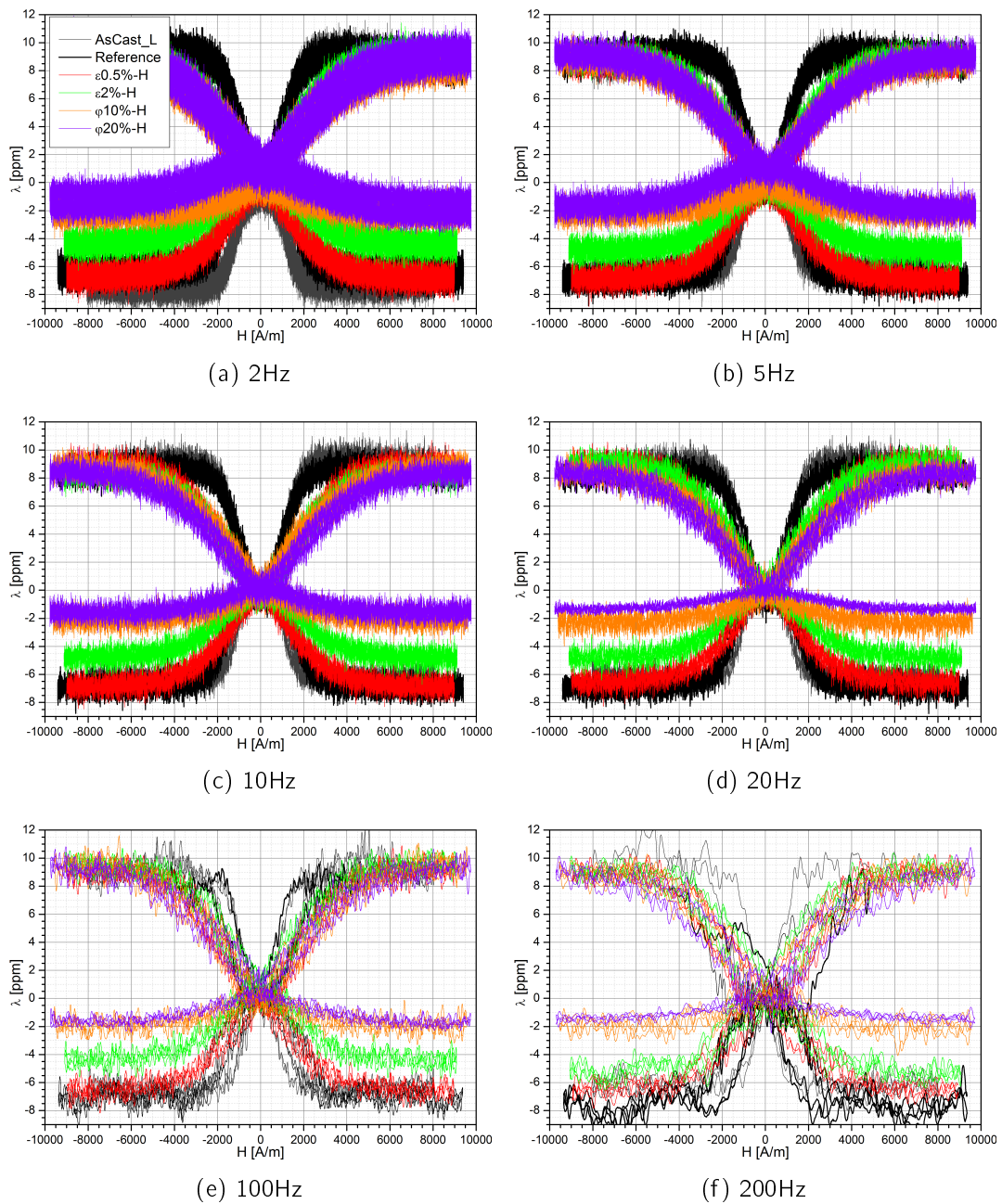
Figure 6.25: Magnetostriction λ of the homogeneous deformed samples at a certain frequency

Also due to the stress induced texture in the material the magnetic domains are more aligned in the direction of the texture. When a field is applied parallel to the texture direction, the magnetization vectors align easier in this direction. The magnetostriction has not to overcome an additional energy and therefore the longitudinal MS $\lambda_{\parallel}$ does not change under deformation. Applying now the field

perpendicular to the texture on the other hand the magnetization vectors α_i have to rotate against the local stress energy, therefore the transverse magnetostriction $\lambda_\perp$ must overcome the deformation energy. The value of $\lambda_\perp$ should reach zero when the material exhibit a texture only in one direction (all magnetization vectors α_i are aligned in this direction).

6.5.1 Comparison and residual stress

In order to compare the different stress induced local textures the pre factors of the deformed samples will be correlated with the undeformed saturation magnetostriction. To calculate the saturation magnetostriction now the anisotropy saturation constant γ is introduced in eq. 6.5. The estimated lattice constants are shown in table 6.13. The factor γ indicates how much texture appears due to the deformation, under the condition that the texture occurs only in one direction.
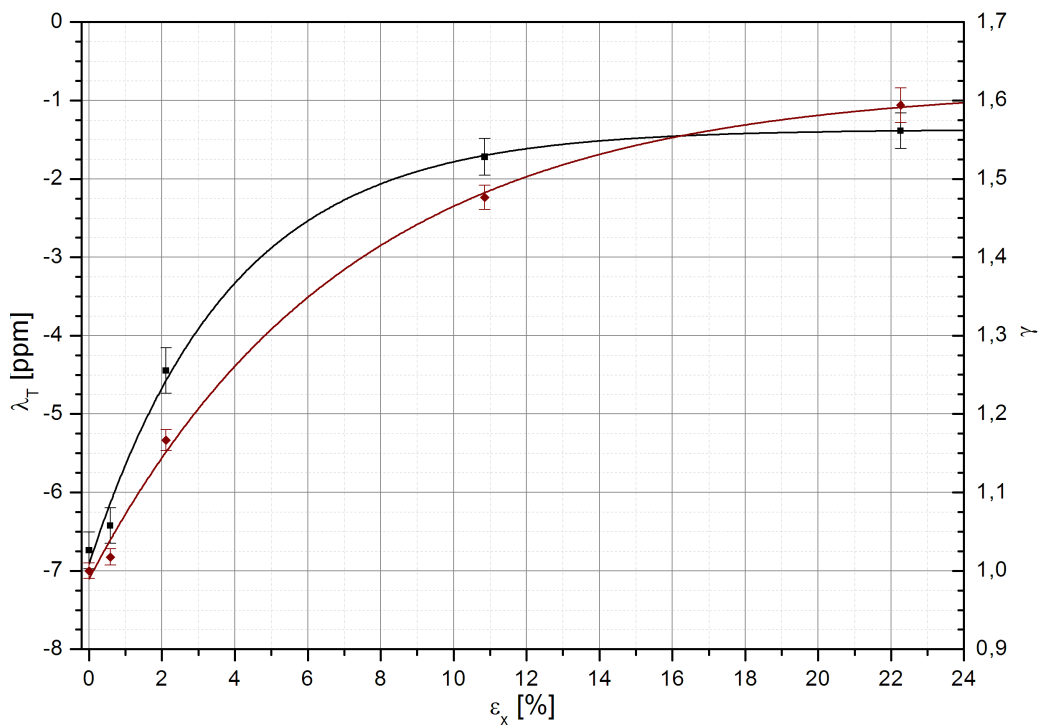
Figure 6.26: Fitted values for the transverse magnetostriction λ_T (black) and the saturation anisotropy constant γ (red)

As for the stress behaviour of the coercive field and of the losses, a saturation behaviour can be observed also for the magnetostriction. Also in this case a function is used to describe stress behaviour of the magnetostriction. The functions

are again a *Stirling* type.

$$\lambda_T(\varepsilon) = \lambda_{T_0} + U_1 \frac{e^{u_1 \varepsilon} - 1}{u_1} \tag{6.6a}$$

$$\gamma(\varepsilon) = \gamma_0 + V_1 \frac{e^{v_1 \varepsilon} - 1}{v_1} \tag{6.6b}$$

From the fitting process the amplitudes and the rates were obtained and listed in table 6.13. Now the saturation value of the transverse magnetostriction $\lambda_\parallel$ arrives $\lambda_{T_{sat}} = \lambda_T(\sigma = 0.22) = -1.373$. The initial anisotropy constant γ_0 should be exactly 1, because it was normalized using the "Reference" sample. Through the fitting process an error on all values has to be expected, but they are in a reasonable margin, which ensures the validity of the data. Inserting the parameters give $\gamma_{sat} = \gamma(\epsilon = 0.22) = 1.627$.

	λ_T [*ppm*]			γ			σ_{res} [*MPa*]·	
λ_{T_0}	-6.9134	±0.215	γ_0	0.9985	±0.0154	σ_{res_0}	4.615	±0.358
U_1	1.4410	±0.093	V_1	0.0887	±0.0122	$\sigma_{res_{sat}}$	150.21	±0.76
u_1	-0.2601	±0.046	v_1	-0.1412	±0.0227	ε_0	6.127	±0.101
						p	2.023	0.144
$\lambda_T(\infty) = \lambda_{T_{sat}} = -1.3723$			$\gamma(\infty) = \gamma_{sat} = 1.6182$			$\sigma(\infty) = \sigma_{res_{sat}} = 150.21 \, MPa$		

Table 6.13: Calculated function parameters for the transverse magnetostriction λ_T, the anisotropy saturation constant γ and the residual stress σ_{res}

With the measurement of the magnetostriction and the properties of the hysteresis loops it is possible to estimate the *residual stress* σ_{res} in the material. As described in 2.3.5 the calculated residual stress in eq. 2.44 gives only the averaged stress throughout the material. This equation needs the static coercive field H_{C_0} and the *effective magnetocrystalline constant* K_{eff} introduced in 2.3. For Fe3%Si the constant $K_{eff} = 144.51 \, J/m^3$, which was calculated using the reference sample and the magnetocrystalline constants K_1 and K_2 [23] and the

saturation polarization $J_s = 2.05\,T$ was determined in 6.2.3. The results are listed in 6.13 and are visualized in figure 6.27.
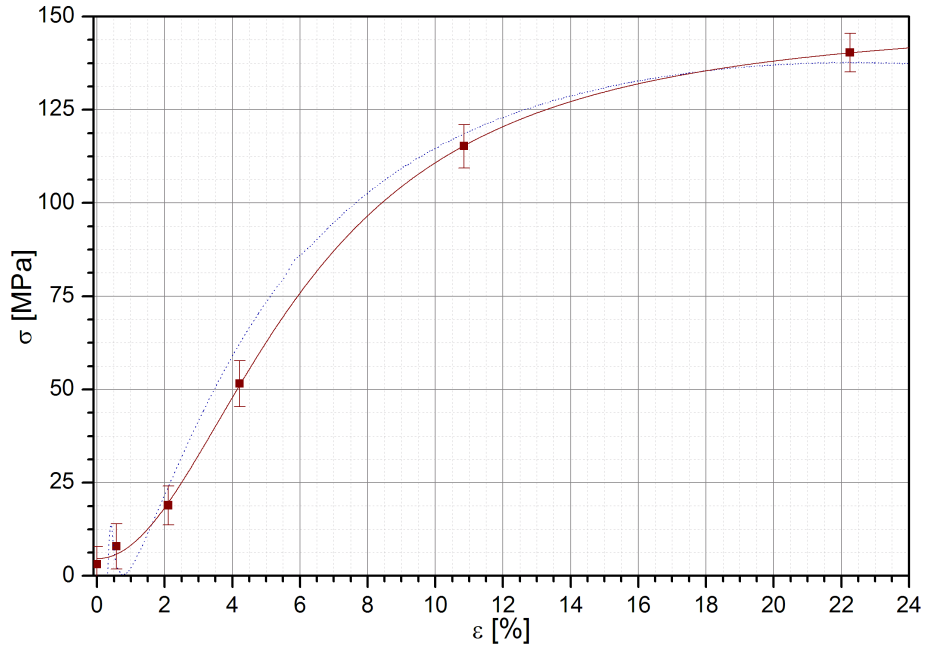
Figure 6.27: Data points and fitted function for the residual stress σ_{res} in comparison to the shifted $\varepsilon - \sigma$ curve (blue)

The function corresponds to a logistic behaviour, although the function has to be modified to minimize the error of the data points.

$$\sigma_{res}(\varepsilon) = \frac{\sigma_{res_0} - \sigma_{res_{sat}}}{1 + \left(\frac{\varepsilon}{\varepsilon_0}\right)^p} + \sigma_{res_{sat}} \tag{6.7}$$

7 Conclusion

According to the various hysteresis measurements and the analysis of the data as shown in this thesis, the influence of the internal stress after different deformation processes, on magnetic properties (hysteresis, polarization J(t), magnetostriction, losses,...) became understandable. It was shown, that the losses are directly correlated to any internal or external stress state. Especially the static losses W_0 increase with the stress. The magnetization vectors α_i of the material in a defined texture (rolling, tensile) are rotating towards the texture. Therefore the magnetization process parallel to the texture-direction is easier than perpendicular to it. The overall magnetization process needs more energy to magnetize a deformed material, because the energy from the magnetoelastic energy due to an internal stress must be overcome. The deformation effect on the shape of the hysteresis can be directly observed by plotting the hysteresis loops above each other (fig. 6.9). The slope of the B(H) loops change strongest where the permeability exhibit its maximum, but they all saturate at the same polarization $J_s = 2.05\,T$. The saturation magnetization is constant and independent from mechanical influence or heat treatment. Contrary the coercive field strength H_c increases with stress, which supports the energy argument from above.

 The electrical resistivity ρ also changes, because of the deformation causes dislocations and local stress centers. Because the classic and excess losses are indirect proportional to the electric resistivity, the overall losses of the deformed samples become at higher frequencies smaller than that of the reference sample (see fig. 6.13) . In these figures the curves losses versus frequency are getting more flat with increasing deformation and therefore the excess and the classical losses are decreasing, which is shown in fig. 6.15b and 6.15c. When the individual loss coefficients are investigated further, more information on the magnetization process is revealed. With the in eq. 2.53 derived formula the classical losses can be directly calculated considering the function of the magnetic flux density B(t). This suggests, that most of the deformation information is in the shape of the magnetic flux density B(t). More interesting is the evaluation of the excess losses. The classical losses can be understood using Maxwell's equation, whereas the excess losses are connected to the micro structure. The excess losses are not fully understood yet. The form factor V_0 is the first order simplification to describe all micro magnetic processes. This has encouraged the conclusion, that all external

influences must be connected with this parameter. With the experiments performed in this work only macroscopic effects can be evaluated correctly, therefore the interpretation is based on the overall change of the micro magnetic system, which includes all influences (domain size, domain movement, atomic interaction, spin coupling,...). Nevertheless the dependency of a homogeneous deformation can be correlated to the factor V_0 in first order, which leads to a simple distribution $V_0 \propto \sqrt{\sigma_{res}}$.

The losses of the punched samples change drastically under external stress. Especially at higher frequencies they vary strongly compared to the „Reference" sample. The graphs of the losses versus frequency in fig. 6.16 overlap regarding their clearance, but show a correlated behaviour with the cutting speed. Faster punches lead to smaller losses for every clearance and reaches its lowest value for d=0.035 mm. The inhomogeneous deformation is localized on the edges (¡10 mm). With the 5 mm gap of the ring samples, this inhomogeneity can be fully detected and correctly interpreted. Applications with small dimensions (e.g. electric motors) can profit from this information, because the loss difference to the reference sample can be more than 10% for f=50 Hz.

Another independent, important property which was measured was the magnetostriction in longitudinal $\lambda_\parallel$ and perpendicular $\lambda_\perp$ direction to the applied field. The transverse magnetostriction decreases with increasing deformation. This is because of the texture direction of the deformed material. When the texture is perpendicular to the external field, the magnetostriction is already compensated. $\lambda_\perp=0$ when all the magnetization vectors are aligned because of the deformation, which is supported by the derivation in 6.5 for the stress dependent magnetostriction. The magnetostriction also follows a similar hysteresis loops at low fields. This, commonly referred as butterfly, is very similar to the magnetic hysteresis. It also changes the slope with increasing deformation. The area and the position of the magnetostriction versus field curve may be correlated with the losses and the coercivity.

The saturation magnetostriction λ_s must have the same value for all samples (similar to the saturation polarization J_s). To achieve this, the *anisotropy magnetostriction constant* γ was introduced in 2.3, which contains the information about the deformation process. Now with the relation in 2.3 the residual stress in the material can be calculated, with the static coercive field strength H_{c0} and the *effective magnetocrystalline constant* $\langle K_{eff} \rangle$. The residual stress σ_{res} was com-

pared the inelastic part of the $\sigma - \varepsilon$ graph, which shows similarity to the inelastic stress induced in the material.

7.1 Future Work

The EDT department of the AIT searched for a calculation method to predict the magnetic losses of deformed material. Simon Ertl developed in his masterthesis a model based on the theory of Jiles and Atherton. With the experimental data, this model can be verified and improved.

Since the mechanical deformation changes the magnetic properties it can be assumed, that a high temperature also effects them. The temperature dependence of the magnetic properties is of interest for electrical motors and generators, which intend to heat up during operation. Therefore a set of deformed samples has to be measured at certain temperatures. The additional energy induced in the material will change the loss coefficients. In first order perturbation theory all induced energies can be calculated separately and summed up. Most stress effects happen in the microstructure and there is no ansatz which allows to include into the Hamiltonian for the magnetic exchange coupling extensions such as temperature or the deformation tensor. To investigate the real behaviour the micromagnetism must be observed. Applying electron microscopy allows to determine the crystal structure the grains size and local defects. For a certain microstructure the domains of the material during magnetization process can be observed using Kerr's method. This may help to correlate the form factor V_0 and excess losses applying a well defined deformation.

The material in this thesis was M400-50A (Fe3%Si) electrical steel. The values obtained from the experiments were compared with data sheets of the same material. Another task is now to compare the calculations determined in this work with other steel qualities. Therefore the punched samples with the same parameters (clearance, cutting speed) were also produced for M400-35A and M330-50A.

Literature

[1] A. Aharoni: „*Introduction to the Theory of Ferromagnetism* “. Oxford Science Publications: Oxford, 2000.

[2] R. Becker and W. Döring: „*Ferromagnetismus* “. Springer: Berlin, 1939.

[3] G. Bertotti: „*Hysteresis in Magnetism* “. Academic Press: San Diego, 1998.

[4] „*BNC 2110 Installation Guide* “. National Instruments, 2007.

[5] R. Bozorth: „*Ferromagnetism* “. D. Van Nostrand Co, 1951.

[6] A. delMoral: „*Handbook of Magnetostriction and Magnetostrictive Materials* “. Del Moral: Saragossa, 2008, vol. 1.

[7] „*DMS Series Y* “. HBM, 2011.

[8] „*Electrical Steel Strip* “. Voest Alpine, 2013.

[9] S. Ertl: „Simulating the change of magnetic hysteresis due to the cut of nonoriented steel sheet“. Diplomarbeit. Wien: TU Wien, 2013.

[10] R. Fischer, T. Schrefl, H. Kronmüller, and J. Fidler: „*Grain-size dependence of remanence and coercive field of isotropic nanocrystalline composite permanent magnets* “. In: *Journal of Magnetism and Magnetic Materials*, Volume 153, Max-Planck-Institut für Metallforschung, pp. 35–39, 1996.

[11] R. Grössinger: „*A critical examination of the law of approach to saturation. I. Fit procedure* “. In: *Physica Status Solidi (a)*, Volume 66, pp. 665–674, 1994.

[12] S. Hartl: „Einfluss des Luftspaltes auf gewickelte Ringproben“. Projektarbeit. Wien: TU Wien, 2013.

[13] S. Hartl: „Hysteresograph“. Projektarbeit. Wien: Tu Wien, 2013.

[14] A. Huber and R. Schäfer: „*Magnetic Domains - The Analysis of Magnetic Microstructure* “. Springer Verlag: Dresden, 1998.

[15] E. Hug, O. Hubert, and J. VanHoutte: „*Effect of internal stresses on the magnetic properties of non-oriented Fe-3wt.% Si and (Fe,Co)-2wt.% V alloys* “. In: *Material Science and Engineering A 332*, pp. 193–202, 2001.

[16] „*Instruction Manual KEPCO 100-4* “. KEPCO, INC., 1994.

[17]   V. Iordache, E. Hug, and N. Buiron: „*Magnetic behaviour versus tensile deformation mechanisms in a nonoriented Fe-(3 wt.%)Si steel*". In: *Materials Science and Engineering A359*, pp. 62–74, 2003.

[18]   J. Jackson: „*Klassische Elektrodynamik*". de Gruyter, 1993, vol. 2.

[19]   D. Jiles: „*Introduction to Magnetism and Magnetic Materials*". Taylor and Francis: Ames, 1997.

[20]   C. Kittel: „*Introduction to Solid State Physics*". John Wiley and Sons Inc: New York, 2005, 8th ed.

[21]   C. Kittel: „*Physical Theory of Ferromagnetic Domains*". In: *Revision of Modern Physics*, Volume 21, p. 541, 1949.

[22]   H. Kronmüller and A. Seeger: „*Theorie des Einmündungsgesetzes in plastisch verformten kubisch-flächenzentrierten Einkristallen*". In: *Journal of Physics and Chemistry of Solids*, Volume 18, pp. 93–115, 1961.

[23]   H. Landolt and R. Börnstein: „*Magnetic Properties of Metals*". Springer Verlag: Berlin-Heidelberg, 1994, vol. 19.

[24]   Mathew, Kaul, and Nigam: „*Magnetic irreversibility, spin-wave excitations and magnetocaloric effect in nanocrystalline Gadolinium*". In: *Journal of Physics*, Volume Conference Series 200, 2009.

[25]   N. Mehboob: „Hysteresis of Soft Magnetic Materials". Dissertation. Wien: Universität Wien, 2012.

[26]   R. Neugebauer: „*Umform- und Zerteiltechnik*". Wissenschaftliche Scripten: Chemnitz, 2005. Ed. by F. Institut.

[27]   „*NI 6115/6120 User Manual*". National Instruments, 2003.

[28]   J. Nye: „*Physical Properties of Crystals*". Oxford Science Publications: Oxford, 1976.

[29]   P. Oser: „Ein Hysteresograph zur Charakterisierung weichmagnetischer Materialien". Diplomarbeit. Wien: TU Wien, 2008.

[30]   B. Predel: „*Fe-Si (Iron-Silicon)*". In: *Landolt-Börnstein - Group IV Physical Chemistry*, Volume 5e, pp. 1–6, 1995.

[31] R. PremKumar and J. Samajdar: „*Relative effect(s) of texture and grain size on magnetic properties in a low silicon non-grain oriented electrical steel*". In: *Journal of Magnetism and Magnetic Materials*, Volume 264, pp. 75–86, 2006.

[32] D. L. Rodrigues-Jr: „*Effect of Plastic Deformation on the Excess Loss of Electrical Steel*". In: *IEEE Transactions on Magnetics*, Volume 48, Escola Politecnica da Universidade de Sao Paulo, 2012.

[33] S. Scheriau, M. Kriegisch, and S. Kleber: „*Magnetic characteristics of HPT deformed soft-magnetic materials*". In: *Journal of Magnetism and Magnetic Materials*, Volume 322(20), pp. 2984–2988, 2010.

[34] A. Schnabl, S. Knappe-Gruenberg, and D. Stollfuss: „*Proposal of a Demagnetization Function*". In: *IEEE Transactions on Magnetics*, Volume 43, pp. 2959–2961, 2007.

[35] J. Snoek: „*The Weiss-Heisenberg Theory of Ferro-magnetism and a New Rule Concerning Magnetostriction and Magneto-Resistance*". In: *Nature*, Volume 163, pp. 837–838, 1946.

[36] N. Takahashi and D. Miyagi: „*Effect of Stress on Iron Loss of Motor Core*". In: *IEEE International Electric Machines & Drives Conference*, Okayama University, 2011.

[37] S. Treml: „Simulation der Werkstofftrennung beim Schneiden". Masterthesis. Mittweida: Hochschule Mittweida, 2004.

[38] E. Villari: „*Change of Magnetization by Tension and by Electric Current*". In: *Annalen der Physik Leipzig*, Volume 126, p. 87, 1865.

Appendix

A Magnetostriction

A.1 Elastic Energy F_{el}

From the general expression

$$F_{el} = c_{ijkl}\varepsilon_{ij}\varepsilon_{kl}$$

and using repeating notations over i=1,2,3 the *Voigt's* notation $c_{ijkl} \to c_{nm}$ can be used.

$$\varepsilon_{ijk} = \begin{pmatrix} \varepsilon_{11} \\ \varepsilon_{22} \\ \varepsilon_{33} \\ 2\varepsilon_{23} \\ 2\varepsilon_{13} \\ 2\varepsilon_{12} \end{pmatrix}$$

The first independent with i=1 ($\to j = k = l = 1$) now reads

$$(1/2) \cdot c_{1111}\varepsilon_{11}\varepsilon_{11} \mathrel{\hat{=}} (1/2) \cdot c_{11}\varepsilon_{11}^2$$

For the cubic lattice is $c_{11} = c_{22} = c_{33}$. Therefore the first time gives

$$(1/2) \cdot c_{11}(\varepsilon_{11} + \varepsilon_{22} + \varepsilon_{33})$$

The factor $(1/2)$ arrives from the Voigt's notation and will be applied by the symmetric terms $(11 \ldots 33)$ rather than the unsymmetrical. The second notation i=1,j=1 and k=2,l=2 gives

$$c_{1122}(\varepsilon_{11}\varepsilon_{22} + \varepsilon_{22}\varepsilon_{33} + \varepsilon_{33}\varepsilon_{11}) \mathrel{\hat{=}} c_{12}(\varepsilon_{11}\varepsilon_{22} + \varepsilon_{22}\varepsilon_{33} + \varepsilon_{33}\varepsilon_{11})$$

Here also $c_{12} = c_{13} = c_{23}$ is valid. With the independent index i=4 ($\to j = k = l = 4$) the strain tensors ε can be represented with the three dimensional notation, where every entry now appears twice, when *jkl* go through $1 \ldots 3$

$$2 \cdot c_{4444}(\varepsilon_{12}\varepsilon_{12} + \varepsilon_{13}\varepsilon_{13} + \varepsilon_{23}\varepsilon_{23}) \mathrel{\hat{=}} 2 \cdot c_{44}(\varepsilon_{12}^2 + \varepsilon_{13}^2 + \varepsilon_{23}^2)$$

The resulting elastic energy gives then

$$F_{el} = (1/2) \cdot c_{11}(\varepsilon_{11} + \varepsilon_{22} + \varepsilon_{33}) + c_{12}(\varepsilon_{11}\varepsilon_{22} + \varepsilon_{22}\varepsilon_{33} + \varepsilon_{33}\varepsilon_{11}) + 2 \cdot c_{44}(\varepsilon_{12}^2 + \varepsilon_{13}^2 + \varepsilon_{23}^2)$$

The same steps regarding the index summation can be used for the magnetoelastic energy F_{mel} and the magnetocrystalline energy $F_K(\vec{\alpha})$

A.2 Calculation of saturation magnetostriction

Consistently applying the new coordinates

$$\alpha_1 = \cos\xi \sin\theta \cos\phi + \sin\xi(\cos\theta \cos\phi \cos\psi + \sin\phi \sin\psi)$$
$$\alpha_2 = \cos\xi \sin\theta \sin\phi + \sin\xi(\cos\theta \sin\phi \cos\psi + \cos\phi \sin\psi)$$
$$\alpha_3 = \cos\xi \cos\theta - \sin\xi \sin\theta \cos\psi$$
$$\beta_1 = \sin\theta \cos\phi \qquad \beta_2 = \sin\theta \sin\phi \qquad \beta_3 = \cos\theta$$

in the *Becker & Döring* equation

$$F_k(\vec{\alpha}) = K_i\alpha_i + K_{ij}\alpha_i\alpha_j \qquad\qquad + \cdots + K_{ijkl}\alpha_i\alpha_j\alpha_k\alpha_l$$
$$E_{mel}(\vec{\alpha}, \varepsilon_{ij}) = \qquad\qquad \overline{M}_{ijk}\alpha_i\varepsilon_{jk} + \overline{M}_{ijkl}\alpha_i\alpha_j\varepsilon_{kl}$$
$$F_{el}(\varepsilon_{ij}) = \qquad\qquad c_{ijkl}\varepsilon_{ij}\varepsilon_{kl}$$

and inserting it into the spontaneous magnetostriction $\bar{\lambda}$ gives up to the fifth order

$$\bar{\lambda} = \left(h_0 + \frac{1}{5}h_1 - \frac{1}{5}h_2 + \frac{1}{5}h_3 + \frac{23}{105}h_4 - \frac{1}{35}h_5\right) +$$
$$+ \left(\frac{2}{5}h_1 - \frac{3}{5}h_2 + \frac{12}{35}h_4 + \frac{3}{35}h_5\right) \cdot \cos^2(\xi)$$

For the $\langle 100 \rangle$ and $\langle 111 \rangle$ direction the initial magnetostriction can be obtained with the equation above using for $\langle 100 \rangle \rightarrow 0 \leq \varphi \leq \pi; 0 \leq \psi \leq \pi$ and for $\langle 111 \rangle \rightarrow 0 \leq \varphi \leq \pi; -\pi \leq \psi \leq \pi$

$$\lambda_{i_{100}} = h_0 + \frac{1}{3}h_1 + \frac{1}{3}h_4; \quad \lambda_{i_{111}} = h_0 + \frac{1}{3}h_1 + \frac{1}{3}h_3 + \frac{1}{3}h_4$$

Both equations does not assume that domains are distributed equally and therefore must be subtracted from the general solution. To simplify the expression

$$\Delta l / l = \lambda = P + Q \cdot \cos^2(\xi)$$

with

$$Q = (2/5)h_1 + (3/5)h_2 + (12/35)h_4 + (1/35)h_5$$
$$P = -(2/15)h_1 - (1/5)h_2 + (1/5)h_3 - (4/35)h_4 - (1/35)h_5$$
$$P = -(2/15)h_1 - (1/5)h_2 - (2/15)h_3 - (4/35)h_4 - (1/35)h_5$$

is introduced. Limiting only to h_1 and h_2 gives

$$\lambda = -(4/35)h_1 - (6/35)h_2 + ((4/15)h_1 + (6/15)h_2)) \cdot \cos^2(\xi) =$$
$$= \frac{3}{2}((2/5)h_1 + (3/5)h_2)(\cos^2(\xi) - 1/3) =$$
$$= \frac{3}{2}\lambda_s(\cos^2(\xi) - 1/3)$$

where the saturation magnetostriction λ_s is introduced [6, S.22ff].

B Mechanical Deformation

The following picture shows the tensile machine from the group of Professor Zehetbauer.The stripe was attached between the two clams and adjusted to be tension-free. Two white markers were taped in an arbitrary distance on it. When the tensile machine now starts pulling, a camera registers the length change of the two white markers.

Figure B.1: Tensile machine with a M400-50A strip clamped

Also some additional information of the stripes used for the tensile test and the homogeneous stripes are given below.

Strip	Heated [$°C$]	l [mm] x b [mm]	ε [mm]
Tensile 1	450	500×60.1	break
Tensile 2	450	500×60.2	break
Tensile 3	450	500×60.2	break
Tensile 4	450	500×60.1	break
$\varepsilon 0.5\% - H$	460	500×60.2	0.58
$\varepsilon 2\% - H$	460	500×60.1	2.11
$\varepsilon 4\% - H$	460	500×60.2	4.08
$\varphi 4\% - H$	440	500×50.0	4.71
$\varphi 10\% - H$	440	500×50.2	10.85
$\varphi 20\% - H$	440	500×50.2	22.26

Table B.1: Dimensions of the stripes for tensile and rolling deformation

C Samples

This section gives additional information of the samples used in this thesis. The picture below shows the set-up of the two types of samples.

Figure C.1: Standard sample for hysteresis measurement (left) and one with a magnetostriction set-up (right)

In the table below are the dimensions of the ring shaped samples. From this values the magnetic mean path l_m, cross section A_{fe} and the iron fill factor ν_{fe} can be calculated directly.

Sample	d_1 [mm]	d_2 [mm]	h [mm]	m [g]	m_{gl} [g]
Reference					
AsCast	50.093	39.767	1.640	8.12859	0.06006
Reference	50.128	39.732	1.598	8.12966	0.07484
Homogeneous					
$\varepsilon 0.5\% - H$	50.000	39.940	1.620	8.10704	0.07486
$\varepsilon 2\% - H$	50.050	39.830	1.600	8.05457	0.06339
$\varepsilon 4\% - H$	50.080	39.848	1.634	7.96042	0.05442
$\varphi 4\% - H$	46.118	36.704	1.628	6.80584	0.06395
$\varphi 10\% - H$	46.260	36.580	1.454	6.05247	0.04220
$\varphi 20\% - H$	46.136	36.662	1.354	5.67461	0.04759
Inhomogeneous					
P0.05/5-H	50.078	39.852	1.632	8.12844	0.05403
P0.05/15-H	50.138	39.818	1.640	8.12505	0.05822
P0.05/25-H	50.206	39.784	1.622	8.12677	0.06031
P0.035/5-H	50.056	39.882	1.618	8.12601	0.05571
P0.035/15-H	50.146	39.792	1.618	8.12685	0.05725
P0.035/25-H	50.168	39.900	1.618	8.12748	0.05958
P0.01/5-H	50.099	39.957	1.617	8.12744	0.05398
P0.01/15-H	50.102	39.891	1.630	8.12661	0.05421
P0.01/25-H	50.133	39.865	1.621	8.12704	0.05501

Table C.1: Geometry and weight of all samples used for this thesis

D Results

The following table shows the factor Γ in eq. 6.2 for sinusoidal losses. This information is displayed in the appendix, because the whole analysis in this thesis

is based on the results from the triangular H(t)-field. It can be seen, that the calculation of the classical losses is also valid for other signal forms.

Sample	Γ							V_0
	1Hz	2Hz	5Hz	10Hz	20Hz	50Hz	100Hz	
AsCast	0.866	1.082	1.121	1.096	0.960	1.130	0.834	0.2733
Reference	1.164	1.118	0.896	0.933	1.078	0.993	1.018	0.2508
ε0.5%-H	0.836	1.010	0.955	0.843	1.082	1.096	0.991	0.2298
ε2%-H	1.084	0.907	0.974	0.815	1.028	1.030	0.975	0.2211
ε4%-H	0.842	0.815	0.900	0.986	0.876	0.839	0.887	0.1065
φ4%-H	1.081	0.920	1.171	0.881	0.928	0.844	0.923	0.2289
φ10%-H	0.988	1.032	1.077	1.061	0.844	0.901	0.885	0.0688
φ20%-H	1.049	0.832	1.089	0.955	1.061	1.143	0.823	0.0565

Table D.1: Ratio between classical losses from the fitting function and the calculated, as well as the shape factor V_0 from the excess losses under sinusoidal H-field